Igneous processes of the Early Solar System

by
Steven J. Singletary

B.S. Mathematics and Computer Science
University of North Carolina – Pembroke, 1996

M.S. Geology
Texas Christian University, 1999

Submitted to the Department of
Earth, Atmospheric, and Planetary Sciences
in Partial fulfillment of the Requirements for the Degree of

DOCTOR OF PHILOSOPHY
IN
GEOCHEMISTRY
AT THE
MASSACHUSETTS INSTITUTE OF TECHNOLOGY
[February 2004]
DECEMBER, 2003

Signature of Author: _____
Department of Earth, Atmospheric, and Planetary Science
December 5, 2003

Certified By: _____
Timothy L. Grove
Professor of Geology
Thesis Supervisor

Accepted By: _____
Maria Zuber
E. A. Griswold Professor of Geophysics
Head of the Department

Igneous Processes of the Early Solar System

By

Steven J. Singletary

B.S. University of North Carolina – Pembroke, 1996
M.S. Texas Christian University, 1999

Submitted to the Department of Earth, Atmospheric, and Planetary Sciences
On December 5, 2003, in partial fulfillment of the
Requirements for the Degree of
Doctor of Philosophy in Geochemistry

ABSTRACT

Experimental, petrographic and numerical methods are used to explore the igneous evolution of the early solar system. Chapters 1 and 2 detail the results of petrographic and experimental studies of a suite of primitive achondritic meteorites, the ureilites. The first chapter presents data that reveal correlations between mineral modal proportions and mineral chemistry that are used to guide experiments and models of ureilite petrogenesis. Chapter 2 details and applies the experimental results to describe ureilite petrogenesis as the result of progressive heating of a primitive carbon-rich body. The experiments place temperature and depth constraints on ureilite formation of 1100 to 1300°C and 5 to 13 MPa – equivalent to the central pressure of an asteroid with a radius of 130 km. Chapter 3 reports the results of melting experiments of Allende carbonaceous chondrite at temperatures and pressures that would be expected on small bodies in the early solar system (up to 1300°C and 2.5 to 15 MPa) heated by decay of short lived isotopes. The results are then applied to ureilite petrogenesis and assembly of larger planetary bodies. The final chapter is an experimental study to test a hybridized source region for the high titanium lunar ultramafic glasses. Two models are presented that invoke either a heterogeneous source region or sinking and reaction of an ultramafic, titanium rich magma with underlying mantle regions.

Thesis Supervisor: Timothy L. Grove
Title: Professor of Geology

Table of Contents

ABSTRACT..... 3
TABLE OF CONTENTS..... 4
INTRODUCTION..... 6

CHP 1. EARLY PETROLOGIC PROCESSES ON THE UREILITE PARENT BODY..... 9
Abstract..... 9
Introduction..... 9
Techniques..... 12
Elemental Mapping..... 12
Experiments..... 13
Phase Analysis..... 14
Petrography and Mineralogy..... 15
Pyroxenes..... 15
Olivine..... 16
Modal Proportions..... 16
Experimental Results..... 18
Olivine-Pigeonite-Liquid Thermometer..... 19
Discussion..... 20
Smelting..... 20
Evidence for Smelting..... 22
Temperature Variations..... 24
References..... 26
Figure Captions..... 29
Figures..... 31

CHP 2. EXPERIMENTAL CONSTRAINTS ON UREILITE PETROGENESIS..... 48
Abstract..... 48
Introduction..... 48
Ureilite Petrography and Petrology..... 50
Procedures..... 53
Experimental Results..... 55
Approach to Equilibrium..... 55
Pu + Fo_{83}..... 56
Pu + Fo_{75}..... 57
ULM..... 58
ULM + Fo_{75}..... 58
ULM + Fo_{75} + CPX..... 59
Smelting Reaction Calibration..... 60
Petrologic Modeling..... 62
Ca/Al Ratios..... 64
Cr_2O_3..... 65
Discussion..... 65
Conclusions..... 70

References..... 72
Figure Captions..... 75

CHP 3. PARTIAL MELTING EXPERIMENTS OF ALLENDE CV3 MATERIAL..... 107
Abstract..... 107
Introduction..... 107
Previous Experimental Studies..... 108
Experimental Procedure..... 109
Approach to Equilibrium..... 112
Experimental Results..... 112
Discussion..... 114
Application to Ureilite Petrogenesis..... 116
Application to Larger Planetary Bodies..... 118
Conclusions..... 122
References..... 124
Figure Captions..... 127
Figures..... 129

CHP 4. ORIGIN OF LUNAR HIGH TITANIUM ULTRAMAFIC GLASSES: A HYBRIDIZED SOURCE?..... 145
Abstract..... 145
Introduction..... 145
Experimental Procedure..... 148
Experimental Results..... 150
Discussion..... 151
Conclusions..... 155
References..... 157
Figure Captions..... 159
Figures..... 161

Introduction

Since the collapse of the primitive solar nebula, igneous activity has continually modified the material that constitutes our solar system. Driven by heat generated from radioactive decay and kinetic energy released by impacts, this activity has lead to the existence of a wide array of rocks that record the history of our solar system. The stories recorded in the rocks are more often than not incomplete – some pages are missing, others blurred and smeared – such that a simple and straightforward reading of their history is not possible.

In this work, we try to reconstruct several missing portions of our solar system history through the use of detailed petrographic study, petrologic modeling and experiments.

Chapter 1: Early petrologic processes on the ureilite parent body.

Detailed petrographic studies of 21 individual ureilites reveal the existence of previously unrecognized trends that indicate a partial melting, reaction relationship occurring at low pressure and low oxygen fugacity could be responsible for the observed compositional and modal arrays in ureilites. Reconnaissance experiments confirm that a smelting type reaction will generate trends such as those observed in ureilites.

Chapter 2: Experimental constraints on ureilite petrogenesis.

A detailed experimental study was conducted to quantify the smelting process that was proposed in chapter 1. These experiments place constraints on the depths and temperatures at which the ureilites could have been generated. A model of ureilite petrogenesis is developed that invokes heterogeneous accretion of a single ureilite parent

body. Differential heating and diapirism on the parent body lead to the observed ureilite trends in composition, modal proportions and isotopic signatures. The model seeks to reconcile data that suggest very different mechanisms for ureilite petrogenesis.

Chapter 3: Partial melting experiments of Allende CV3 material.

Concrete links between evolved meteorites/planetary material and the most primitive material represented in our collections have proved elusive. Several reconnaissance experiments were conducted to evaluate the melting behavior of primitive material at modest pressures of ~5 to 10 MPa, equivalent to a small body of 50 to 100 km in radius. In addition to supplementing existing data, the results are used to model the compositional behavior of small bodies under going partial melting. The results are applied to ureilite petrogenesis as well as to the effect of partial melting at low pressure on the geochemical characteristic of larger bodies (Earth size) that are assembled from the smaller bodies.

Chapter 4: Origin of high titanium lunar ultramafic glasses: A hybridized source?

Experiments performed for this chapter were designed to investigate igneous activity on a more evolved body, later on in solar system. High-Ti volcanic glasses recovered from the lunar surface by the Apollo astronauts have long been enigmatic in origin. They were produced after crystallization of a lunar magma ocean but exactly how they were generated and even where they originated has remained a mystery. We present data to evaluate a long proposed model of a hybridized source in the lunar mantle. We suggest

generation from a heterogeneous source region or a multi-stage history involving assimilation during sinking of high-Ti bearing melts after generation.

Chp. 1. Early Petrologic Processes on the Ureilite Parent Body

Singletary S.J. and Grove T.L. (2003) Early petrologic processes on the ureilite parent body. *Meteoritics and Planetary Sciences.* **38,** 95-108.

Abstract

We present a petrographic and petrologic analysis of 21 olivine-pigeonite ureilites, along with new experimental results on melt compositions predicted to be in equilibrium with ureilite compositions. We conclude that these ureilites are the residues of a partial melting/smelting event. Textural evidence preserved in olivine and pigeonite record the extent of primary smelting. In pigeonite cores, fine trains of iron metal inclusions are observed that formed by the reduction of olivine to pigeonite and metal during primary smelting. Olivine cores lack metal inclusions but the outer grain boundaries are variably reduced by a late-stage reduction event. The modal proportion of pigeonite and percentage of olivine affected by late stage reduction are inversely related and provide an estimation of the degree of primary smelting during ureilite petrogenesis. In our sample suite this correlation holds for 16 of the 21 samples examined.

Olivine-pigeonite-liquid phase equilibrium constraints are used to obtain temperature estimates for the ureilite samples examined. Inferred smelting temperatures range from ~1150°C to just over 1300°C and span the range of estimates published for ureilites containing two or more pyroxenes. Temperature is also positively correlated with modal percent pigeonite. Smelting temperature is inversely correlated with smelting depth - the hottest olivine-pigeonite ureilites coming from the shallowest depth in the ureilite parent body. The highest temperature samples also have oxygen isotopic signatures that fall toward the refractory inclusion rich end of the carbonaceous chondrite – anhydrous mineral (CCAM) slope 1 mixing line. These temperature-depth variations in the ureilite parent body could have been created by a heterogeneous distribution of heat producing elements indicating that isotopic heterogeneities existed in the material from which the ureilite parent body was assembled.

Introduction

Ureilites are primitive achondrites that are enigmatic in origin. They primarily contain olivine and pyroxene in proportions that vary with mineral composition. Pigeonite occurs as the only pyroxene phase in the majority of ureilites, with augite present in ~10% of the ureilites as small, irregular lamella and blebs in pigeonite and as larger discrete crystals. Orthopyroxene is also present in a number of ureilites giving pyroxene assemblages of pig±aug±opx, pig±opx and aug±opx (Goodrich, 1992; Mittlefehldt *et al*, 1998; Takeda *et al*, 1989). Ureilites contain significant amounts of carbon (~3 wt% on average) typically

found in an intergranular matrix in the form of graphite, lonsdaleite, and diamond (Grady *et al*, 1985). The matrix also contains minor metal (Fe and Ni), sulfides and fine-grained silicates (Mittlefehldt *et al*, 1998). The typical ureilite texture is characterized by ~1 mm, elongate, irregular pigeonite and olivine grains with curved intergranular boundaries that generally meet in triple junctions (Berkley *et al*, 1976; Goodrich, 1992). A few ureilites are texturally heterogeneous and contain regions with the typical mm-sized ureilite texture and regions that contain large pyroxene crystals (up to 15 mm, Mittlefehldt *et al*, 1998).

Several different models have been proposed to explain the processes that generated the ureilites. Goodrich *et al* (1987) developed a multi-stage, igneous cumulate model based on textures in the ureilites and chemical trends in the major mineral phases. They posited that ureilites were precipitated from magmas generated by small degrees of melting (<10%) of a source depleted in plagioclase. Goodrich *et al* (1987) shows the precursor material must have superchondritic Ca/Al ratios. Carbonaceous chondrites, the most plausible precusors, do not have superchondritic Ca/Al ratios and the formation of a ureilite from them would require more than one stage of melt extraction. A problem with this model is that it implies that only a small volume of the original parent material was converted into ureilites. Since the ureilites constitute the second largest group of achondrites, one would expect the complementary material to be represented in our collections. However, no meteorite type complementary to the ureilites has been identified (Rubin, 1988).

Other workers have modeled ureilites as residues of partial melting (Boynton *et al*, 1976; Scott *et al*, 1993; Wasson *et al*, 1976). Previously, the residue models failed to account

for strong mineral alignments observed in the ureilites that suggest they are cumulate in origin (Berkley *et al*, 1980; Rubin, 1988). Walker and Agee (1988) presented experimental evidence that showed the textural alignments could have been formed by thermal compaction, consistent with the residue hypothesis. Early residue models ascribed the high carbon content to impacts of carbon rich bodies into the ureilite parent body. Carbon injection by impacts does not explain the presence of large graphite crystals in low-shock ureilites (Berkley and Jones, 1982). Impact injection also fails to account for carbide-bearing metallic spherules (up to 100 μm) contained within olivine grains that suggest carbon is a primary constituent of the ureilite parent material (Goodrich and Berkley, 1986).

Takeda (1987a) proposed that ureilites represent nebular condensates that underwent high temperature recrystallization during the early stages of planetesimal collision. If this were the case, ureilites should have higher sulfur contents than they do (Rubin, 1988), as sulfide melts do not readily separate from a crystalline silicate melt (Walker and Agee, 1988). Smelting of an olivine-rich source has also been suggested as a petrogenetic process to account for the ureilites (e.g. Warren and Kallemeyn, 1992; Walker and Grove, 1993). The amount of smelting is controlled by C-O-Fe equilibria which is strongly pressure dependent. At low pressures (2.5 MPa) FeO in silicates is unstable and is reduced to Fe metal, producing MgO-rich silicates and a CO gas. Above 10 MPa smelting is suppressed and Fe silicates coexist with graphite (Walker and Grove, 1993). Therefore, the less smelted ureilite samples record greater depths in the parent body, and the more smelted samples record shallow depths. Many authors have argued that if smelting had occurred, there should exist correlations between the modal percentage of

pyroxene, metal content and mg# (defined here as molar MgO/[MgO+FeO]) (e.g. (Goodrich, 1992; Mittlefehldt *et al*, 1998). In previous investigations none of these correlations were found.

This paper presents a study of ureilite petrology coupled with a set of reconnaissance experiments to evaluate smelting as a primary petrogenetic process in the genesis of the ureilites. The smelting process we are hypothesizing is a different and distinct process than that responsible for the reduction rims on ureilite olivine. As many authors have suggested, these reduction rims were formed by a secondary, late-stage reduction process that may have been associated with the disruption of the parent body (e.g. Warren and Kallemeyn, 1992). By studying a large sample suite of ureilites, we hoped to identify the petrologic systematics that have thus far eluded researchers. The experimental results provide an independent check on our results and provide pressure and temperature estimates of ureilite equilibration.

Techniques

Elemental Mapping

For this study we chose 21 thin sections from 19 olivine-pigeonite ureilites representing a range of mineral compositions. The sample suite is listed in Table 1. There are two sets of paired meteorites within the sample set – EET 96293 paired with EET 96314 and QUE 93336 paired with QUE 93341. The MIT JEOL 733 Superprobes were used to obtain high-resolution, back-scattered electron images and elemental x-ray maps of each section. The maps are rectangular in shape and were obtained so as to image the maximum area of the sample with minimal epoxy overlap. The elemental maps were obtained with a stage-

raster technique using an electron beam fixed at x-ray focus, an accelerating potential of 15 kV, a current of 30 nA and diameter of 10 μm. The number of stage steps per traverse (which range from 750 to 1500) and dwell times per stage step (from 5 to 10 msec/step) were varied to obtain a stage speed of 0.1 mm/sec. Step sizes ranged from 10 to 30 μm. Elemental intensities were obtained using wavelength dispersive techniques with Ca, Fe, and Mg measured simultaneously by separate spectrometers.

The pixels of each map were assigned values based on brightness, which is directly proportional to the abundance of the element in the imaged spot. The assigned values were then counted and binned to obtain an approximation of the modal proportions of the phases in the image. Only the Mg map was used to obtain the phase proportions as pigeonite, olivine and the reduced rims were easily differentiated based on Mg content. The phase proportions in each thin section were then taken to represent the modal mineralogy in the entire meteorite. We should note here that we assume the thin sections are representative of the meteorite. For some of the coarser-grained (3mm grain size) ureilites the mapped areas may not provide a representative sample of modal mineralogy and some ureilites may possess textural variability that can not be observed in 10 mm by 5 mm thin sections. The results of the mapping are provided in Table 1.

Experiments

Reconnaissance smelting experiments were carried out using two different starting compositions (Table 2) to explore the temperature-pressure relations of the smelting reaction. The experimental conditions and products are listed in Table 3. The bulk composition of the first mix (PTL) is an approximation of one of three primary trapped liquid compositions from Goodrich *et al* (2001) and was used as a first approximation to

obtaining saturation with the correct phases. The second mix (PU) is an average of melt compositions calculated to be in equilibrium with the ureilite minerals in the 21 samples used in this study. The average PU bulk composition was determined by using the compositions of the major silicate phases in the ureilite samples, temperatures obtained from the olivine-pigeonite thermometer and distribution coefficients calculated from published experiments (see discussion of the olivine-pigeonite thermometer below). The mixes were prepared by combining high purity oxides and Fe sponge (Grove and Bence, 1977). Grinding under ethanol for six hours produced a uniform powder. Ten to 15 mg of the starting material were loaded into a small graphite crucible and then into a Pt tube that was welded on the bottom and loosely crimped and open on the top. The Pt tube and its contents were then run at 1150° to 1220°C for ~19 hrs in a rapid quench, externally heated, 0.25" I.D., ZHM alloy, cold seal pressure vessel pressurized with CO (see Walker and Grove, 1993). Runs were terminated by inverting the ZHM vessel as it was extracted from the furnace, allowing the Pt tube to drop to the cold seal region of the vessel at pressure where the charge quenched. The charges were extracted from their tubes and crucibles, crushed and optically examined by reflected light, mounted in epoxy, then ground and polished to a flat surface for reflected light and electron microprobe examination.

Phase Analysis

The chemical compositions of the major silicate phases in both the ureilite sections and experimental charges were obtained by electron microprobe analysis. The phases were analyzed at an accelerating voltage of 15 kV and a beam current and diameter of 10 nA and ~2 μm. Glasses in the experimental charges were analyzed with a beam diameter of

10 μm. The CITZAF correction package of Armstrong (1995) was used to reduce the data. The atomic number correction of Duncomb and Reed, the Heinrichs tabulation of absorption coefficients, and the fluorescence correction of Armstrong were used to obtain a quantitative analysis (Armstrong, 1995). Compositions of the experimental run products and ureilite samples are presented in Tables 3 and 4, respectively.

Petrography and Mineralogy

Pyroxenes

The majority of the pyroxenes present in ureilites are pigeonites with mg#s from 76 to 93 (Table 4). The pigeonite mg#s correlate with those of coexisting olivine, indicating equilibrium between the two phases, noted by earlier studies (Goodrich, 1992). The pigeonites within each section display grain to grain homogeneity and lack exsolution features, indicating rapid cooling from high temperatures (Goodrich, 1992; Takeda, 1987b).

The pigeonites examined in this study are riddled with trains of fine-grained, metallic inclusions (Fig. 1a) that have been observed previously (Berkley *et al*, 1980; Goodrich, 1992). The percentage of metallic inclusions contained in pigeonite reported in Table 1 is an average of several grains within each thin section as determined by image analysis of high-resolution BSE images. The values range from 0.46 to 2.60 % over all the ureilites examined (Table 1). Individual inclusions display sharp boundaries with the host pigeonite. Most importantly, no reduction haloes are observed around the inclusions, suggesting that they are co-genetic with the pigeonite and were not produced by the late-stage reduction event that modified the olivine rims.

Olivine

Olivine grains are euhedral to anhedral with core compositions ranging from Fo_{76} to Fo_{93} (Table 3), consistent with previous reports for the ureilite compositional range (Berkley *et al*, 1980; Goodrich, 1992; Mittlefehldt *et al*, 1998). The cores of the olivine grains are homogeneous and devoid of the tiny metal inclusions observed in pigeonite (Fig. 1b). Thin reduction rims (~10 to 100 μm) are present on all of the olivine grains where in contact with the carbon-rich matrix. The rims are composed of nearly pure forsterite, enstatite and tiny inclusions of Ni-free Fe metal (Mittlefehldt *et al*, 1998). Metal inclusions in the interior of olivine have been noted rarely (e.g. ALHA77275, Berkley and Jones, 1982). The inclusions in ALHA77275 are on the order of 5-20 μm in size and contain kamacite ± sulfide (troilite) and display eutectoid metal-sulfide intergrowths. In general, a sharp contact is observed between the reduced rim and the homogeneous interior of the olivines. Reduction rims are also found in the other major phases (pigeonite, and some chromite) but are much less pronounced than the ubiquitous olivine rims (Berkley *et al*, 1980). The reduction rims are interpreted to have been formed during a late stage reduction event that affected all ureilites (Berkley *et al*, 1976; Berkley *et al*, 1980; Goodrich, 1992; Warren and Kallemeyn, 1992; Mittlefehldt *et al*, 1998).

Modal proportions

The sample suite displays a range of modal pigeonite proportions. Sample EET 96293 defines the upper limit of the range at ~56% pigeonite, with the lower end bounded by GRA 95205 at ~5% pigeonite. A range in the amount of reduction of olivine (measured as the percent olivine contained in reduction rims) is also observed - from 0 to 60%. Figure 2 shows the modal proportions of pigeonite plotted against the amount of

reduction in the rims of the olivine grains for each sample. Examination of Mg elemental maps of samples from the extremes of the trend reveals that those sections with higher proportions of pigeonite have sharper, more distinct grain boundaries. Conversely, sections with a low pigeonite component have large amounts of secondary olivine reduction and more diffuse, less well defined grain boundaries (Fig. 3).

The data plotted in Figure 2 suggest there is a trend of increasing olivine reduction with decreasing pigeonite content although there are several distinct outliers. Of the 21 samples examined, 16 define a trend from low modal pigeonite (10 to 25 %) and high percentages of reduced olivine (50 %) toward high modal pigeonite (40 to 55 %) and no reduced olivine. Five samples do not follow this trend. There are 3 outlier ureilites at 5 to 20 % modal pigeonite and 0 % reduced olivine and 2 outliers at 50 % pigeonite and 50 % reduced olivine. The two samples that plot above the trend are texturally distinctive. Dingo Pup Donga exhibits a brecciated nature and thus may not be representative of the equilibrated olivine-pigeonite ureilites. The second, QUE 93341, displays wide olivine reduction rims but still has sharp, well-defined grain boundaries. QUE 93341 is paired with QUE 93336, which lies on the trend between modal percent pigeonite and olivine reduction we suggest. Due to the coarse-grained nature of ureilites and their inferred origin as residues, we suspect that significant textural heterogeneity exists and could be responsible for the outliers we observe in Fig. 2.

The 3 samples with variable modal pigeonite and no reduction of their coexisting olivine rims may be explained if C is heterogeneously distributed in the ureilite samples. Carbon contents in ureilites range from 2 to 6 wt. % with a few samples containing as little as 0.2 wt. % C (Grady *et al*, 1985). Measurements of carbon for individual ureilites are variable

and this variability is assumed to result from the heterogeneous distribution of the C-rich matrix in the sample (Mittlefehldt *et al*, 1998). This would also explain the absence of a correlation between mineralogy and C content (Grady *et al*, 1985). Nevertheless, of the 21 ureilites examined in this study, 16 fall on the trend we would expect if primary smelting of the ureilites occurred. In order to resolve the discrepancies in Fig. 2, more thin sections of ureilite samples must be quantitatively mapped using techniques like those outlined in this paper.

Experimental Results

The PTL experiments (composition of Goodrich *et al*, 2001) are all saturated with olivine, small amounts of iron metal, and melt. The highest temperature and pressure experiment (1200°C, 7.5 MPa) contains only those three phases. Three intermediate runs, from 1200 to 1170°C and 7.5 to 1.3 MPa, have augite as an additional phase. The lowest temperature run (1150°C at 7.5 MPa) also contains plagioclase. The results of the experiments are given in Table 3 and represented graphically in Figure 4.

The second set of experiments was performed using a mix of 80% PU and 20% $Fo_{83.8}$ olivine. The runs were isothermal (1220 °C) and pressure ranged from 7.5 to 1.5 MPa. The runs are all saturated with augite, pigeonite, and iron metal. Figure 5 plots the mg# of the augite for both the PTL and PU series against the pressure of each experiment. The mg# of Hughes009 is shown for reference. As pressure decreases, the mg# of the augite increases. The same relation also holds for the forsterite content of the coexisting olivine in the PTL experiments. At constant pressure, the mg# of the augite also varies with increasing temperature, as shown by the three experiments at 7.5 MPa.

Olivine-Pigeonite-Liquid Thermometer

Temperature estimates currently exist for only a few ureilite samples (e.g. (Chikami *et al*, 1997; Takeda, 1987a, b; Takeda *et al*, 1989). The available temperature estimates were made using a two-pyroxene thermometer, which requires the coexistence of pigeonite and augite or orthopyroxene and augite (Goodrich *et al*, 2001). Ureilites are acknowledged to be igneous rocks quenched rapidly from high (~1200 °C) super-solidus temperatures. Therefore, it is reasonable to see if the assumption of coexisting olivine – pigeonite – liquid can be used to further understand the conditions of ureilite formation. Because our samples only contain one pyroxene (pigeonite) coexisting with olivine, we have developed an olivine-pigeonite-liquid thermometer to obtain temperature estimates. Compositional data sets for published experiments that contain the phase assemblage olivine, pigeonite, and liquid (Bartels and Grove, 1991; Nielsen *et al*, 1988) were used to calibrate the thermometer. Distribution coefficients were calculated for SiO_2, Al_2O_3, TiO_2, FeO, MgO, MnO, CaO and Cr_2O_3 between both olivine/liquid and pigeonite/liquid for each published experiment. The distribution coefficients were then used to calculate an equilibrium liquid for each ureilite in this study.

Both CaO and MgO in pigeonite from all the experimental data display linear trends in ln $D^{pig/liq}_{(CaO,MgO)}$ vs 10000/T space (R^2 of 0.35 and 0.98 respectively; Fig. 6). The CaO and MgO compositions of pigeonite coexisting with olivine and liquid show systematic variations with temperature (Fig. 7).

The compositions of the pigeonites were treated as temperature dependent variables from which we developed an expression for temperature. Through multiple least squares regression analysis of the data set, we obtain the temperature expression (in °C):

$$T = 812.6(\pm 21.8) + 11.1\ (\pm 0.6)\ MgO\ (mol\%) + 4.0\ (\pm 1.6)\ CaO\ (mol\%) \quad (1).$$

The errors on the coefficients are one sigma with the largest error on the constant term and $R^2 = 0.97$ for fitting the entire published data set. Figure 8 is a plot of the experimental temperature vs. estimated temperature and shows that our derived expression is able to recover temperatures to within ~ ± 20°C. Armed with the modal mineralogy, compositional data, and temperature estimates, we now investigate smelting as a process for generating the olivine-pigeonite ureilite assemblage.

Discussion

Smelting

Smelting is generally thought of as reduction of a solid Fe-bearing oxide or silicate to produce a pure Fe metal and gas phase. This process is commonly used in the iron industry with solid iron oxide ore and carbon to produce a pure iron melt. For the purposes of this study, we define smelting as:

olivine + silicate liquid + carbon → pigeonite + Fe metal + carbon monoxide. (2)

All discussions of smelting in this paper will refer to this reaction proceeding as written. For the purposes of discussion, we assume the silicate melt involved in the reaction is a partial melt derived from the ureilite parent body. At present we have little control on the melt composition but experiments are in progress to help constrain this important variable. We are also assuming CO is confined by lithostatic pressure and our discussion is based on CO being in equilibrium at each pressure.

We have calibrated the smelting reaction coefficients using the decompression-smelting experiments on lunar sample 12002 of Walker and Grove (1993). The reaction is

$$1\ liq + 0.72\ Ol + 0.43\ C = 1.29\ Pig + 0.43\ Fe + 0.43\ CO \quad (3)$$

with the stoichiometric coefficients reported as wt%. As the degree of smelting increases, the amount of free iron and pigeonite will increase and the amount of carbon decreases. Therefore, ureilites with a higher modal percent pigeonite have been smelted to a higher degree.

The effects of smelting should also be observed as systematic variations in mineral composition. As smelting proceeds, carbon is reacted and converted into CO gas and metallic Fe is produced. The mg#s of the major phases should then rise in response to this reaction. Since pressure and smelting extent are inversely correlated, shallower ureilite residues will be more smelted and have a higher mg#, while deeper residues will have a lower mg# and have experienced less smelting. We also predict that ureilites containing olivine and pyroxene with higher mg#s represent portions of the ureilite parent body that are smelted to a higher degree and resided at shallow depths (Walker and Grove, 1993). The variation in modal pigeonite and olivine Fo content in the 21 ureilites from our sample suite are plotted in Fig. 9. The trend of increasing Fo content with increasing modal pigeonite is followed for most samples. The exception is QUE 93341with high modal pigeonite at low Fo. However, QUE 93336 which is paired with QUE 93341 does fall on the trend. QUE 93341 also contains a large percentage of late stage olivine reduction rims (Fig. 2). Also shown in Fig. 9 is a calculated change in Fo content and modal pigeonite using the stoichiometric coefficients from the Walker and Grove (1993) smelting reaction [3]. The variations in the ureilite sample suite and the modeled smelting trend are broadly parallel for the more iron-rich samples, but there is more scatter in the high modal pigeonite – high Fo end of the suite.

Evidence for Smelting

Two key observations are the presence of metal inclusions in pigeonite and the absence of the metal inclusions in coexisting olivine. Both observations are consistent with smelting of olivine to produce metal + pigeonite. The metal inclusions present in pigeonite represent the co-formation of these phases by the smelting reaction. The absence of reduction halos around the metal inclusions, and their uniform dispersion throughout the pigeonite grains (see Fig. 1a) indicates that the metal was not derived by late stage reduction of the pigeonite. The lack of such metal grains in cores of olivine grains indicates that they were not present when this silicate phase formed.

We also observe that ureilites with high modal proportions of pigeonite have sharp olivine and pigeonite grain boundaries and lower total amounts of late-stage reduction of olivine rims (see Fig. 3). This can be explained by our conclusion that ureilites with higher modal percent pigeonite have been smelted to a higher degree. One manifestation of this is seen by the increased degree of late stage reduction of olivine in samples that have a low pigeonite component (Fig. 2). Ureilites that have undergone little to no smelting would be expected to retain much of their primary carbon, which is utilized in the reduction of olivine during the secondary reduction event (assuming they all originally had similar C contents). The exceptions are QUE 93341 and Dingo Pup Donga, which contain significant secondary olivine reduction and 50% modal pigeonite and the 3 samples (ALHA78262, A 881931 and GRA 95205) that do not contain reduced olivine rims. As discussed earlier, we suggest that these exceptions to the trend may be explained by compositional and textural heterogeneities in the ureilite meteorites. Our textural studies rely on very small sample areas, and heterogeneities in the distribution of

C and in the proportions of olivine and pigeonite are known to exist (Mittlefehldt *et al*, 1998).

At this point we feel that the presence of trends between modal percent pigeonite, percentage of olivine reduction (Fig. 2) and mineral compositions (Fig. 9) warrants serious consideration of smelting as an important petrologic process involved in the primary petrogenesis of the ureilites. The relation of these petrologic and mineralogical parameters to carbon content is less secure. Many authors have sought a relation between carbon content and geochemical parameters and have found no correlation (Mittlefehldt *et al*, 1998). There is little overlap between our sample suite and the sample suite that has been analyzed for carbon content (only 4 samples analyzed by Grady *et al* (1985) are also among our 21 samples and these 4 all contain ~ 2 wt. % carbon). Therefore, we can not establish any relation between our textural criteria for smelting and carbon content. The results of our temperature estimations are presented in Table 4. Calculated temperatures range from ~1150°C to just over 1300°C and are in general agreement with those previously published (1180°C to 1300°C; Takeda, 1987b). Calculated temperatures using our estimation technique are also similar to those inferred by Sinha *et al* (1997) for their Group II and III ureilites. However, the temperature estimates of Sinha *et al* (1997) for their Group I ureilites are systematically lower by 100 °C when compared to our olivine - pigeonite and the Takeda *et al* (1987) two-pyroxene thermometry estimates. Because our estimates conform to those of Takeda *et al* (1987) and because we are able to recover experimental temperatures using our method (see Fig. 8), we feel the temperatures we report best estimate the igneous conditions experienced by ureilite residues.

There is a positive correlation of olivine forsterite content with temperature (Figure 10). This relation holds true for all samples examined in this study, as well as for data from the literature (Berkley *et al*, 1980; Chikami *et al*, 1997; Goodrich, 1992). The correlation of high temperatures with high modal percent pigeonite and olivine forsterite contents indicates that the more smelted (lower pressure and therefore assumed to be shallower) samples have experienced the highest temperatures. The higher temperatures may have driven smelting reactions further. But what was the reason for higher temperatures in some ureilites and not others?

Temperature Variations

The temperature gradient present during the early stages of ureilite planetesimal formation is unknown, but a good starting assumption would be that depth and temperature are positively correlated. Therefore, ureilite samples that yield higher temperatures should represent a deeper sampling of the parent body. However, the higher temperature ureilites are also more mg-rich (Fig. 10), and therefore require shallower smelting depths. Walker and Grove (1993) proposed that the suppression of the smelting reaction should provide a minimum estimate of parent body size (~100 km) and a stratigraphy within the ureilite parent body defined by mg# (deeper samples having low mg#s and shallower samples having high mg#s). The results of our experiments are also consistent with deeper samples having low mg#s and a shallow depth of origin for the high mg# augite-bearing ureilites (Fig. 5). Furthermore, our results suggest that temperature and smelting depth are inversely related in the ureilite parent body. In other words, the shallower ureilite residues are more smelted and formed at higher temperatures, while the less smelted ureilite residues formed at greater depths and lower

temperature. An explanation for this inverse correlation could be that the upper regions of the ureilite parent body were hotter due to heat addition from impacts. Another possible explanation of the temperature inversion may be that the ureilite parent body was compositionally heterogeneous.

Oxygen isotopic studies of the ureilites show significant variation that could indicate the parent body may have been isotopically heterogeneous (Clayton and Mayeda, 1988, 1996). The isotopic data scatter along a line with slope ~1 on the oxygen three isotope plot. Refractory inclusions from the Allende carbonaceous chondrite also plot along the same line (Fig. 11). The Allende refractory inclusions are rich in Al-bearing minerals (spinel, corundum, perovskite, etc.; Brearley and Jones, 1998). The heterogeneous incorporation of inclusions into the ureilite parent body would lead to an inhomogeneous distribution of short-lived radionuclides (i.e. ^{26}Al) and differential heating of the parent body. The correlation of high temperature, high mg# samples with the Allende CAI oxygen isotopic signature (Fig. 12) is consistent with this idea. The correlation of high temperature, shallow smelting and oxygen isotopes could be caused by an accretion-inherited radial heterogeneity in the small (~100 km) planetesimal. It could also be a consequence of other heterogeneities that might lead to thermal buoyancy, diapirism and subsequent smelting that proceeds to higher degrees and ends at shallower depths.

References

ARMSTRONG J. T. (1995) Citzaf - a package of correction programs for the quantitative electron microbeam x-ray-analysis of thick polished materials, thin-films, and particles. *Microbeam Analysis* **4**, 177-200.

BARTELS K. S. AND GROVE T. L. (1991) High-pressure experiments on magnesian eucrite compositions: constraints on magmatic process in the eucrite parent body. *Proc. Lunar Planet. Sci Conf.* **21st**, 351-365.

BERKLEY J. L., BROWN H., KEIL K., CARTER N. L., MERCIER J. C. C. AND HUSS G. (1976) The Kenna ureilite – An ultramafic rock with evidence for igneous, metamorphic, and shock origin. *Geochim. Cosmochim. Acta* **40**, 1429-1437.

BERKLEY J. L. AND JONES J. H. (1982) Primary igneous carbon in ureilites: Petrological implications. *Proc. Lunar Planet. Sci. Conf.* **13th**, *J. Geophys. Res.* **87**, A353-A364.

BERKLEY J. L., TAYLOR G. J., KEIL K., HARLOW G. E. AND PRINZ M. (1980) The nature and origin of ureilites. *Geochim. Cosmochim. Acta* **44**, 1579-1597.

BOYNTON W. V., STARZYK P. M. AND SCHMITT R. A. (1976) Chemical evidence for genesis of ureilites, achondrite chassigny and nakhlites. *Geochim. Cosmochim. Acta* **40**, 1439-1447.

BREARLY A. J. AND JONES R. H. (1998) Chondritic Meteorites. In *Planetary Materials* (ed. J. Papike), **36**.

CHIKAMI J., MIKOUCHI T., TAKEDA H. AND MIYAMOTO M. (1997) Mineralogy and cooling history of the calcium-aluminum-chromium enriched ureilite, Lewis Cliff 88774. *Meteorit. Planet. Sci.* **32**, 343-348.

CLAYTON R. N. AND MAYEDA T. K. (1988) Formation of ureilites by nebular processes. *Geochim. Cosmochim. Acta* **52**, 1313-1318.

CLAYTON R. N. AND MAYEDA T. K. (1996) Oxygen isotope studies of achondrites. *Geochim. Cosmochim. Acta* **60**(11), 1999-2017.

GOODRICH C. A. (1992) Ureilites: A critical-review. *Meteoritics* **27**(4), 327-352.

GOODRICH C. A. AND BERKLEY J. L. (1986) Primary magmatic carbon in ureilites: Evidence from cohenite-bearing metallic spherules. *Geochim. Cosmochim. Acta* **50**, 681-691.

GOODRICH, C. A., JONES, J. H. AND BERKLEY, J. L. (1987) Origin and evolution of the ureilite parent magma: Multi-stage igneous activity on a large parent body. *Geochim. Cosmochim. Acta* **51**, 2255-2273.

GOODRICH C. A., FIORETTI A. M., TRIBAUDINO M. AND MOLIN G. (2001) Primary trapped melt inclusions in olivine in the olivine- augite-orthopyroxene ureilite Hughes 009. *Geochim. Cosmochim. Acta* **65**, 621-652.

GRADY M. M., WRIGHT I. P., SWART P. K. AND PILLINGER C. T. (1985) The carbon and nitrogen isotopic compositions of ureilites: implications for their genesis. *Geochim. Cosmochim. Acta* **49**, 903-915.

GROVE T. L. AND BENCE A. E. (1977) Experimental study of pyroxene-liquid interaction in quartz-normative basalt 15597. *Proc. Lunar Sci. Conf.* **8th**, 1549-1579.

MITTLEFEHLDT D. W., McCOY T. J., GOODRICH C. A. AND KRACHER A. (1998) Non-chondritic meteorites from asteroidal bodies. In *Planetary Materials* (ed. J. Papike), **36**.

NIELSEN R. L., DAVIDSON P. M. AND GROVE T. L. (1988) Pyroxene-melt equilibria - an updated model. *Contrib. Mineral. Petrol.* **100**, 361-373.

RUBIN A. E. (1988) Formation of ureilites by impact-melting of carbonaceous chondritic material. *Meteoritics* **23**, 333-337.

SCOTT E. R. D., TAYLOR G. J. AND KEIL K. (1993) Origin of ureilite meteorites and implications for planetary accretion. *Geophys. Res. Lett.* **20**, 415-418.

SINHA S. K., SACK R. O AND LIPSCHUTZ M. E. (1997) Ureilite meteorites: Equilibration temperatures and smelting reactions. *Geochim. Cosmochim. Acta* **61**, 4235-4242.

TAKEDA H. (1987a) A coexisting orthopyroxene-pigeonite pair in yamato-791538 and formation condition of ureilites. *Meteoritics* **22**, 511-512.

TAKEDA H (1987b) Mineralogy of Antarctic ureilites and a working hypothesis for their origin and evolution. *Earth Planet. Sci. Lett.* **81**, 358-370.

TAKEDA H., MORI H. AND OGATA H. (1989) Mineralogy of augite-bearing ureilites and the origin of their chemical trends. *Meteoritics* **24**, 73-81.

WALKER D. AND AGEE C. B. (1988) Ureilite compaction. *Meteoritics* **23**, 81-91.

WALKER D. AND GROVE T. (1993) Ureilite smelting. *Meteoritics* **28**, 629-636.

WARREN P. H. AND KALLEMEYN G. W. (1992) Explosive volcanism and the graphite oxygen fugacity buffer on the parent asteroid(s) of the ureilite meteorites. *Icarus* **100**, 110-126.

WASSON J. T., CHOU C. L., BILD R. W. AND BAEDECKER P. A. (1976) Classification of and elemental fractionation among Ureilites. *Geochim. Cosmochim. Acta* **40**, 1449-1458.

Figure Captions

Figure 1. a) Pigeonite from the El Gouanem ureilite displaying trains of tiny metallic inclusions that are representative of the ureilites examined in this study. The dark areas are pits in the grain. b) Olivine from the same thin section. Notice the absence of inclusions in the interior of the grain. The only iron present is found in conjunction with the secondary reduction rims that have prominent reduction haloes (seen around the Fe metal on the left side of the image).

Figure 2. Modal percent pigeonite plotted against the amount of reduction in olivine as determined by image analysis. Dotted lines connect paired meteorites.

Figure 3. Mg maps of ureilites with different modal percents of pigeonite. In both images, the lighter grey phase is olivine, the darker phase is pigeonite. a) GRA 95205 with ~5% pigeonite. The grain boundaries are diffuse and not well defined. b) With over 50% pigeonite, EET 96293 displays sharper grain boundaries.

Figure 4. Mineral assemblages of experiments using the PTL and PU bulk compositions (see text).

Figure 5. Mg# of augite from both PTL and PU experiments plotted against the pressure of each experiment (10 bars = 1 MPa). A general trend exists within each experimental set of increasing mg# with decreasing pressure. Mg# of Hughes 009 is shown for reference.

Figure 6. Ln $D^{pig/liq}$ vs 10000/T plots of CaO and MgO data from published experiments used to obtain the expression for the Olivine-Pigeonite thermometer (see text).

Figure 7. Plot of molar percent CaO vs MgO in pigeonite from published experiments (see text) and ureilite samples from this study. Isotherms calculated using eqn. (1). Numbers in italics by experimental points are the reported experimental temperatures.

Figure 8. Experimental temperature vs. estimated temperature using eqn. [1] for published experiments (see text) and experiments in this study. Even though the 2σ error is ±40°C, eqn [1] recovers temperature to within ±20°C.

Figure 9. Modal percent pigeonite plotted against the olivine Fo content. There is an overall positive correlation, consistent with a smelting process. Arrow indicates the expected changes in olivine Fo and modal percent pigeonite with 12% smelting (calculated using eqn. (3)).

Figure 10. Ureilite olivine Fo content vs. estimated temperature using the olivine-pigeonite thermometer. Published olivine Fo values taken from Chikami et al. (1997), Berkley *et al* (1980) and Goodrich *et al* (1987).

Figure 11. Oxygen isotopic compositions of dark inclusions from CV3 chondrites and ureilites. The ureilites scatter about a line extrapolated from the inclusions. The more smelted ureilites (higher mg#), as determined in this study, fall towards the CAIs (see Fig. 12). The italicized numbers are the mg# of the plotted ureilite. Adapted from Figure 1 in Clayton and Mayeda (1988).

Figure 12. Olivine Fo content vs. $\Delta^{17}O$. $\Delta^{17}O$ data taken from Clayton and Mayeda (1988, 1996). Ureilites with lower $\Delta^{17}O$ values have higher olivine Fo contents, indicating an advanced degree of smelting.

Figure 1.

a)

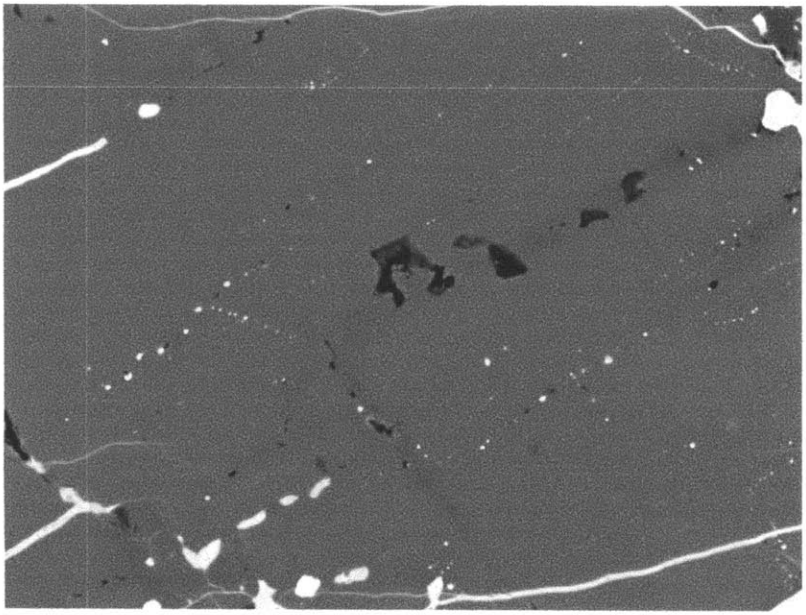

100 μm

b)

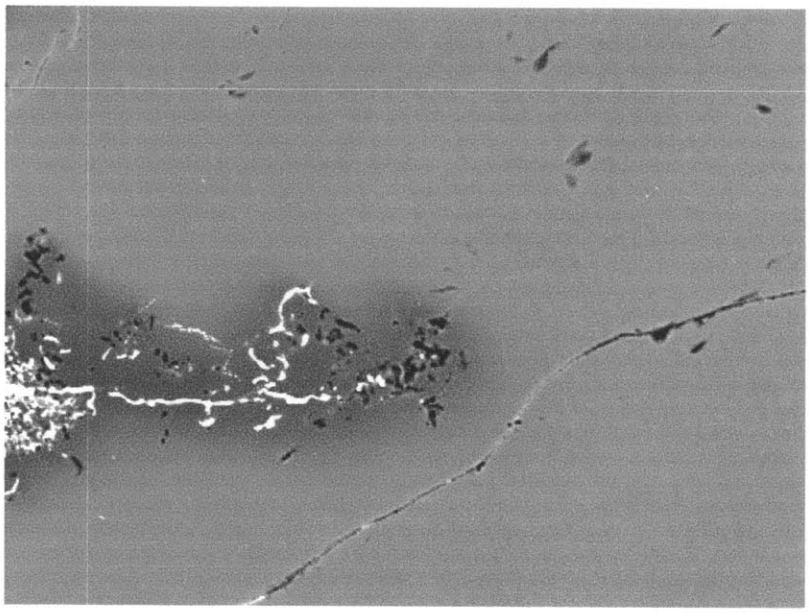

100 μm

Figure 2.

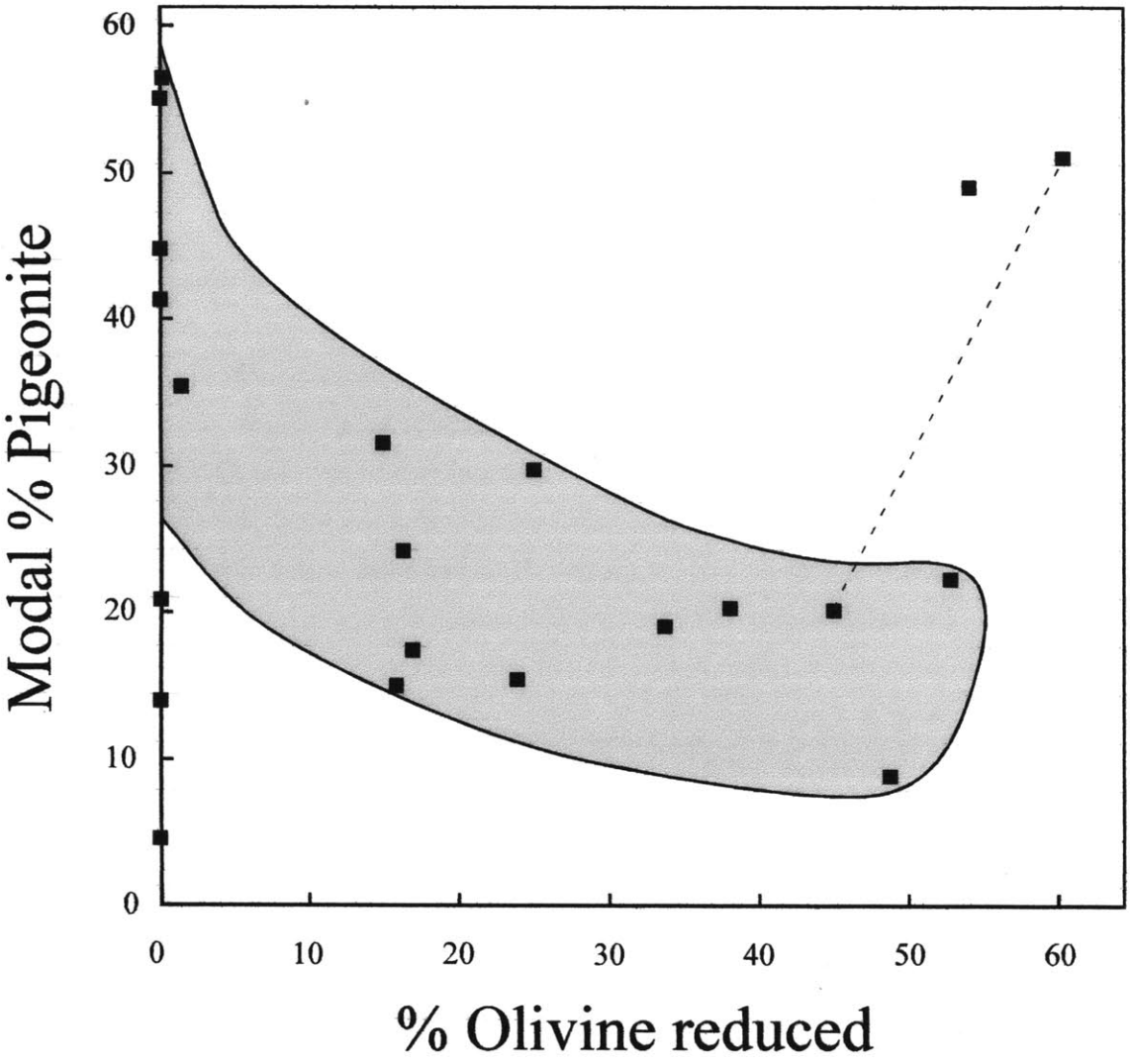

Figure 3.

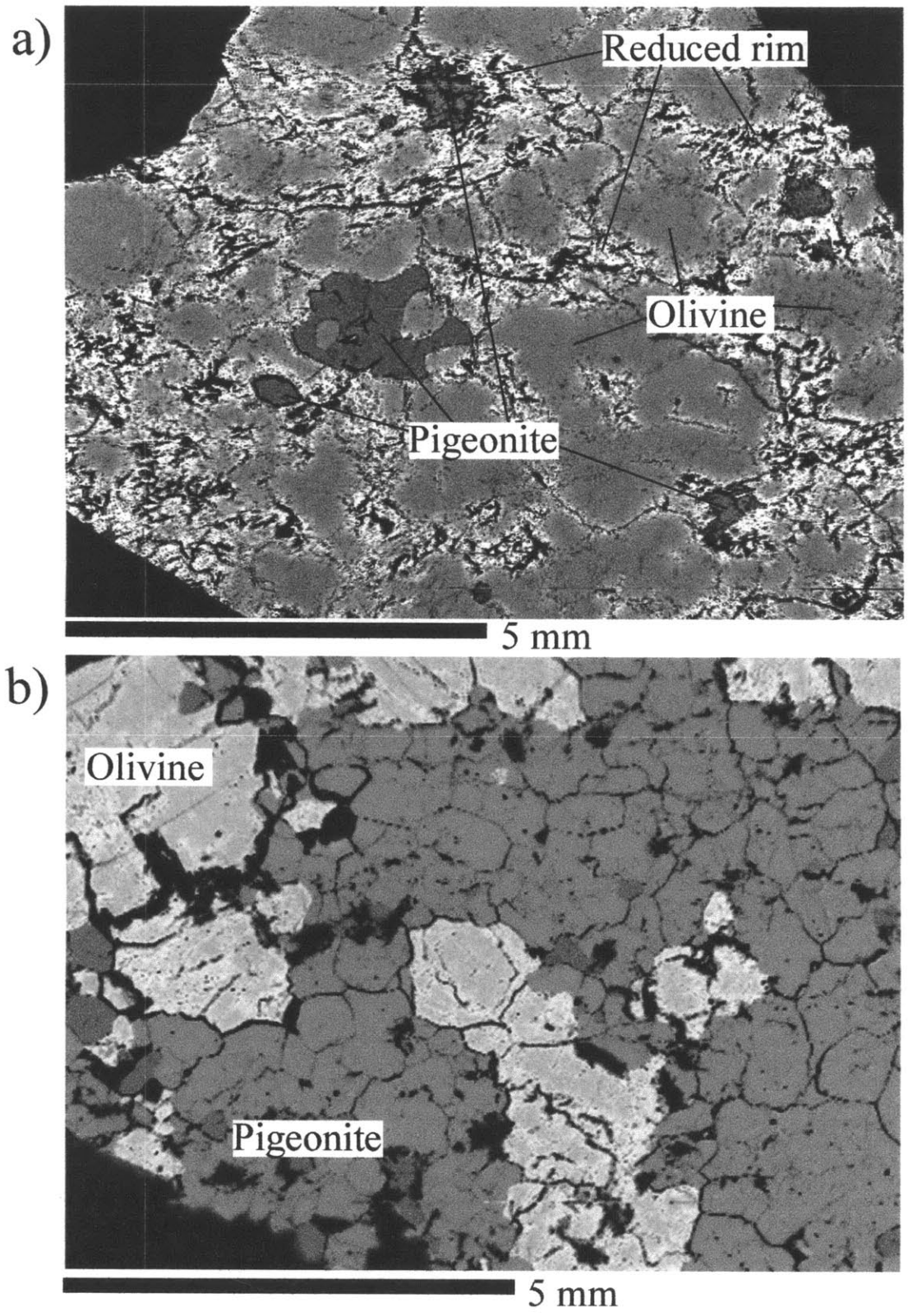
a)
Reduced rim
Olivine
Pigeonite
5 mm
b)
Olivine
Pigeonite
5 mm

Figure 4.

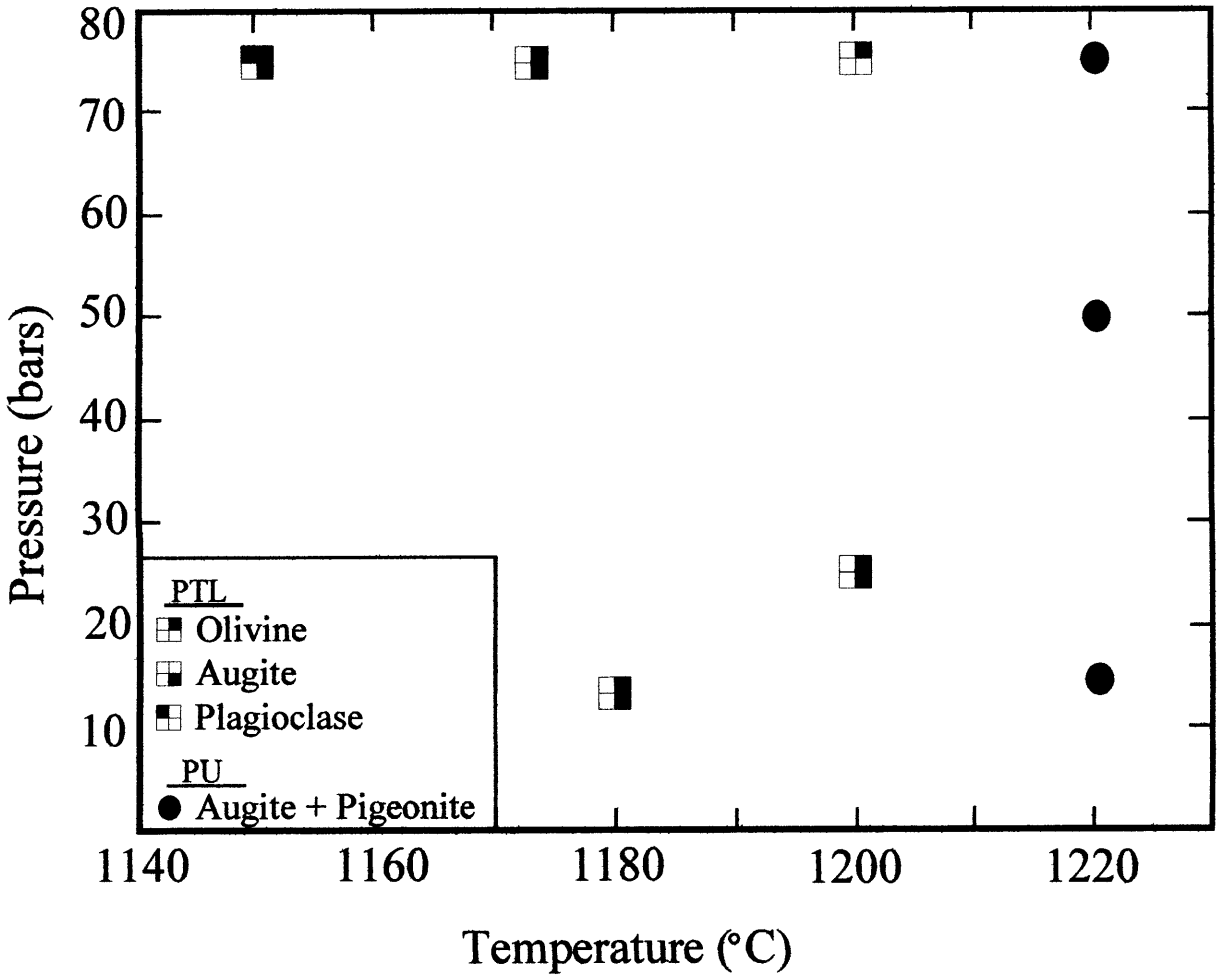
80
70
60
50
40
30
20
10
Pressure (bars)
PTL
Olivine
Augite
Plagioclase
PU
Augite + Pigeonite
1140
1160
1180
1200
1220
Temperature (°C)

Figure 5.

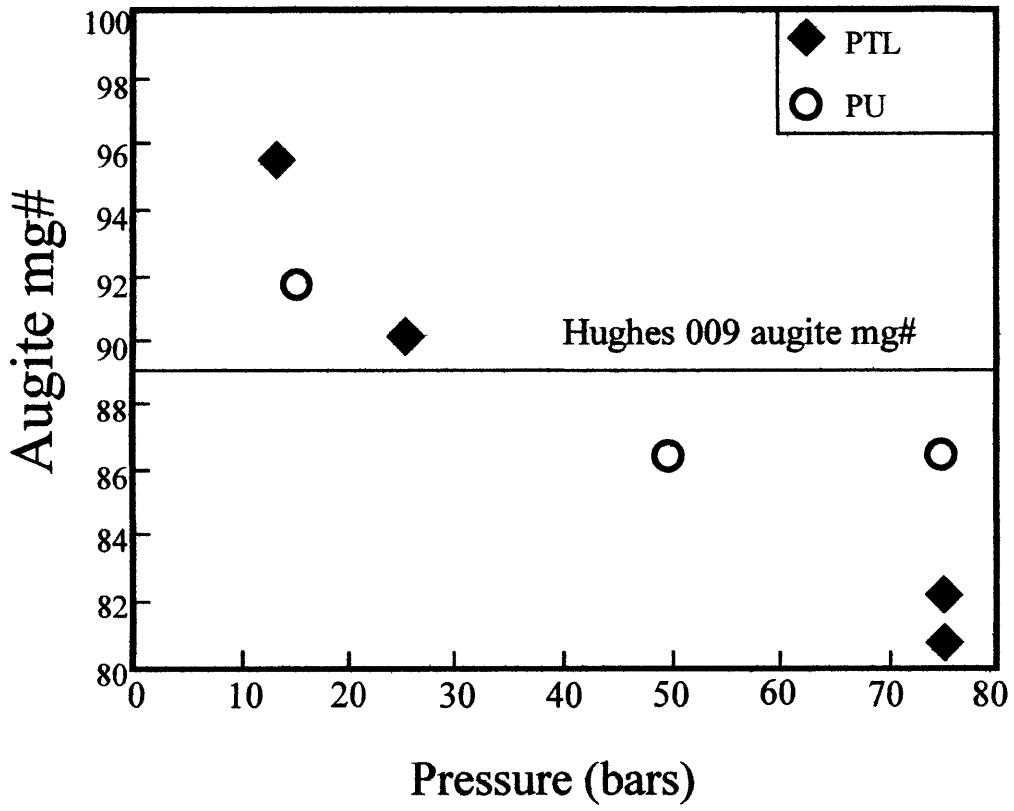
PTL
PU
Hughes 009 augite mg#
Augite mg#
Pressure (bars)
100
98
96
94
92
90
88
86
84
82
80
0
10
20
30
40
50
60
70
80

Figure 6.

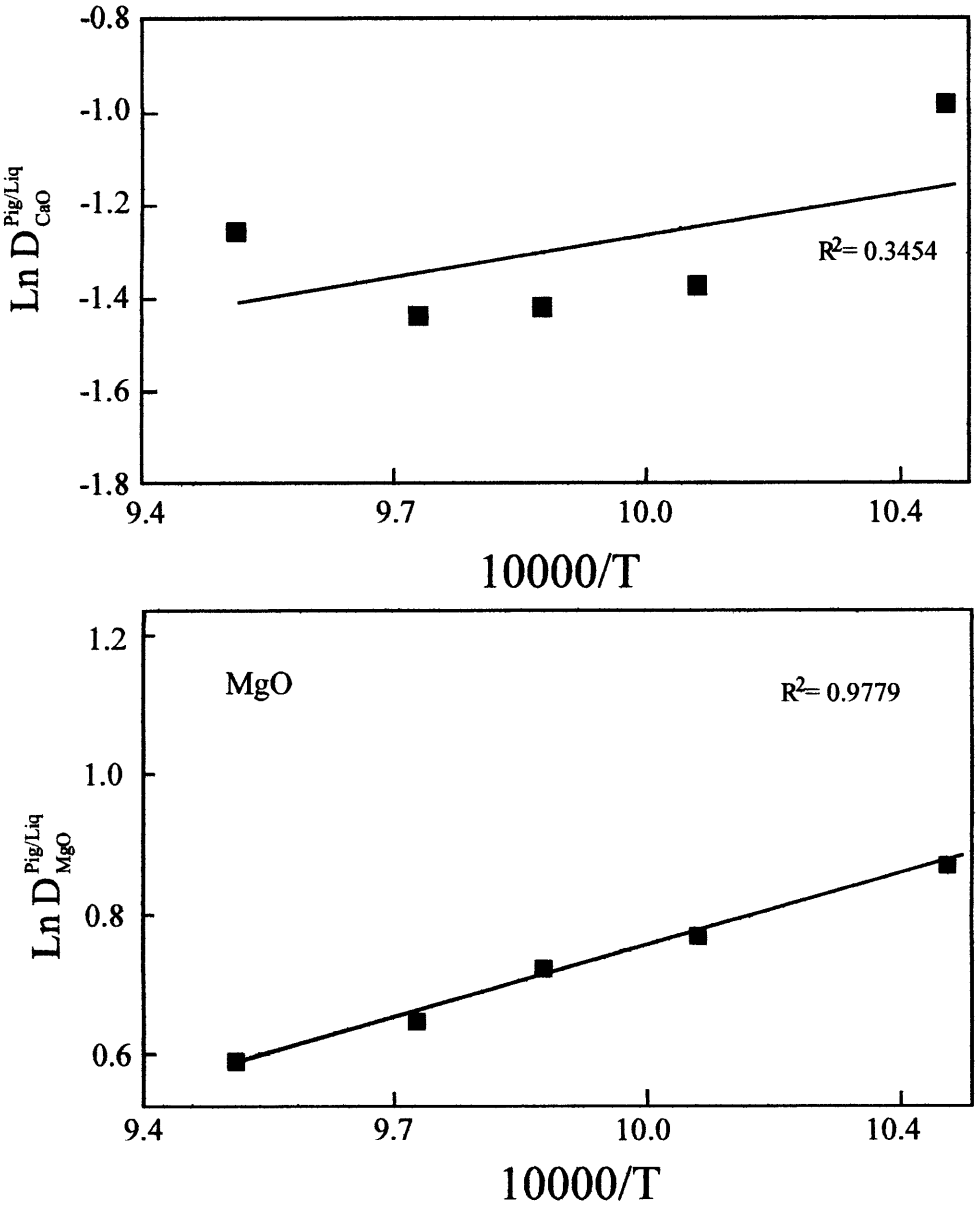
-0.8
-1.0
-1.2
-1.4
-1.6
-1.8
Ln D Pig/Liq CaO
R2= 0.3454
9.4
9.7
10.0
10.4
10000/T
1.2
1.0
0.8
0.6
MgO
R2= 0.9779
Ln D Pig/Liq MgO
9.4
9.7
10.0
10.4
10000/T

Figure 7.

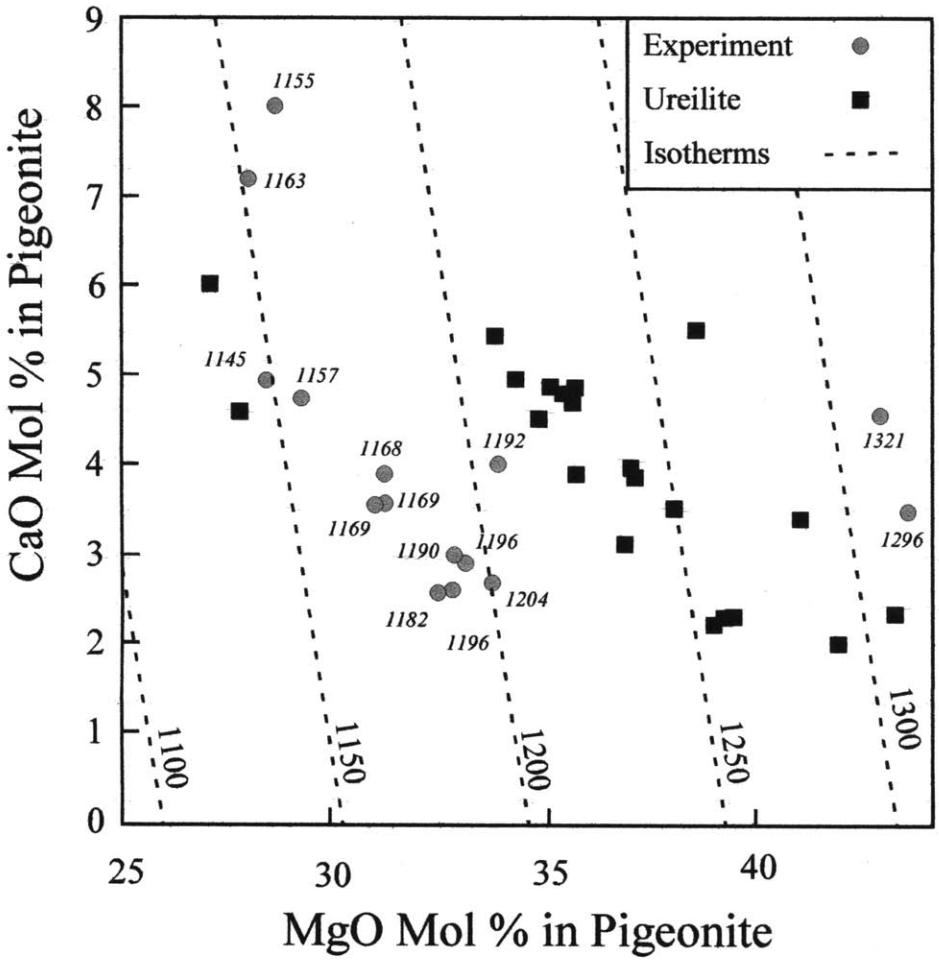
Experiment
Ureilite
Isotherms
CaO Mol % in Pigeonite
MgO Mol % in Pigeonite
0
1
2
3
4
5
6
7
8
9
25
30
35
40
1155
1163
1145
1157
1168
1169
1169
1190
1196
1182
1196
1192
1204
1321
1296
1100
1150
1200
1250
1300

Figure 8.

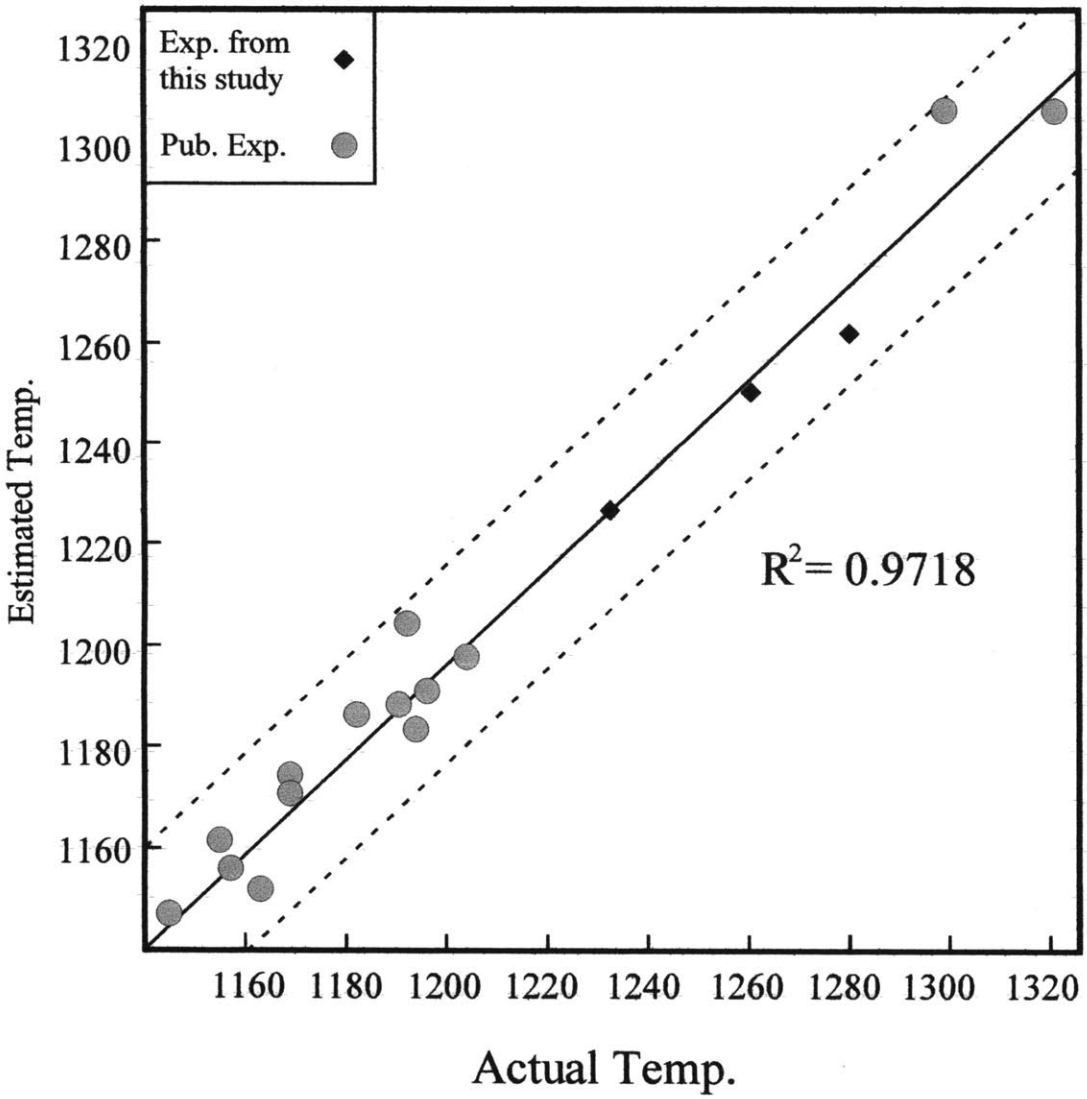
Exp. from this study
Pub. Exp.
R^2= 0.9718
Estimated Temp.
Actual Temp.
1160
1180
1200
1220
1240
1260
1280
1300
1320

Figure 9.

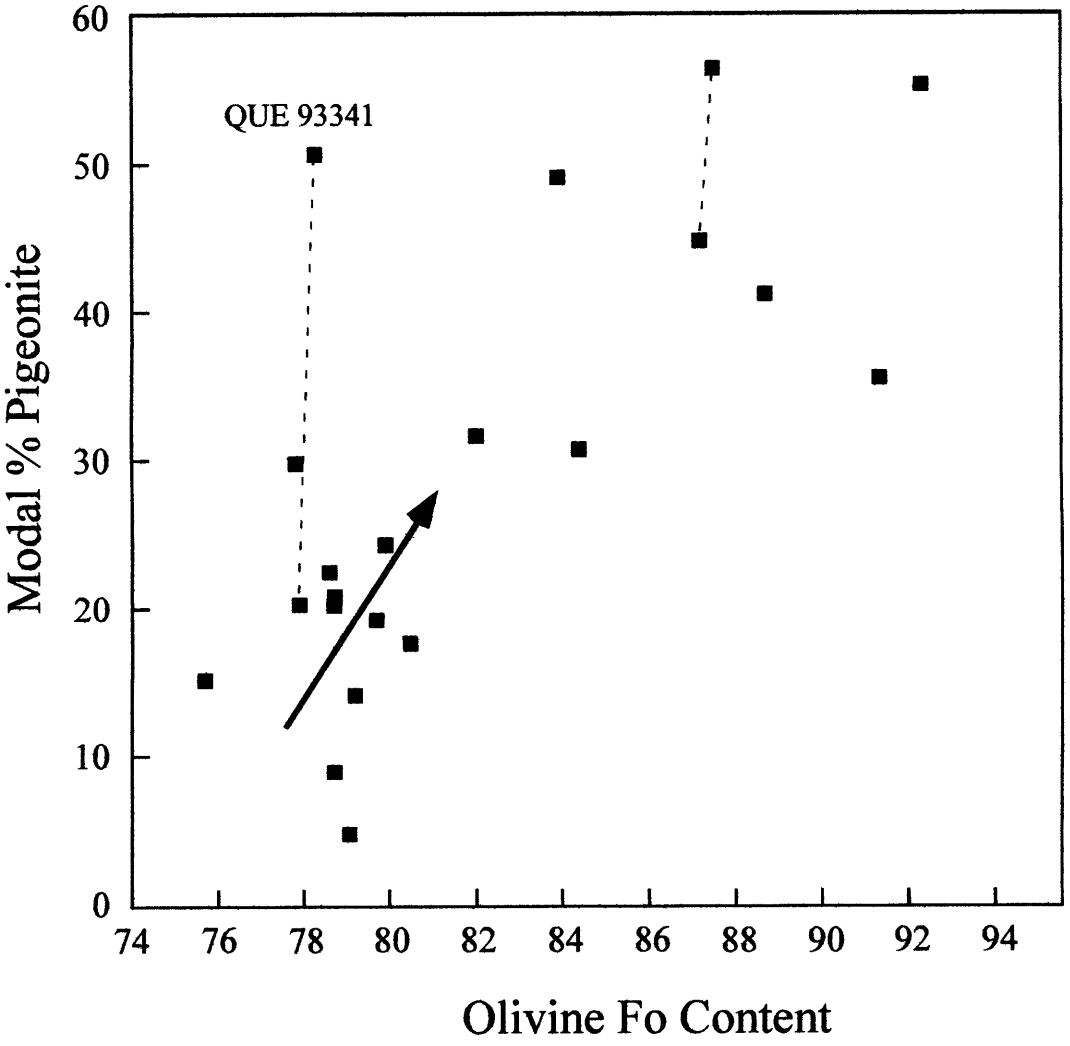
QUE 93341
Modal % Pigeonite
Olivine Fo Content
60
50
40
30
20
10
0
74
76
78
80
82
84
86
88
90
92
94

Figure 10.

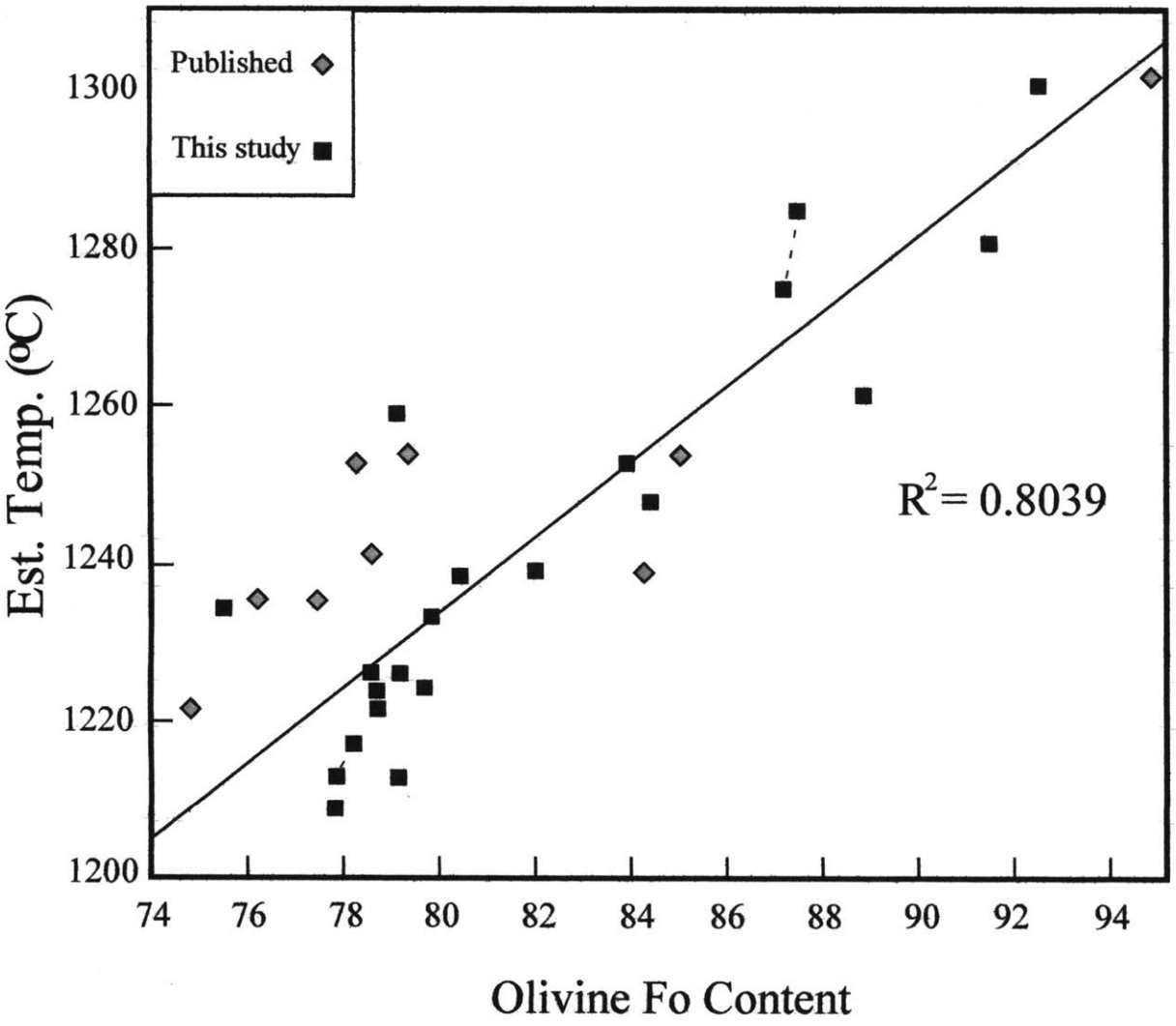
Published
This study
1300
1280
1260
1240
1220
1200
Est. Temp. (°C)
74
76
78
80
82
84
86
88
90
92
94
Olivine Fo Content
R^2= 0.8039

Figure 11.

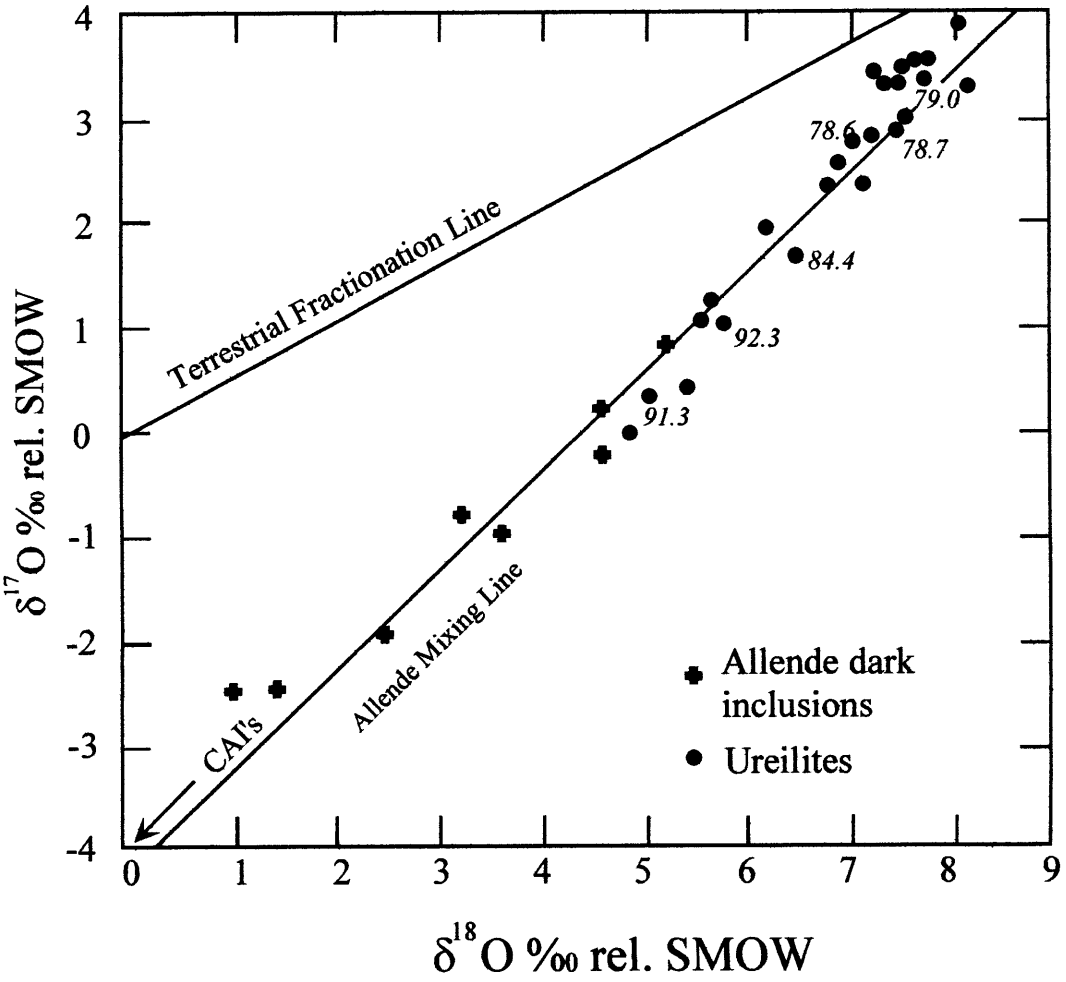
Terrestrial Fractionation Line
Allende Mixing Line
CAI's
Allende dark inclusions
Ureilites
79.0
78.6
78.7
84.4
92.3
91.3
δ^{17}O ‰ rel. SMOW
δ^{18}O ‰ rel. SMOW

Figure 12.

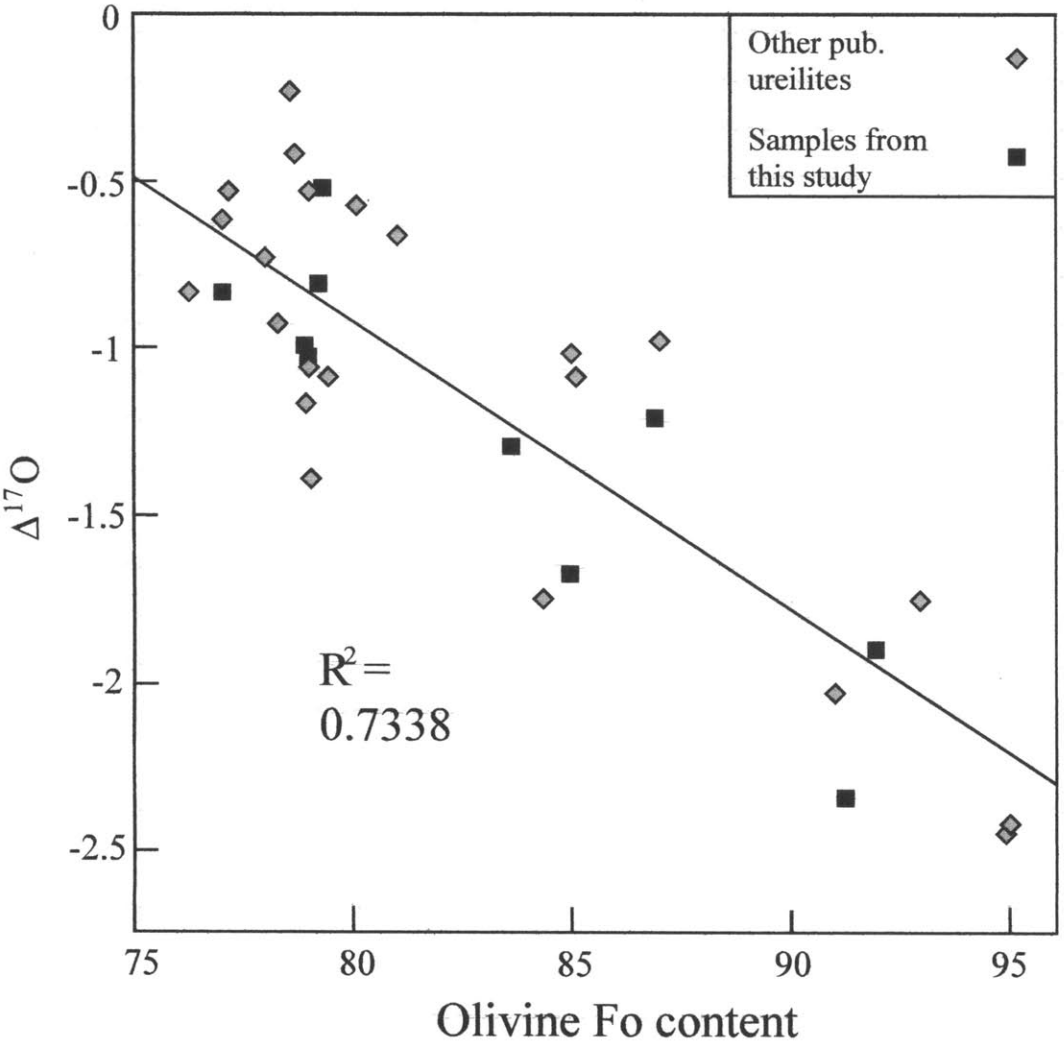
Other pub. ureilites
Samples from this study
R^2 = 0.7338
$\Delta^{17}O$
0
-0.5
-1
-1.5
-2
-2.5
75
80
85
90
95
Olivine Fo content

TABLE 1. Modal proportions of ureilites examined in this study.

Ureilite	Olivine[1] Modal %	Percent of total[1] olivine in reduced rims	Olivine mg #	Pigeonite[1] Modal %	Pigeonite grain mapping[2] % Metal	wt% C[3]
A 881931	77	0.0	79.2	14	0.7	
ALHA78262	76	0.0	78.7	21	1.3	
Dar Al Gani 340	79	33.6	79.7	19	0.6	
Dingo Pup Donga	35	53.9	83.9	49	1.4	1.7
EET 83225	59	0.0	88.7	41	1.3	
EET 87517	45	0.0	92.3	55	1.3	
EET 96293	34	0.0	87.5	56	1.5	
EET 96314	54	0.0	87.2	45	1.1	
El Gouanem	82	16.8	80.5	18	2.1	
GRA 95205	94	0.0	79.1	5	2.6	
GRO 95575	90	48.7	78.7	9	1.3	
GRO 95608	69	25.0	77.8	30	0.9	
Kenna	78	38.0	78.7	20	1.3	2.0
Lew 87165	67	6.3	84.4	31	1.6	
Novo Urei	77	52.6	78.6	22	0.8	2.3
QUE 93336	81	44.9	77.9	20	1.8	
QUE 93341	49	60.3	78.3	51	1.1	
Y 74123	70	16.3	79.9	24	0.5	2.9
Y 74659	63	1.6	91.8	36	0.7	
Y 791839	77	15.8	75.7	15	2.1	
Y 82100	64	15.0	82.0	32	0.6	

[1] Modal proportions obtained by image analysis of Mg x-ray maps.

[2] Percent of pigeonite grains as metal obtained by image analysis of back scattered electron images.

[3] Data from Grady et al., 1985.

TABLE 2. Experimental bulk compositions

	SiO_2	Al_2O_3	TiO_2	Cr_2O_3	FeO	MnO	MgO	CaO	K_2O	Na_2O	Total
PTL mix	46.50	8.20	0.50	1.00	14.70	0.36	19.10	8.10	0.02	1.50	99.98
Pu mix	54.09	6.56	0.52	0.76	14.36	0.21	9.80	13.72	-[a]	-	100.01
PU + 20% oliv	51.68	5.24	0.42	0.61	14.58	0.16	16.79	10.97	-	-	100.45

[a] - indicates oxide not added to mix.

TABLE 3. Experimental run conditions and results.

Run #	T (C)	P (MPa)	Phase*	SiO_2	TiO_2	Al_2O_3	Cr_2O_3	FeO	MnO	MgO	CaO	Na_2O	Total	Mg#	$^{(Mg,Fe)}K_d^{xtal/L}$
Ptl 5	1200	7.5	Olivine (10)	38.7 (3)[a]	-[b]	-	0.51 (6)	16.8 (2)	0.36 (2)	43.3 (5)	0.50 (3)	-	100.2	82.1	0.32
			Glass (24)	52.2 (5)	0.61 (9)	12.1 (1)	0.41 (6)	10.3 (2)	0.26 (3)	8.4 (1)	12.9 (3)	3.2 (3)	100.4	59.4	-
Ptl 6	1173	7.5	Olivine (20)	38.6 (5)	-	-	0.36 (5)	19.4 (3)	0.44 (4)	40.2 (9)	0.55 (6)	-	99.6	79.3	0.31
			Glass (25)	51.6 (5)	0.81 (3)	13.8 (2)	0.23 (3)	10.4 (2)	0.30 (2)	6.7 (2)	11.1 (3)	4.7 (2)	99.6	53.3	-
			Augite (8)	51.9 (5)	0.35 (7)	2.3 (9)	1.4 (1)	6.1 (3)	0.25 (4)	17.0 (8)	20.0 (6)	0.5 (2)	99.8	82.3	0.23
Ptl 7	1150	7.5	Olivine (11)	38.0 (3)	-	-	0.27 (5)	22.6 (4)	0.51 (3)	38.4 (5)	0.60 (4)	-	100.4	75.2	0.28
			Glass (15)	52.7 (4)	0.87 (7)	15.3 (2)	0.14 (8)	10.0 (2)	0.26 (3)	4.8 (3)	9.1 (2)	6.5 (4)	99.7	46.7	-
			Augite (11)	52.7 (4)	0.47 (7)	2.2 (7)	1.2 (3)	6.5 (5)	0.28 (4)	16.1 (6)	20.5 (4)	0.50 (9)	100.5	80.9	0.19
			Plag (6)	55.3 (1.1)	-	28.7 (1.1)	-	0.7 (2)	-	-	10.7 (2)	5.4 (3)	100.8		-
Ptl 8	1200	2.5	Olivine (7)	41.8 (4)	-	-	0.95 (3)	4.62 (8)	0.52 (3)	51.3 (7)	0.34 (3)	-	99.5	95.3	0.25
			Glass (8)	56.9 (2)	0.83 (3)	16.3 (1)	0.71 (3)	2.5 (2)	0.33 (3)	6.9 (1)	9.53 (8)	4.9 (3)	98.9	82.5	-
			Augite (4)	53.8 (3)	0.37 (4)	1.8 (1)	1.8 (1)	2.2 (5)	0.44 (4)	20.5 (3)	17.9 (8)	0.41 (8)	99.2	90.2	0.30
Ptl 9	1180	1.3	Olivine (8)	42.1 (4)	-	-	1.00 (8)	3.75 (7)	0.61 (3)	52.7 (7)	0.4 (2)	-	100.6	96.4	0.41
			Glass (3)	57.5 (4)	0.77 (9)	16.9 (1.6)	0.5 (1)	1.8 (2)	0.28 (2)	10.1 (8)	8.1 (9)	5.1 (4)	101.1	90.7	-
			Augite (3)	54.8 (4)	1.0 (6)	1.5 (2)	1.4 (1)	1.64 (9)	0.45 (4)	20.7 (7)	19.1 (8)	0.54 (4)	101.1	95.7	0.45
Pu 1	1220	1.5	Pigeonite (12)	57.6 (5)	0.19 (2)	0.6 (1)	0.76 (4)	3.5 (2)	0.16 (2)	33.4 (7)	4.4 (6)	-	100.6	94.5	0.20
			Glass (10)	61.0 (5)	0.79 (2)	13.5 (5)	0.32 (3)	3.3 (1)	0.14 (2)	6.3 (7)	13.6 (2)	-	99.0	76.8	-
			Augite (2)	55.5 (3)	0.29 (4)	0.82 (5)	0.6 (1)	2.56 (7)	0.20 (2)	22.5 (6)	18.9 (3)	-	101.4	91.8	0.22
Pu 2	1220	5	Pigeonite (7)	56.2 (3)	0.13 (3)	0.5 (2)	0.73 (5)	8.1 (2)	0.20 (2)	29.4 (4)	5.2 (4)	-	100.5	86.4	0.30
			Glass (16)	54.8 (3)	0.76 (3)	11.0 (1)	0.50 (3)	8.5 (1)	0.12 (2)	9.26 (8)	14.2 (2)	-	99.1	66.7	-
			Augite (4)	54.3 (4)	0.22 (5)	1.1 (3)	0.7 (1)	5.3 (6)	0.18 (4)	20.5 (4)	18.9 (9)	-	101.2	87.5	0.31
Pu 4	1220	7.5	Pigeonite (6)	55.9 (5)	0.09 (2)	0.4 (1)	0.66 (5)	10.7 (7)	0.22 (5)	27.2 (5)	5.8 (6)	-	101.3	82.2	0.54
			Glass (12)	58.9 (3)	0.80 (3)	11.2 (2)	0.48 (3)	6.27 (9)	0.2 (1)	8.9 (2)	13.7 (1)	-	100.5	72.2	-
			Augite (2)	54.7 (1)	0.17 (5)	1.0 (3)	0.72 (1)	6.1 (7)	0.25 (7)	20.3 (4)	17.9 (5)	-	101.1	87.5	0.43

* Number in parenthesis indicates # of analysis used for average.

[a] Number in parenthesis is one sigma standard deviation in terms of least units cited. Therefore, 38.7(3) should be read 38.7+/-0.3 wt%.

[b] - indicates element not analyzed or below detectability limit.

TABLE 4. Major phase compositions of ureilites used in this study.

Ureilite	T (°C)[a]	Phase	SiO_2	TiO_2	Al_2O_3	Cr_2O_3	FeO	MnO	MgO	CaO	Total	Mg#	Pyx Wo
A 881931	1213	Olivine (23)[b]	38.4 (4)	0.03 (1)	0.04 (1)	0.54 (3)	19.2 (1.6)	0.40 (4)	41.1 (1.4)	0.31 (2)	100.0	79.2	-[c]
		Pigeonite (18)	55.8 (3)	0.09 (1)	0.7 (1)	1.02 (4)	11.7 (2)	0.38 (4)	25.4 (4)	4.3 (3)	99.4	79.5	8.8
ALHA78262	1224	Olivine (10)	38.8 (3)	-	0.04 (1)	0.71 (3)	19.4 (4)	0.38 (4)	40.4 (2)	0.36 (2)	100.1	78.7	-
		Pigeonite (26)	55.7 (2)	0.05 (1)	0.77 (8)	1.15 (2)	12.0 (3)	0.39 (3)	26.6 (2)	4.0 (1)	100.7	79.8	7.9
Dar Al Gani 340	1224	Olivine (11)	40.0 (3)	0.04 (1)	0.06 (1)	0.81 (3)	18.7 (6)	0.42 (3)	41.2 (3)	0.40 (2)	101.6	79.7	-
		Pigeonite (15)	55.7 (9)	0.09 (1)	0.72 (7)	1.28 (2)	11.0 (2)	0.43 (5)	26.3 (1)	4.96 (8)	100.5	80.9	9.8
Dingo Pup Donga	1253	Olivine (15)	39.9 (2)	0.02 (1)	0.03 (1)	0.69 (2)	15.0 (4)	0.40 (3)	43.9 (2)	0.31 (3)	100.3	83.9	-
		Pigeonite (14)	57.4 (4)	0.04 (2)	0.32 (5)	0.91 (3)	9.7 (2)	0.36 (3)	29.5 (2)	2.33 (6)	100.6	84.4	4.6
EET 83225	1261	Olivine (9)	40.8 (3)	-	0.04 (1)	0.65 (2)	10.8 (3)	0.53 (2)	47.8 (2)	0.38 (2)	101.0	88.7	-
		Pigeonite (21)	55.9 (4)	0.11 (2)	0.5 (2)	0.9 (1)	6.5 (1)	0.39 (9)	28.9 (3)	5.7 (4)	98.9	88.7	11.2
EET 87517	1301	Olivine (16)	41.3 (2)	-	0.02 (1)	0.38 (3)	7.6 (6)	0.41 (4)	50.8 (5)	0.35 (2)	100.9	92.3	-
		Pigeonite (13)	58.4 (2)	0.13 (1)	0.50 (3)	0.58 (2)	4.8 (3)	0.36 (3)	33.7 (1)	2.53 (4)	101.0	92.6	4.7
EET 96293	1285	Olivine (12)	39.7 (2)	0.02 (1)	0.03 (1)	0.50 (1)	12.2 (3)	0.50 (2)	47.8 (3)	0.28 (1)	101.0	87.5	-
		Pigeonite (12)	57.5 (3)	0.10 (1)	1.03 (9)	0.81 (5)	7.65 (9)	0.56 (3)	31.0 (2)	2.32 (4)	100.9	87.9	4.5
EET 96314	1274	Olivine (24)	39.7 (2)	0.02 (1)	0.03 (1)	0.51 (2)	12.4 (3)	0.50 (3)	47.5 (2)	0.28 (1)	100.9	87.2	-
		Pigeonite (12)	56.6 (7)	0.11 (2)	1.15 (3)	1.00 (1)	8.0 (8)	0.48 (3)	31.2 (4)	2.48 (9)	101.0	87.4	4.7
El Gouanem	1239	Olivine (12)	38.2 (2)	-	0.02 (1)	0.66 (7)	17.7 (5)	0.43 (5)	41.4 (4)	0.33 (5)	98.7	80.5	-
		Pigeonite (27)	55.3 (4)	-	0.46 (5)	1.11 (8)	10.9 (2)	0.45 (4)	27.5 (3)	4.0 (1)	99.7	81.8	7.8
GRA 95205	1259	Olivine (13)	39.0 (2)	-	0.04 (3)	0.67 (5)	19.2 (2)	0.38 (3)	40.9 (4)	0.27 (6)	100.5	79.1	-
		Pigeonite (15)	56.2 (8)	0.05 (2)	0.20 (5)	1.12 (9)	7.6 (1.7)	0.50 (3)	30.5 (9)	4.0 (5)	100.2	87.7	7.6
GRO 95575	1222	Olivine (10)	38.9 (2)	0.02 (1)	0.02 (1)	0.83 (2)	19.3 (3)	0.40 (3)	40.0 (2)	0.39 (1)	99.9	78.7	-
		Pigeonite (21)	55.5 (3)	0.05 (1)	0.50 (1)	1.15 (3)	11.6 (1)	0.36 (3)	26.0 (1)	5.00 (8)	100.2	80.1	9.9
GRO 95608	1209	Olivine (10)	38.7 (2)	-	0.04 (1)	0.56 (2)	20.0 (5)	0.39 (4)	39.6 (2)	0.26 (1)	99.6	77.8	-
		Pigeonite (25)	55.2 (3)	0.09 (1)	1.10 (4)	1.25 (4)	11.8 (2)	0.44 (3)	24.9 (1)	5.59 (7)	100.4	79.1	11.2
Kenna	1227	Olivine (21)	38.4 (2)	0.02 (1)	0.03 (1)	0.71 (3)	19.5 (6)	0.36 (4)	40.6 (5)	0.31 (2)	99.9	78.7	-
		Pigeonite	54.7 (4)	0.09 (1)	0.62 (2)	1.14 (3)	11.7 (2)	0.38 (2)	26.4 (3)	4.88 (9)	99.9	80.0	9.6
Lew 87165	1248	Olivine (28)	39.5 (5)	0.06 (1)	0.02 (1)	0.73 (5)	14.7 (1.6)	0.46 (2)	44.5 (1.3)	0.36 (2)	100.3	84.4	-
		Pigeonite	56.3 (2)	0.08 (1)	0.50 (1)	1.11 (2)	9.59 (9)	0.43 (3)	28.6 (5)	3.66 (7)	100.3	84.2	7.1
Novo Urei	1227	Olivine (19)	38.8 (3)	-	0.04 (1)	0.71 (6)	19.4 (4)	0.38 (3)	39.9 (3)	0.35 (2)	99.6	78.6	-
		Pigeonite	53.9 (3)	0.09 (1)	0.95 (5)	1.24 (5)	11.4 (1)	0.41 (3)	26.0 (2)	4.9 (1)	98.9	80.3	9.8
QUE 93336	1213	Olivine (24)	38.9 (2)	0.02 (1)	0.08 (2)	0.54 (3)	20.2 (3)	0.41 (4)	39.9 (2)	0.31 (2)	100.4	77.9	-
		Pigeonite	54.9 (2)	0.10 (1)	1.21 (9)	1.19 (4)	11.8 (1)	0.37 (5)	25.2 (3)	5.05 (9)	99.8	79.1	10.2

[a] Temperature inferred from olivine-pigeonite-liquid thermometer [1], see text.

[b] See table 3 for explanation of parenthesis.

46 indicates element not analyzed or below detectability limit.

TABLE 4. Major phase compositions of ureilites used in this study (cont.)

Ureilite	T (°C)	Phase	SiO_2	TiO_2	Al_2O_3	Cr_2O_3	FeO	MnO	MgO	CaO	Total	Mg#	Pyx Wo
QUE 93341	1217	Olivine (13)	38.9 (3)	0.02 (1)	0.08 (1)	0.56 (3)	20.0 (9)	0.42 (4)	40.5 (7)	0.30 (1)	100.8	78.3	-
		Pigeonite (14)	54.9 (3)	0.07 (1)	0.61 (1)	0.99 (5)	12.1 (3)	0.33 (4)	25.5 (2)	4.6 (1)	99.1	79.0	9.2
Y 74123	1234	Olivine (17)	38.7 (2)	0.03 (1)	0.03 (1)	0.80 (6)	18.8 (6)	0.42 (3)	41.9 (5)	0.39 (2)	101.1	79.9	-
		Pigeonite (2)	56.0 (1)	0.05 (1)	0.42 (1)	1.09 (0)	12.0 (1)	0.42 (2)	27.3 (3)	3.27 (2)	100.6	80.3	6.4
Y 74659	1280	Olivine (20)	40.5 (3)	0.02 (1)	-	0.52 (2)	7.9 (9)	0.40 (2)	50.1 (9)	0.3 (1)	99.7	91.8	-
		Pigeonite (1)	57.70	0.08	0.41	0.75	5.51	0.42	31.30	3.61	99.8	91.0	6.9
Y 791839	1235	Olivine (8)	38.5 (1)	-	-	0.65 (5)	21.9 (3)	0.39 (4)	38.2 (2)	0.34 (4)	100.4	75.7	-
		Pigeonite (14)	56.9 (5)	0.03 (2)	0.3 (2)	1.11 (6)	9.1 (1.2)	0.36 (4)	27.0 (9)	6.0 (1.1)	100.8	84.1	11.7
Y 82100	1240	Olivine (16)	38.9 (2)	0.02 (1)	0.02 (1)	0.81 (2)	16.8 (3)	0.41 (2)	43.1 (3)	0.41 (1)	100.5	82.0	-
		Pigeonite (17)	56.1 (3)	0.06 (2)	0.4 (3)	1.13 (2)	10.24 (2)	0.40 (3)	27.8 (4)	4.6 (2)	100.7	82.9	8.9

Chp. 2. Experimental Constraints on Ureilite Petrogenesis

Abstract

This experimental study explores the petrogenesis of ureilites by a partial melting/smelting process. Experiments have been performed over temperature (1150-1280°C), pressure (5 to 12.5 MPa) and low oxygen fugacity (graphite-CO gas) conditions appropriate for a hypothetical ureilite parent body ~200 km in size. Experimental and petrologic modeling results indicate that a partial melting/smelting model of ureilite petrogenesis can explain many of the unique characteristics displayed by this meteorite group. Compositional information preserved in the pigeonite-olivine ureilites was used to estimate the composition of melts in equilibrium with the ureilites. The results of twenty experiments saturated with olivine, pyroxene, metal and liquid with ureilite appropriate compositions are used to calibrate the phase coefficients and pressure-temperature dependence of the smelting reaction. The calibrated coefficients are used to model the behavior of a hypothetical residue that is experiencing fractional smelting. The residue is initially olivine-rich and smelting progressively depletes the olivine content and enriches the pyroxene and metal contents of the residues. The modeled residue composition at 1260°C best reproduces the trend of ureilite bulk compositions. The model results also indicate that as a ureilite residue undergoes progressive heating, Ca/Al values and Cr_2O_3 contents are enriched at lower temperatures (below ~1240°C) and tend to decrease at higher temperatures. Fractional smelting, as we model it, can account for the high Ca/Al and Cr_2O_3 wt% values observed in ureilites. We propose that ureilites were generated from a residue that was initially olivine-rich and cpx bearing. These residues experienced varying degrees of fractional smelting to produce the compositional variability observed within the pigeonite bearing ureilites. Variations in mineral composition, modal proportions and isotopic signatures are best described by heterogeneous accretion of the ureilite parent body followed by minimal and variable degrees of igneous processing.

Introduction

Ureilites are primitive achondrites that consist of olivine, pyroxene and carbon. They represent the second largest achondrite group but their petrogenesis remains enigmatic. Ureilites display equilibrated coarse-grained textures and mineral chemistry but retain primordial gas contents and isotope signatures.

A wide variety of models have been put forward to explain ureilite petrogenesis. Goodrich *et al* (1987) developed a multi-stage cumulate model based on mineral chemistry and textures. In the model, ureilites represent cumulates from a magma

generated by <10% partial melting of a plagioclase depleted source that had superchondritic Ca/Al ratios. Ureilites would therefore represent only a small fraction of the amount of material that was processed. The most likely precursor materials, carbonaceous chondrites, do not have superchondritic Ca/Al ratios and formation of the ureilites from them would require more than one melting event. Since ureilites are the second most abundant achondrite, the complementary material should be present in our collections. No meteorite type complementary to the ureilites, either residues of the original partial melting or the subsequent basaltic magma left after ureilite accumulation, has been described (Rubin, 1988).

Residue models to explain the ureilites have also been proposed (Boynton *et al,* 1976; Scott *et al,* 1993; Wasson *et al,* 1976). A difficulty for these models is accounting for the strong mineral alignments observed in some ureilites (Berkley *et al,* 1980; Rubin, 1988) that suggest a cumulate origin. However, experimental evidence suggests fabrics can be produced in a residue by thermal compaction (Walker and Agee, 1988). The high carbon content of the ureilites was accounted for by impact of a carbon-rich body. However, this does not explain the presence of carbide-bearing spherules (up to 100 μm) within olivine (Goodrich and Berkley, 1986) or the presence of large, bladed graphite crystals in low shock ureilites (Berkley and Jones, 1982).

Takeda (1987) proposed that ureilites represent nebular condensates that underwent high temperature recrystallization during the early stages of planetesimal collision. If this was the case, ureilites should have higher sulfur contents than they do (Rubin, 1988), as sulfide melts do not readily separate from a crystalline silicate melt (Walker and Agee, 1988).

Smelting of an olivine-rich source has also been suggested as a petrogenetic process to account for the ureilites (e.g. Warren and Kallemeyn, 1992; Walker and Grove, 1993). The amount of smelting is controlled by C-O-Fe equilibria which are strongly pressure dependent. At low pressures (2.5 MPa) FeO in silicates is unstable and is reduced to Fe metal, producing MgO-rich silicates and a CO gas. Above 10 MPa smelting is suppressed and Fe silicates coexist with graphite (Walker and Grove, 1993). Therefore, the less smelted ureilite samples record greater depths in the parent body, and the more smelted samples record shallow depths. Many authors have argued that if smelting had occurred, there should exist correlations between the modal percentage of pyroxene, metal content and mg# (defined here as molar MgO/[MgO+FeO]) (e.g. Goodrich, 1992; Mittlefehldt *et al,* 1998). Singletary and Grove (2003) established this correlation using quantitative petrologic study of 21 ureilites.

Ureilite petrography and petrology

The typical ureilite texture is characterized by elongated, anhedral pyroxene and olivine grains ~1 mm in size with curved intergranular boundaries that generally meet in triple junctions. Pigeonite, augite and orthopyroxene all occur in ureilites however, pigeonite is the sole pyroxene in ~77% of ureilites (Mittlefehldt *et al,* 1998). Where pigeonite is the sole pyroxene present, it shows no exsolution lamellae and is inferred to have cooled rapidly from high temperature. Augite is present in ~10% of ureilites as small irregular blebs and lamellae in pigeonite and as larger, discrete crystals. Orthopyroxene is also present in a small number of ureilites, predominantly as large crystals poikilitically enclosing other pyroxenes (Takeda *et al,* 1989).

Olivine in ureilites ranges in composition from Fo_{74} to Fo_{95} and is characterized by high Cr_2O_3 (~0.56 – 0.85 wt%) and CaO (~0.30 – 0.45 wt%) contents (Mittlefehldt *et al,* 1998). A characteristic feature of the ureilites is the presence of reduced rims on olivine where in contact with the carbon rich matrix and where crosscut by veins of carbon-bearing material (Berkley *et al,* 1980). The rims are most prominent on olivine, but can be observed on other silicate phases to varying degrees. The olivine rims are composed of nearly pure forsterite, Ni-free metal blebs and enstatite. The rims vary in width from 10 to 100 μm and display sharp contacts with the interior of the grains (Mittlefehldt *et al,* 1998). The rims are hypothesized to be a feature produced late in ureilite petrogenesis at fairly high temperature (~1100°C)(Sinha *et al,* 1997).

Carbon occurs predominantly as fine-grained graphite in an interstitial matrix that also contains fine-grained silicates, metal, sulfides and phosphides (Mittlefehldt *et al,* 1998). Rare, mm-sized euhedral graphite crystals have been observed in some ureilites (Treiman and Berkley, 1994). Other polymorphs of carbon that have been identified in ureilites include diamond and lonsdaleite as well as chaoite and organic compounds (Vdovykin, 1970).

The olivine and pyroxene core compositions are homogeneous within grains and between grains in a single meteorite in terms of mg#. However, between meteorites, significant variability exists in mineral chemistry and modal proportions. Olivine forsterite contents range from 74 to 95 with coexisting pyroxenes having mg#s in the -same range, indicating Fe-Mg equilibrium between olivine and pyroxene (Mittlefehldt *et al,* 1998). The modal percent pigeonite varies from 0% in LEW86216 to 100% in MET 01085. A correlation of increasing modal percent pigeonite with higher silicate mg# was reported

by Singletary and Grove (2003) and is hypothesized to result from a primary, low-pressure partial melting event in the presence of carbon.

A long standing debate on ureilite petrogenesis has centered on whether the rocks represent the residues of a partial melting process or a cumulate pile resulting from fractional crystallization of a large body of magma on the ureilite parent body. The meteorites are very coarse-grained, containing olivine and pigeonite that average from 1 to 3 mm in length, with grains as large as 15 mm (Mittlefehldt *et al,* 1998). The grain boundaries are smooth and curved with abundant 120° triple junctions (Goodrich, 1992). In some ureilites, the silicate grains are elongate and the long crystal axes define weak foliations and lineations (Berkley *et al,* 1976; Berkeley *et al,* 1980). In spite of textures that might indicate extensive processing and equilibrated mineral compositions, the ureilites retain several geochemical characteristics of primitive, unprocessed nebular material.

The most striking primitive characteristic is the oxygen isotope signature. Ureilites plot along a line of slope 1 that is defined by end members of carbonaceous chondrite and anhydrous minerals (CCAM)(Clayton and Mayeda, 1988; 1996)(Figure 1). Any high temperature, planetesimal-scale igneous process should fractionate the oxygen isotopes such that they lie along a line with slope of 0.52 (i.e. the lines defined by samples of Mars, Moon, Earth and 4 Vesta). Ureilites also retain noble gases in chondritic abundances (Weber *et al,* 1976). The oxygen isotopic signature and noble gas abundances suggest that ureilites have experienced minimal amounts of processing. The key to ureilite petrogenesis lies in reconciling the overwhelming petrographic evidence

that suggests extensive igneous processing with these primitive geochemical characteristics.

Here we present new experimental results to constrain the amount of processing required to generate the ranges of mineral chemistry and modal proportions observed in ureilites. We hypothesize that olivine-pigeonite bearing ureilites represent the residues of partial melting. The presence of carbon and low pressures on the ureilite parent body combined to create an environment in which a smelting reaction occurred. Smelting for the purposes of this discussion is defined as the reaction:

$$\text{olivine} + \text{liquid} + \text{carbon} \rightarrow \text{pigeonite} + \text{Fe metal} + \text{CO gas.} \quad (1)$$

As the reaction proceeds, Fe metal is sequestered and the mg# of the major silicate phases rises. We posit that the relationship of modal percent pigeonite and mg# reported by Singletary and Grove (2003) is a consequence of this reaction. Petrologic modeling using the experimental data also suggests smelting may be responsible for the high olivine Cr_2O_3 contents and enriched Ca/Al ratios observed in ureilites.

Procedures

All experiments reported here were performed in the MIT Experimental Petrology Laboratory. The bulk compositions used in the experiments are given in Table 1. Experimental run conditions and products are reported in Table 2. For this study five bulk compositions were selected (see discussion).

The starting material was prepared by mixing together high purity reagent grade oxides and Fe° sponge (Grove and Bence, 1977). Grinding under ethanol for ~6 hours produced a uniform powder. Approximately 10 to 15 mg of the starting powder was packed into a

handcrafted carbon capsule. The carbon capsule was then inserted into a platinum tube that was welded shut on one end and loosely crimped on the other. A small hole was made in the crimped end to ensure the gas pressure was fully transmitted to the interior of the experimental charge. The finished assembly, with the welded end at the bottom, was loaded into the pressure vessel.

The experiments were performed in a rapid quench, externally heated, ZHM alloy, cold seal pressure vessel contained in an inconel 600 sheath. The pressure vessel has an inner diameter of 0.25" and was surrounded by argon to prevent oxidation. Once sealed, the vessel is pressurized with CO gas, that serves both as the pressure medium and to ensure a reducing environment. The vessel is then placed in a vertical Del Tech furnace and brought to run temperature. At the end of the experiment, the vessel is extracted from the furnace and inverted to drop the experimental charge to the cold region of the vessel. Rapping the end of the pressure vessel with a wrench assists in making sure the charge falls to the cooling head.

Experiments were then removed from the pressure vessel and extracted from the Pt tube and carbon capsule. Frequently the experiment would come out as one coherent glass bead, other times as a loose aggregate of glass beads and crystals. The bead(s) and/or crystals were then crushed in a Plattner mortar and mounted in epoxy. The mounts were then polished and carbon coated for microprobe analysis (see Fig. 2 for examples of prepared experimental products).

Microprobe analysis was performed using the MIT JEOL 733 Superprobes utilizing the appropriate glass and silicate standards. Crystal phases in the experiments were analyzed using a beam current of 10 nA, accelerating voltage of 15 kV and a spot size of 2 μm.

Glasses were analyzed under the same conditions but with a spot size of 10 μm to reduce the effects of small quench phases. The CITZAF correction package of Armstrong (1995) was used to reduce the data. The atomic number correction of Duncomb and Reed, the Heinrichs tabulation of absorption coefficients, and the fluorescence correction of Armstrong were used to obtain a quantitative analysis (Armstrong, 1995).

Experimental Results

Approach to equilibrium

Experiments performed in this study are all synthesis experiments where crystals and melt have grown from an oxide mix. Phase appearance temperatures have not been reversed because past experience (Grove and Bence, 1977) indicates that direct synthesis is sufficient to recover equilibrium appearance temperature when significant (>40 wt%) melt is present. For the reasons detailed below, we conclude that the experiments approached equilibrium sufficiently so that they can be used to understand the smelting reaction behavior under the conditions of this study. A materials-balance technique (Bryan *et al,* 1969) was used to estimate the phase proportions in the experimental products and to asses the gain or loss of material. The phase proportions and sum of squared residuals for each run are reported in Table 2. If no material was gained or lost during the experiment, the sum of squared residuals should be less than 1 (0 in the ideal case). A sum of squared residuals less than 1 is the first criterion for determination of a successful experiment. A second criterion for equilibrium is the achievement of regular and consistent partitioning of Fe and Mg between olivine, pyroxene and melt. The oliv-melt and pyroxene-melt Fe-Mg exchange distribution coefficients ($K_D^{Fe\text{-}Mg}$ =

$[X_{Fe}^{(Ol,Pyx)}X_{Mg}^{Liq}]/[X_{Mg}^{(Ol,Pyx)}X_{Fe}^{Liq}]$) are reported in Table 2. The reported Fe-Mg K_D values are well behaved and are similar to values reported for other systems (e.g. Grove *et al,* 2003). We proceed assuming the experiments are sufficiently close to equilibrium based on the materials balance calculations and systematic Fe-Mg K_D values.

To investigate smelting as it applies to ureilites, experiments were performed to obtain an assemblage of olivine, pigeonite, metal and liquid with mg# of 75. Compositional, pressure and temperature space were explored to obtain the correct assemblage and then to ascertain how the modal proportions of the phases may vary with mineral chemistry. The experimental results were then used to calibrate the coefficients of the smelting reaction for the ureilite appropriate bulk composition. The various bulk compositions used in this study are reported in Table 1.

Pu+Fo$_{83}$

The first bulk composition used in this study is a mix of a calculated liquid (Pu from Singletary and Grove (2003) see Table 1) and Fo_{83} olivine in a ratio of 71:29. The amount of olivine was increased from that of the experiments reported in Singletary and Grove (2003) to obtain olivine saturation. The bulk composition plots to the left of the opx-cpx join in the Ol-Cpx-Qtz ternary diagram within the olivine primary phase volume (Fig. 3a).

Ten experiments were performed with this composition over a pressure range of 50 to 125 bars and temperatures of 1200 to 1280°C. The experimental set is shown graphically in Figure 4a and run products are plotted in the Ol-Cpx-Qtz ternary in Figure 3a. All runs at 125 bars are saturated with metal, olivine, pigeonite and liquid. The mg#s for olivine and pigeonite decrease from 83 and 85 at 1280°C to 78 and 79, respectively, at 1200°C in

a regular fashion. The Wo content ranges from 6.6 to 12.2. The pigeonites all plot along the opx-cpx join in the Ol-Cpx-Qtz ternary. The liquids plot along the olivine-pigeonite reaction boundary but below the 1-atm olivine-pigeonite-augite-liquid reaction point. Two runs at 100 bars are also saturated with metal, olivine, pigeonite and liquid. The mg#s of the olivine and pigeonite also decrease with decreasing temperature from 83 and 85 to 79 and 81, respectively. These are higher than those of the same phases at the same temperature at 125 bars (see Fig. 4a). Olivine is absent from all experiments below 100 bars. Two experiments at 1230°C; 80 bars and 1260°C; 75 bars contain metal, pigeonite and liquid as saturating phases. The mg#s of the pigeonite are higher than those at the same temperature but higher pressure and display the same decrease of mg# with decreasing temperature (87 to 85). Two experiments at 50 bars contain pigeonite, augite, metal and liquid.

Pu+Fo$_{75}$

The second bulk composition is a mix of the calculated liquid in equilibrium with a Fo$_{83}$ bearing ureilite with 29% Fo$_{75}$ olivine added. Two experiments were performed with this composition at 1260°C and pressures of 75 and 125 bars (Fig. 4b). The higher pressure run contains metal, olivine (Fo$_{78}$), pigeonite (mg#79) and liquid. The lower pressure experiment is saturated with augite, pigeonite, metal and liquid. The pigeonite mg#s are slightly higher than those in the Pu + Fo$_{83}$ experimental set at the same temperature and pressure. All the pyroxenes plot along the opx-cpx join in the Ol-Cpx-Qtz ternary (Fig 3b). The liquids plot near the calculated Pu composition.

ULM

A second equilibrium liquid (ULM) was calculated using the method of Singletary and Grove (2003). ULM is calculated to be in equilibrium with the silicate portion of an ureilite with mg#s of 75-76 (Table 1). The bulk composition plots to the right of the opx-cpx join, along the olivine-pigeonite reaction boundary (fig. 3c).

Three experiments at 115 bars are saturated with pigeonite, metal and liquid (fig. 4c). The mg# of the pigeonite decreases from 84.6 at 1260°C to 72 at 1150°C. The pigeonite plots along the opx-cpx join (Fig 3c). The liquids plot along the olivine-pigeonite reaction boundary above the bulk composition but below that of the Pu liquid composition.

ULM+Fo_{75}

The fourth set of experiments uses a bulk composition of 71% ULM and 29% Fo_{75}. The addition of olivine pulls the bulk composition to the left of the opx-cpx join into the olivine primary phase volume (Fig 3d). Six experiments span a temperature-pressure range of 1180 to 1300°C and 75 to 125 bars (Fig 4d). All of the runs are saturated with metal, olivine, orthopyroxene and liquid. Mg#s of olivine and orthopyroxene range from 86 and 87, respectively, at 1230°C; 75 bars down to 72 and 70 at 1180°C; 110 bars. The pyroxene Wo contents vary from 2.2 to 9.6. As in the previous experiments, the mg#s decrease with decreasing temperature and increase with decreasing pressure.

The pyroxenes scatter along the opx-cpx join near the opx end. The liquids are more dispersed than in the previous experiments but scatter about the ULM bulk composition (Fig 3d).

ULM+Fo_{75}+CPX

The fifth bulk composition is a mixture of 76% ULM, 19% Fo_{75} olivine and 5% clinopyroxene with a mg# of 76. The bulk composition plots above the previous composition in the Ol-Cpx-Qtz ternary but still in the olivine primary phase volume (Fig 3e). Experiments were conducted from 50 to 115 bars and from 1160 to 1280°C (Fig 4e). Twenty experiments with this bulk composition are saturated with metal, olivine, pigeonite and liquid. Three experiments at 115 bars and below 1190°C contain plagioclase as an additional saturating phase.

The olivine Fo content at 115 bars and 1280°C is 81.4 and decreases to 73.9 at 1160°C. At 90 bars, the high temperature experiment contains $Fo_{86.3}$ olivine. The Fo content decreases to 76.3 at 1175°C. Olivine Fo contents at 75 bars decrease from 90.2 at 1280°C to 76.2 at 1175°C. One experiment at 55 bars, 1200°C contains $Fo_{77.2}$ olivine. Pigeonite mirrors the coexisting olivine with mg# decreasing with decreasing temperature and increasing with decreasing pressure. The experimental pyroxenes all plot along the opx-cpx join. The experimental liquids all cluster along the olivine-pigeonite reaction boundary, above the ULM liquid composition.

Several different bulk compositions were used in this study and there are similarities in all the experimental sets. Even though the experimental assemblages differ slightly, they all display the same behavior in regards to the relationships between mg#, pressure and temperature. As pressure decreases at constant temperature, the mg# of the silicate phases rise. Conversely, as temperature drops at constant pressure the mg# of the silicate phases drops.

Smelting Reaction Calibration

The smelting reaction coefficients are calculated in two ways – subtraction of modal proportions (SMP) and by mass balance (MB). The reaction is most sensitive to pressure, therefore, pairs of experiments at the same temperature and different pressures are used in the calculation.

The SMP method subtracts the modal proportions of the phases in an experiment from the proportions of the phases in a higher pressure experiment. The modal proportions of each experiment are calculated by performing a mass balance against the starting composition and are reported in Table 2. Phases with like signs after subtraction are placed on the same side of the reaction. The coefficients are then normalized to 1 liquid. The computed coefficients are reported in Table 3. If the sum of both sides were within 10%, the sides were normalized to 1 for comparison and are reported in Table 4.

The three experiments at 1280°C provide two set of calibration pairs. Even though in both cases the sums of the sides are not with 10%, the metal coefficient is nearly equal to or greater than that of the pyroxene. At 1260°C, three pairs of experiments yield sums within 10% and give average coefficients (in wt%) of:

$$0.05\ C + 0.77\ Ol + 1\ Liq \Rightarrow 1.47\ Pyx + 0.24\ Fe + 0.12\ CO \quad (2)$$

Five experimental pairs are available at 1230°C, however, only three have sides that sum to within 10%. They yield average reaction coefficients of:

$$0.27\ C + 1.56\ Ol + 1\ Liq \Rightarrow 2.03\ Pyx + 0.40\ Fe + 0.20\ CO \quad (3)$$

Two calibration pairs at 1200°C yield average coefficients of:

$$0.04\ C + 1.16\ Ol + 1\ Liq \Rightarrow 1.94\ Pyx + 0.18\ Fe + 0.09\ CO \quad (4)$$

The normalized coefficients in Table 4 show a general increase in the amount of metal produced as temperature increases. In contrast, the amounts of olivine and liquid consumed remain fairly constant.

The MB method uses the same experimental pairs as the SMP method. More experimental pairs were used because this method does not require the modal proportions of the experiments be precisely known. The analyses of all the experimental phases in the lower pressure experiment are mass balanced against the liquid of the higher pressure experiment to yield proportions of the phases that have been removed or added. The proportion of liquid after the mass balance is subtracted from 1 and the proportions of the all the phases are then normalized to 1 liquid as in the previous method (Table 3). When the sums of both sides are within 10%, they are normalized to 1 for comparison (Table 4). Two calibration pairs at 1280°C yield average smelting reaction coefficients of:

$$0.13\ C + 0.40\ Ol + 1\ Liq \Rightarrow 0.54\ Pyx + 0.63\ Fe + 0.32\ CO. \quad (5)$$

Three calibration pairs at 1260°C give average coefficients of:

$$0.04\ C + 0.77\ Ol + 1\ Liq \Rightarrow 1.62\ Pyx + 0.16\ Fe + 0.08\ CO \quad (6)$$

similar to those obtained from the SMP method at 1260°C. Three calibration pairs at 1230°C also yield similar results to the SMP calibration at 1230°C:

$$0.09\ C + 1.38\ Ol + 1\ Liq \Rightarrow 1.93\ Pyx + 0.41\ Fe + 0.20\ CO. \quad (7)$$

Even though seven experimental pairs are available at 1200°C, only one has sums of both sides that are within 10%. The coefficients from that pair are:

$$0.01\ C + 0.29\ Ol + 1\ Liq \Rightarrow 1.33\ Pyx + 0.03\ Fe + 0.01\ CO. \quad (8)$$

The right side of the reaction is identical to that of the SMP calibration at 1200°C; however, the amount of olivine consumed is much less. The normalized coefficients

reported in Table 4 display a similar pattern to those calculated using the SMP method, with metal production increasing with higher temperatures – dramatically so at 1280°C. The coefficients calculated at 1260 and 1230°C by both methods are nearly identical. Since the MB technique has more calibration pairs that span a larger temperature range, the coefficients calculated from that method are used in the petrologic modeling.

Petrologic Modeling

Petrologic modeling was performed to assess the behavior of a residue that is undergoing smelting. A bulk composition was depleted by subtracting or adding olivine, metal, pigeonite and liquid in proportions as determined by the smelting reaction coefficients calculated in the preceding section. At each step, the compositions of the phases that are removed or added are calculated to be in equilibrium with the liquid. Each model run was performed isothermally, and each step through the model corresponds to decompression and approximates fractional smelting. The compositions of the residue and liquid are recalculated after each step as phases are added and subtracted.

The model inputs for each run include temperature, the proportions of olivine, metal and pigeonite to add or subtract at the given temperature, a residue composition and a liquid composition. Model runs were made using four temperatures for which the smelting reaction was calibrated and for which compositional data exist from the experimental set – 1280, 1260, 1230 and 1200°C. An additional model run was made at 1300°C using the compositions and coefficients from the 1280°C experiments. Results for a typical model run are shown in Table 5. A residue composition corresponding to 7%ULM: 91%Fo_{75}:2%Cpx was deemed appropriate to the ureilites (see discussion) and is reported

here. At each temperature, the composition of the highest pressure experimental liquid was used as the starting liquid composition. Olivine composition was determined by using a K_d^{Fe-Mg} of 0.33 and assuming equilibrium with the liquid. The pigeonite composition is calculated using a temperature dependent expression for Wo content determined from the experimental data (Fig. 5a). The En and Fs components are calculated assuming equilibrium with the liquid. The Al, Cr, and Ti contents of the pyroxene are also predicted using temperature dependent partition coefficients calculated from the experimental data (Fig. 6). The residues are plotted in Ol-Cpx-Qtz ternary space (Fig. 7). The olivine Fo contents are plotted against the number of model steps in Figure 8.

Examination of the calculated residue compositions plotted in Ol-Cpx-Qtz ternary space shows that as smelting proceeds, the residue composition migrates toward the olivine-pigeonite reaction boundary at temperatures of 1260°C and below. The 1200 and 1230°C model residue trends pass above the ureilite bulk compositions. The 1260°C model run passes directly through the ureilite model compositions and is the best fit to the bulk ureilite data using the 7%ULM:91%Fo_{75}:2% Cpx residue composition. At 1280°C, the residue composition moves away from the reaction boundary and toward olivine (Fig. 8). At temperatures above 1230°C, the metal coefficients from the reaction calibration are such that the mg# of the silicate phases rises as the reaction proceeds. At 1200°C, the amount of metal removed is small enough that the mg# of the silicate phases decreases as the reaction proceeds. The 1300 and 1280°C model runs are the only ones that produce olivine Fo contents of 90 and above.

Ca/Al Ratios

Ureilite Ca/Al ratios are significantly above chondritic, previously reported as averaging 4.2 x CI and as high as 14.5 x CI (Goodrich, 1992). Using the modal proportions and mineral analysis reported in Singletary and Grove (2003) we recalculate the Ca/Al ratios and find an average bulk ratio of 7.1 with an upper value of 19.5. The bulk Ca/Al ratios are plotted versus the estimated temperature from Singletary and Grove (2003) in Figure 9. The data display two general, albeit scattered, trends - increasing Ca/Al ratio at temperatures below ~1240°C and decreasing Ca/Al ratios above 1240°C.

The superchondritic Ca/Al values of the ureilites have always posed a problem for models of ureilite petrogenesis. The cumulate model of ureilite petrogenesis requires the magma from which olivine and pigeonite precipitate have superchondritic Ca/Al ratios. Such a magma would indicate a plagioclase depleted source material in the melting region and by inference some degree of igneous processing well before ureilite formation (Goodrich *et al,* 1987). The source material must also have superchondritic Ca/Al ratios in the residue model as well. Goodrich *et al* (1999) demonstrated that in a single stage melting model (<25-30% melting) to produce pigeonite bearing residues, the source must have had Ca/Al ratios of 2.5 to 3 x CI.

The Ca/Al ratios for the model residue compositions are plotted in Figure 10 versus the model step (or extent of smelting). Because all of the Ca and Al are carried in the pyroxene, the amount of pyroxene added to the residue dominates this value. The beginning value is slightly less than 1.5 and increases to over 2.5 at 1230°C. The same behavior is observed in the temperature range of 1200 to 1260°C. At 1280°C, the Ca/Al ratios do not rise as rapidly and increase to just over 1.5. The same behavior is observed

at 1300°C with the rise in Ca/Al ratio increasing less than at 1280°C. The change in behavior of the residue Ca/Al ratio as smelting proceeds between 1260 and 1280°C is largely controlled by the amount of pyroxene added to the residue. At high temperatures (>1280°C) the values of the metal and pyroxene coefficients are such that less pyroxene is being added to the residue compared to temperatures of 1260°C and below. This indicates that pyroxene addition is the primary control on the model residue Ca/Al value.

Cr_2O_3

Ureilites are also characterized by high Cr contents (Mittlefehldt *et al,* 1998). The pyroxene Cr_2O_3 contents of ureilite olivine are plotted in Figure 11 versus estimated temperature (Singletary and Grove, 2003). As seen in the Ca/Al data, there exist two trends. The pyroxene Cr_2O_3 wt% increases slightly at lower temperature and then trails off at high temperature (>1240°C).

The model residue Cr_2O_3 wt% is plotted in Figure 12 versus the model step. As with the Ca/Al values, all Cr_2O_3 is hosted in the model pyroxene and therefore, pyroxene addition dominates the residue values. The initial Cr_2O_3 is ~0.05 and increases rapidly at 1230°C to over 0.30 wt%. At 1280°C however, the increase in Cr_2O_3 increases minimally to just over 0.05 wt%. The Cr_2O_3 at 1300°C drops initially and gradually rises, but the Cr contents never recover to the initial value.

Discussion

Reconnaissance experiments reported in Singletary and Grove (2003) were performed to explore the temperature-pressure relations of the smelting reaction using an approximation of a primary liquid composition reported by Goodrich *et al* (2001).

Experiments using that composition were not saturated with the correct phases and were too Mg rich to be generally relevant to the range of compositions spanned by ureilites. A second bulk composition was then calculated to explore more Fe-rich compositions using a liquid (Pu) calculated to be in equilibrium with an average ureilite containing Fo_{83} olivine. Experiments demonstrated that such a liquid with 20% Fo_{83} olivine added was saturated with pigeonite, augite and metal (Singletary and Grove, 2003).

Experiments on the calculated liquid demonstrate saturation with olivine, pigeonite, metal and liquid over the pressures and temperatures of interest when 29% Fo_{83} olivine is added. However, the lowest mg# of the experimental phases was 78. In order to produce olivine with lower Fo content, 29% Fo_{75} olivine was added to the mix in place of the Fo_{83} olivine. As before, the experiments are saturated with olivine, pigeonite, metal and liquid. The lowest mg# again was 78.

A second equilibrium liquid (ULM) was then calculated using a subset of the ureilites with mg#s of 75-77. Experiments using the ULM liquid only are saturated with pigeonite, augite, metal and liquid. Twenty-nine percent Fo_{75} olivine was then added to bring the bulk composition into the olivine primary phase volume. The bulk composition of 71% ULM and 29% Fo_{75} olivine is saturated with olivine, orthopyroxene, metal and liquid with mg#s of the solid phases in the 75-76 range. The predominant pyroxene is orthopyroxene rather than pigeonite. In order to raise the Wo content of the experimental pyroxene, 5% Cpx with an mg# of 76 was added. The experimental pyroxenes produced by the Cpx added bulk composition (LMC) are pigeonite, with olivine, metal and liquid as additional saturating phases.

The LMC bulk composition produces the correct assemblage with the appropriate mineral chemistry to explore smelting as it applies to the ureilites. Several other key data also support using this bulk composition. Figure 5b displays the pigeonite Wo content of ureilites vs. the estimated temperature as reported in Singletary and Grove (2003). Figure 5a displays the experimental Wo content vs. temperature from this study. The low temperature ureilites and experiments (~1150-1220°C) contain Wo 8-12 pigeonite. The Wo content in both ureilites and experiments decrease at higher temperatures to ~4 at 1300°C. The equations for the line of best fit through both sets of data are similar as well. Additionally, the pigeonite Wo content vs. Olivine Fo content are similar between the LMC experiments and ureilites as shown in Figure 13, with low olivine Fo contents correlating to high pigeonite Wo contents. Based on the similarity of the experimental data to the ureilite data, the correct phase assemblage and mineral chemistry, we feel the LMC experiments represent a close approximation to the ureilite system. Consequently, these experiments are used to investigate the petrogenesis of the ureilites through smelting of a low Fo (75-77) residue.

If smelting is occurring then several predictions can be made about mineral chemistry and the experiments should display systematic behavior consistent with the smelting reaction. If this is the case, then the experiments can be used to predict the consequences of smelting and then compared to the mineral chemistry variations in the ureilites. Predicted behavior due to smelting should include: 1) isothermal pressure decrease resulting in a rise of mg# of the silicate phases as smelting proceeds due to the sequestration of Fe metal; 2) isobaric temperature decrease resulting in a decrease of mg#, reflecting olivine crystallization.

The twenty experiments shown in Figure 4e display exactly the behavior predicted if the smelting reaction is occurring. Along all isotherms, as pressure decreases, the olivine Fo content and pigeonite mg# rise (with the single exception of the 55 bar experiment at 1200°C). Likewise, along each isobar, the mg# of both phases decreases. This set of smelted experiments can now be used to apply the smelting model to ureilites and investigate smelting as a viable model for ureilite petrogenesis.

The results of the smelting reaction coefficient calibration indicate that the smelting reaction is proceeding as hypothesized, with carbon, olivine and liquid being consumed and carbon monoxide, pigeonite and metal being generated. There exists scatter in the data, but there is a general trend of increasing metal production with higher temperatures. This is reflected in Figure 14 that plots olivine Fo content against temperature.

The results of the model smelting runs indicate that if the ureilite source material contained Fo_{75} olivine, the ureilites are best modeled by progressive heating of an olivine rich residue, approximated in our model by a composition of 7%ULM:91%Fo_{75}:2%Cpx. The residue trend generated by fractional smelting indicates that the initial residue must be olivine rich to reproduce the bulk composition variations in ureilites as expressed in the Ol-Cpx-Qtz ternary diagram. Once the temperature has risen to sufficiently high values (in excess of 1260°C) the calibrated reaction coefficients become such that smelting can produce the high mg# (>90) ureilites and the residue compositions then migrate back through the bulk compositions as shown in Figure 7. This is in agreement with Singletary and Grove (2003) that found the high mg# ureilite pigeonite record temperatures of 1280°C and higher.

The behavior of the Ca/Al ratios and Cr_2O_3 contents of the model residue are also indicative of progressive heating of the source material. At low temperatures (<1260°C) the model runs indicate that smelting can raise the Ca/Al ratio and Cr_2O_3 content of the residue. As temperature increases and the amount of pyroxene added to the residue is decreased and outpaced by metal, the change in Ca/Al ratio decreases and approaches a constant value. The same behavior is observed in the Cr_2O_3 data as well. The ureilite data reported in Figures 8 and 10 are consistent with this idea. While the exact Ca/Al values do not match, we caution that the full extent of compositional space has yet to be explored (more Ca/Al rich residues) nor have all phases that maybe participating in the smelting reaction been included and accounted for (i.e. spinel may play a significant role in controlling the Ca/Al ratio and Cr_2O_3 contents).

The correlation of olivine Fo content with $\Delta^{17}O$ in ureilites (Fig. 15) has been interpreted to reflect a radial stratification in the ureilite parent body (Goodrich *et al,* 2003). Why such a gradient should exist is not clear. Based on the data presented here, we put forth an argument for a heterogeneous parent body that experiences diapirism as illustrated in Figure 16.

Heterogeneous incorporation of heat producing elements, predominantly ^{26}Al in the form of CAIs, leads to differential heating of the ureilite parent body. As packages of material begin to heat to temperatures where partial melting can begin, the smelting reaction begins to produce CO gas. Packages that are heated to a greater extent become more buoyant as more gas is added and begin to rise. Additional heat is added as the smelting reaction itself is exothermic, releasing ~121 kJ of energy at 1200°C and 124 kJ at 1300°C for each mole of CO gas produced.

The drop in pressure experienced by the ascending material, coupled with the increased temperatures drives the smelting reaction to produce ureilites with high mg# silicates. A process such as this would preserve the primitive isotopic signature of the ureilites and explain the correlation of high mg# to $\Delta^{17}O$ without the need for a radial gradient in oxygen isotopes. This model also explains the inverse depth-temperature correlation reported by Singletary and Grove (2003). The smelting process also has the ability to enrich the Ca/Al ratios and Cr_2O_3 contents of the residue as displayed by the modeled residue compositions.

Conclusions

Petrologic modeling, experimental results and petrographic evidence support smelting as a viable process to invoke in ureilite petrogenesis. Smelting must begin with an olivine-rich source at low temperatures (~1200°C) and occur over a restricted temperature range above 1200°C and below 1300°C. The experimental assemblages indicate that ureilites with low mg#s (75-77) are residues of partial melting of a source that previously contained augite and possibly plagioclase. If plagioclase was present, it is exhausted during earlier fractional smelting and as partial melting continues at low pressure augite is also removed from the source. As fractional smelting continues, temperature increases, carbon is consumed by the smelting reaction and CO gas is produced. Gas production decreases the density of a package of material which then migrates to shallower depths, driving the smelting reaction further and producing higher mg# residues that correlate to ureilites with mg#s greater than 90. This is supported by the assemblages from experiments performed with the no Cpx added bulk compositions and experiments at low

pressures. The correlation of mg# to $\Delta^{17}O$ can also be explained by diapirism of CAI rich packages of material, negating the need for a UPB with a radial stratification of oxygen isotopes. The behavior of the model residue Ca/Al ratios and bulk Cr_2O_3 contents indicates that progressive heating of the ureilite source material may also explain the relations of Ca/Al ratio and Cr_2O_3 to temperature.

References

Armstrong J.T. (1995) Citzaf - a package of correction programs for the quantitative electron microbeam x-ray-analysis of thick polished materials, thin-films, and particles. *Microbeam Analysis* **4**, 177-200.

Berkely J.L., Taylor G.J., Keil K., Harlow G.E. and Prinz M. (1980) The nature and origin of ureilites. *Geochim. Cosmochim. Acta* **44,** 1579-1597.

Berkely J.L. and Jones J.H. (1982) Primary igneous carbon in ureilites: Petrological implications. Proceedings, 13th Lunar and Planetary Science Conference. *J. Geophy. Res.* **87**, A353-A364.

Bryan W.B., Finger L.W. and Chayes F. (1969) Estimating proportions in petrographic mixing equations by least squares approximation. *Science* **163**, 926-927.

Boynton W. V., Starzyk P. M. and Schmitt R. A. (1976) Chemical evidence for genesis of ureilites, achondrite chassigny and nakhlites. *Geochim. Cosmochim. Acta* **40**, 1439-1447.

Clayton R.N. AND Mayeda T.K. (1988) Formation of ureilites by nebular processes. *Geochim. Cosmochim. Acta* **52**, 1313-1318.

Clayton R.N. AND Mayeda T.K. (1996) Oxygen isotope studies of achondrites. *Geochim. Cosmochim. Acta* **60**, 1999-2017.

Goodrich C.A. (1992) Ureilites: A critical-review. *Meteoritics* **27**, 327-352.

Goodrich C.A. and Berkley J.L. (1986) Primary magmatic carbon in ureilites: Evidence from cohenite-bearing metallic spherules. *Geochim. Cosmochim. Acta* **50**, 681-691.

Goodrich C.A., Jones J.H. and Berkley J.L. (1987) Origin and evolution of the ureilite parent magma: Multi-stage igneous activity on a large parent body. *Geochim. Cosmochim. Acta* **51**, 2255-2273.

Goodrich C.A., Fioretti A.M., Molin G. and Tribaudino M. (1999) Primary trapped melt inclusions in olivine in a ureilite – I. *Description. Lunar Planet. Sci.* **30**, abtr. 1026.

Goodrich C.A., Fioretti A.M., Tribaudino M. and Molin G. (2001) Primary trapped melt inclusions in olivine in the olivine-augite-orthopyroxene ureilite Hughes 009. *Geochim. Cosmochim Acta* **65**, 621-652.

Goodrich C.A., Krot A.N., Scott E.R.D., Taylor G.J., Fioretti A.M. and Keil K. (2002) Formation and evolution of the ureilite parent body and its offspring. In *Lunar and Planetary Science XXXIII,* Abstract #1379, Lunar and Planetary Institute, Houston (CD-ROM).

Grove T.L. and Bence A.E. (1977) Experimental study of pyroxene-liquid interaction in quartz-normative basalt 15597. *Proc. Lunar Sci. Conf.* **8th,** 1549-1579.

Grove T.L., Elkins-Tanton L.T., Parman S.W., Chatterjee N., Muenter O. and Gaetani G.A. (2003) Fractional crystallization and mantle-melting controls on calc-alkaline differentiation trends. *Contrib. to Mineral. Petrol.* **145,** 515-533.

Mittlefehldt D.W., McCoy T.J., Goodrich C.A. and Kracher A. (1998) Non-chondritic meteorites from asteroidal bodies. In *Planetary Materials* (ed. J. Papike), **36.**

Kushiro I. (1972) Determination of liquidus relations in synthetic silicate systems with electron probe analysis: the system forsterite-diopside-silica at 1 atmosphere. *Am. Mineral.* **57,** 1260-1271.

Rubin A.E. (1988) Formation of ureilites by impact-melting of carbonaceous chondritic material. *Meteoritics* **23,** 333-337.

Scott E.R.D., Taylor G.J. and Keil K. (1993) Origin of ureilite meteorites and implications for planetary accretion. *Geophys. Res. Lett.* **20,** 415-418.

Sinha S.K., Sack R.O. and Lipshutz M.E. (1997) Ureilite meteorites: Equilibration temperatures and smelting reactions. *Geochim. Cosmochim. Acta* **61,** 4235-4242.

Singletary S.J. and Grove T.L. (2003) Early petrologic processes on the ureilite parent body. *Met. & Planet. Sci.* **38,** 95-108.

Takeda H. (1987) Mineralogy of Antarctic ureilites and a working hypothesis for their origin and evolution. *Earth Planet. Sci. Lett.* **81,** 358-370.

Takeda H., Mori H. and Ogata H. (1989) Mineralogy of augite-bearing ureilites and the origin of their chemical trends. *Meteoritics* **24,** 73-81.

Treiman A. and Berkley J.L. (1994) Igneous petrology of the new ureilites Nova 001 and Nullarbor 010. *Meteoritics* **29,** 843-848.

Vdovykin G.P. (1970) Ureilites. *Space Sci. Rev.* **10,** 483-510.

Walker D. and Agee C. B. (1988) Ureilite compaction. *Meteoritics* **23,** 81-91.

Walker D. and Grove T. (1993) Ureilite smelting. *Meteoritics* **28,** 629-636.

Warren P.H. and Kallemeyn G.W. (1992) Explosive volcanism and the graphite oxygen fugacity buffer on the parent asteroid(s) of the ureilite meteorites. *Icarus* **100**, 110-126.

Wasson J.T., Chou C.L., Bild R.W. and Baedecker P.A. (1976) Classification of and elemental fractionation among Ureilites. *Geochim. Cosmochim. Acta* **40**, 1449-1458.

Weber H.W., Begemann F. and Hintenberger H. (1976) Primordial gases in graphite-diamond-kamacite inclusions from the Havero ureilite. *Earth Planet. Sci. Lett.* **29**, 81-90.

Figure Captions

Figure 1. $\delta^{17}O$ vs $\delta^{18}O$ of Martian, HED, Terrestrial, Lunar and Ureilite samples. Ureilites line along a line of slope 1. The terrestrial fraction line has slope 0.52 and is characteristic of samples that have under gone extensive igneous processing. The martian samples also fall along a line of slope 0.52 but displaced from the terrestrial fractionation line. Data from Clayton and Mayeda (1996).

Figure 2. Backscattered Electron Images of experimental run products. A) BSE image of an entire experimental charge. Black areas within the charge are bubbles, presumably filled with CO gas during the experiment. B) BSE image showing a close up of the crystalline run products and liquid. This experiment (LMC-3) is saturated with olivine, pigeonite, metal and liquid.

Figure 3. Olivine-Clinopyroxene-Quartz ternary diagrams. Phase boundaries are from Kushiro (1972) and are shown for reference. Run products for each bulk composition used are displayed, see text for discussion. A) 79Pu:21Fo_{83} bulk composition. B) 79Pu:21Fo_{75} bulk composition. C) ULM. D) ULM + Fo_{75}. E) ULM + Fo_{75} + Cpx.

Figure 4. Pressure-Temperature grids for all bulk compositions used in this study. The bulk composition plotted is given in the upper right corner for each grid. Symbols for each experiments indicate saturating phases. Liquid is present in all experiments in addition to the crystalline phases. The phases present are represented by solid fill. Numbers by each symbol report the mg# of the phases.

Figure 5. Pyroxene Wo content vs temperature. a) experimental pyroxenes (see Table 2). b) ureilite pyroxenes (data from Singletary and Grove (2003) and references therein).

Figure 6. Experimental pyroxene compositions vs. run temperature (see Table 2). a) mol % Al_2O_3. b) mol % TiO_2. c) mol% Cr_2O_3.

Figure 7. Model residue compositions plotted in Olivine-Clinopyroxene-Quartz ternary space. Each diagram represents a portion of the Ol-Cpx-Qtz ternary as depicted in the inset. Filled circles are ureilite bulk compositions calculated from the modal proportions and phase analyses of Singletary and Grove (2003). Arrows display the predicted residue behavior during smelting at the indicated temperature. The starting composition is at the olivine rich end and smelting drives the residue towards pyroxene rich compositions. The exception is the 1280°C trend which moves residue compositions away from the olivine-pyroxene reaction boundary.

Figure 8. Model olivine Fo content vs. model step. Each step represents 2% fractional smelting as described in the text. Each trend represents isothermal decompression of the model residue composition.

Figure 9. Ureilite pyroxene Ca/Al (molar) ratios vs. estimated equilibrium temperatures. Data from Singletary and Grove (2003).

Figure 10. Model bulk residue Ca/Al (molar) values vs. model step (see Figure 8 for model).

Figure 11. Ureilite bulk Cr_2O_3 wt% values vs estimated equilibrium temperature (Singletary and Grove, 2003).

Figure 12. Model bulk residue Cr_2O_3 wt% values vs. model step (see figure 8 for model).

Figure 13. Pyroxene Wo content vs. Olivine Fo content. a) experimentally produced pyroxene Wo contents vs. co-existing olivine Fo content (see Table 2). b) ureilite pyroxene Wo content vs. co-existing olivine Fo content. Data from Singletary and Grove (2003).

Figure 14. Experiment temperature vs. olivine Fo content. Data from this study (see Table 2.)

Figure 15. Ureilite olivine Fo content vs $\Delta^{17}O$. Data from Singletary and Grove (2003) and Clayton and Mayeda (1988; 1996). Ureilites with lower $\Delta^{17}O$ values have higher olivine Fo contents, indicating an advanced degree of smelting.

Figure 16. Cartoon depicting the cross section of a hypothetical ureilite parent body [UPB]. A) Upper panel represents the UPB after the early stages of accretion before igneous processing begins. Heterogeneous accretion produces a parent body composed of randomly mixed packages of isotopically distinct material. Variable CAI contents lead to differential heat production due to the amounts of ^{26}Al present. B) Lower panel shows the same UPB after igneous processing has begun and the early stages of differentiation of the UPB. Individual packages of material undergo differential heating that leads to variable degrees of smelting and ascent within the UPB. As packages of material reorganize within the UPB, mineral chemistries equilibrate and fabrics are produced.

Figure 1.

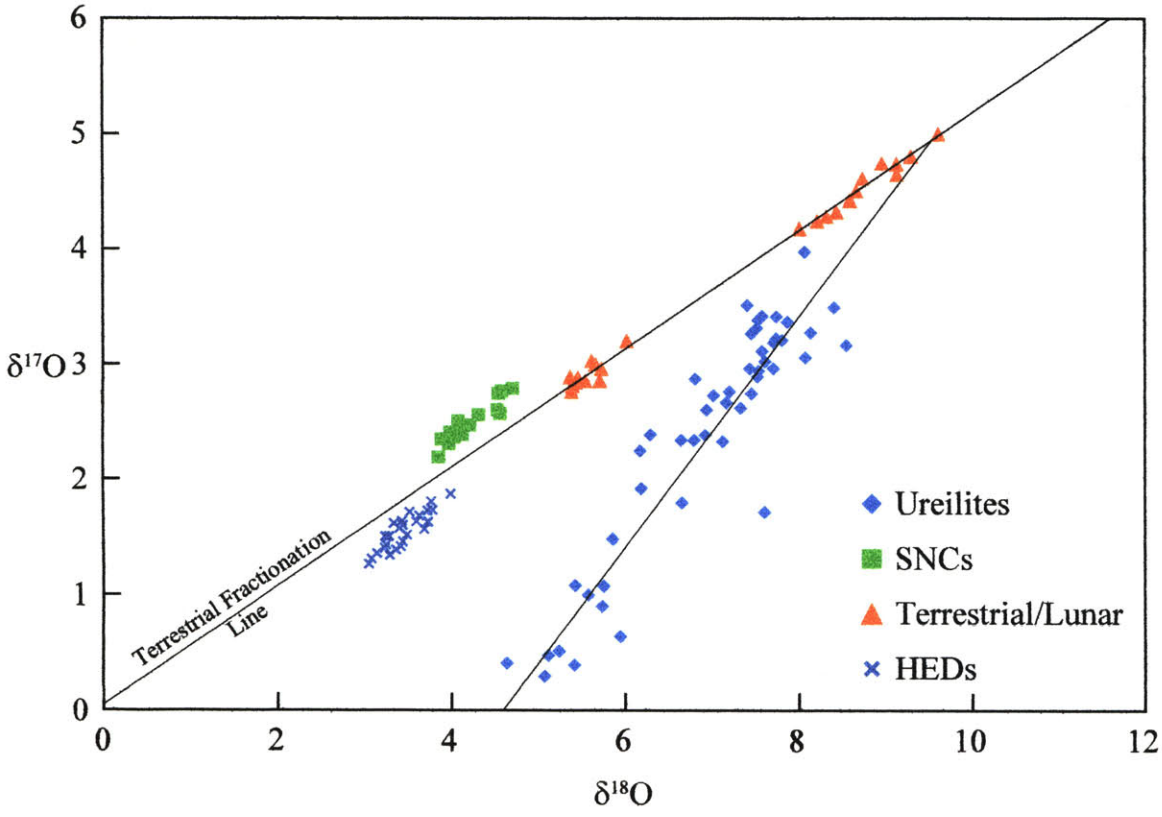
6
5
4
3
2
1
0
$\delta^{17}O$
0
2
4
6
8
10
12
$\delta^{18}O$
Terrestrial Fractionation Line
Ureilites
SNCs
Terrestrial/Lunar
HEDs

Figure 2.

A)

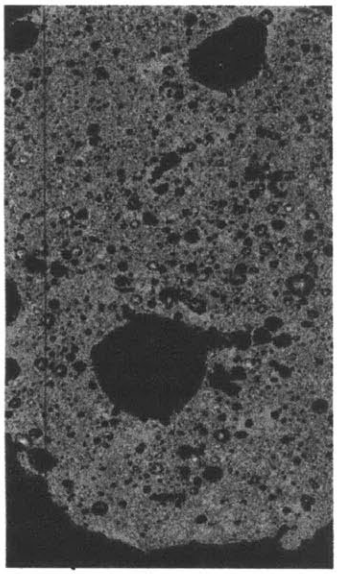

B)

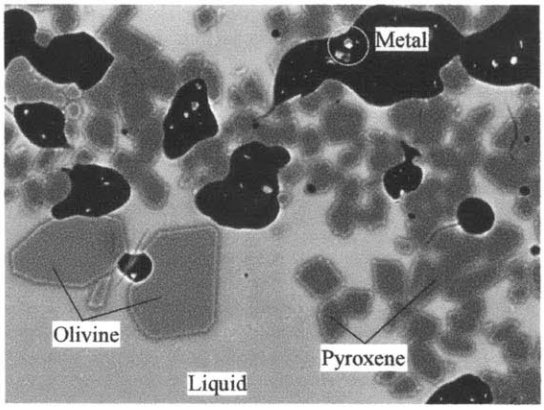

Figure 3.

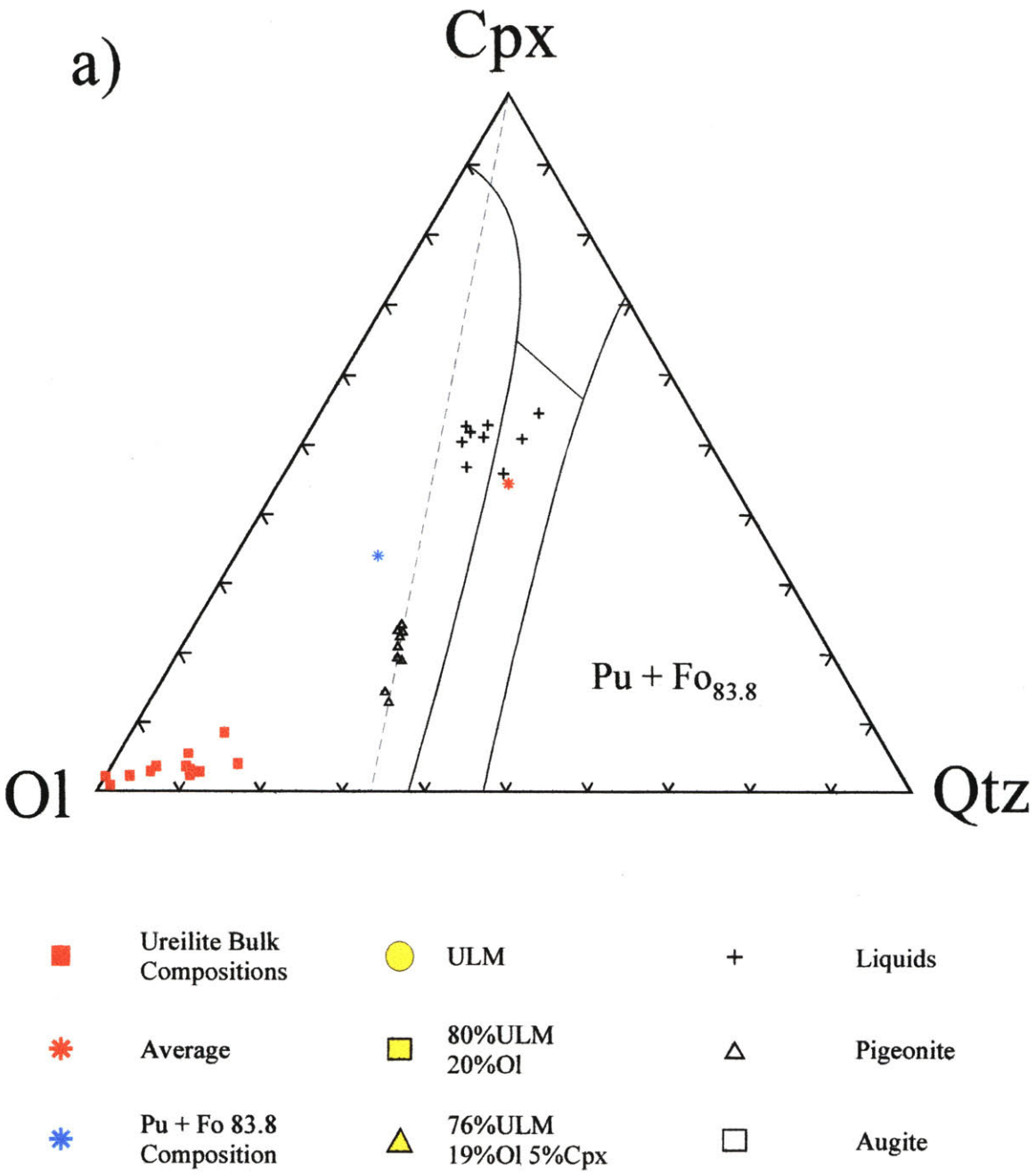
a)
Cpx
Ol
Qtz
Pu + Fo83.8
Ureilite Bulk Compositions
Average
Pu + Fo 83.8 Composition
ULM
80%ULM 20%Ol
76%ULM 19%Ol 5%Cpx
Liquids
Pigeonite
Augite

Figure 3

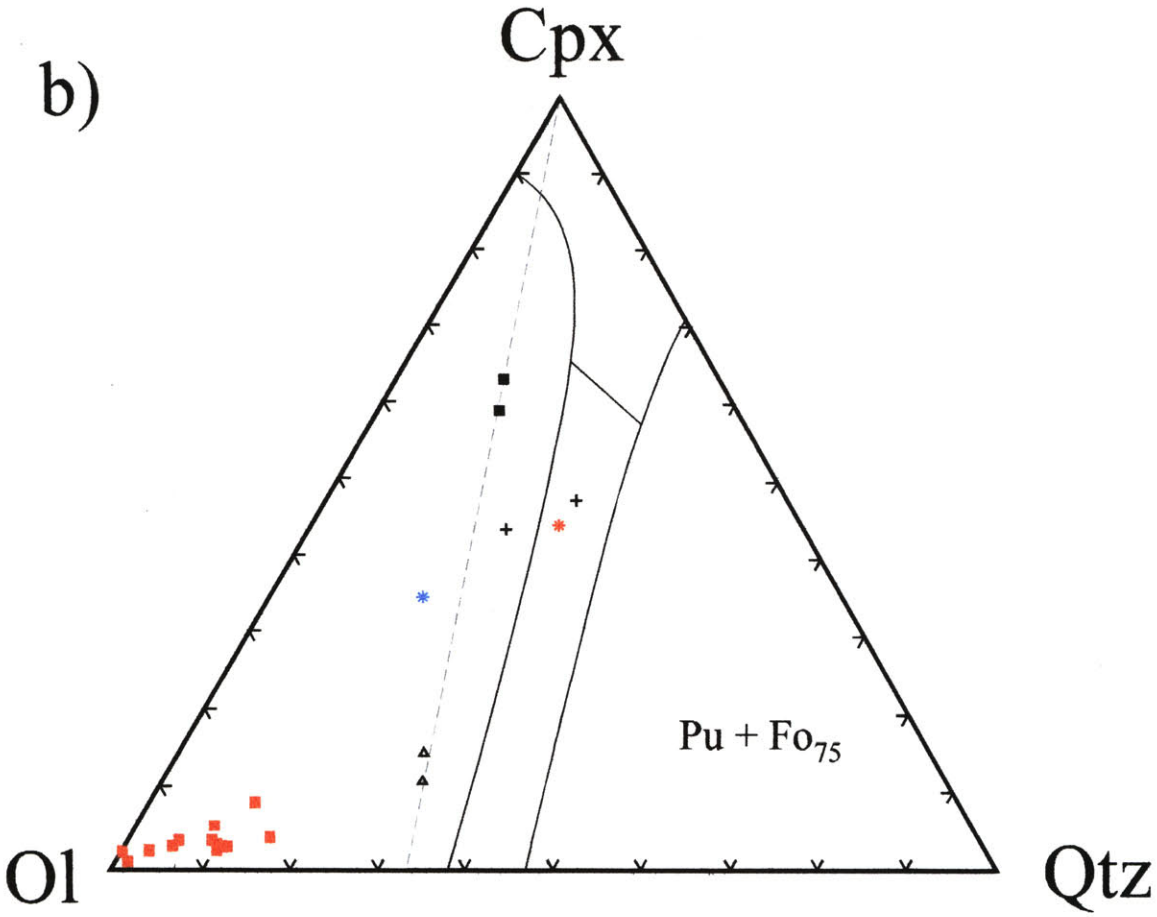

■	Ureilite Bulk Compositions	●	ULM	+	Liquids
✱	Average	□	80%ULM 20%Ol	△	Pigeonite
✱	Pu + Fo 83.8 Composition	△	76%ULM 19%Ol 5%Cpx	□	Augite

Figure 3.

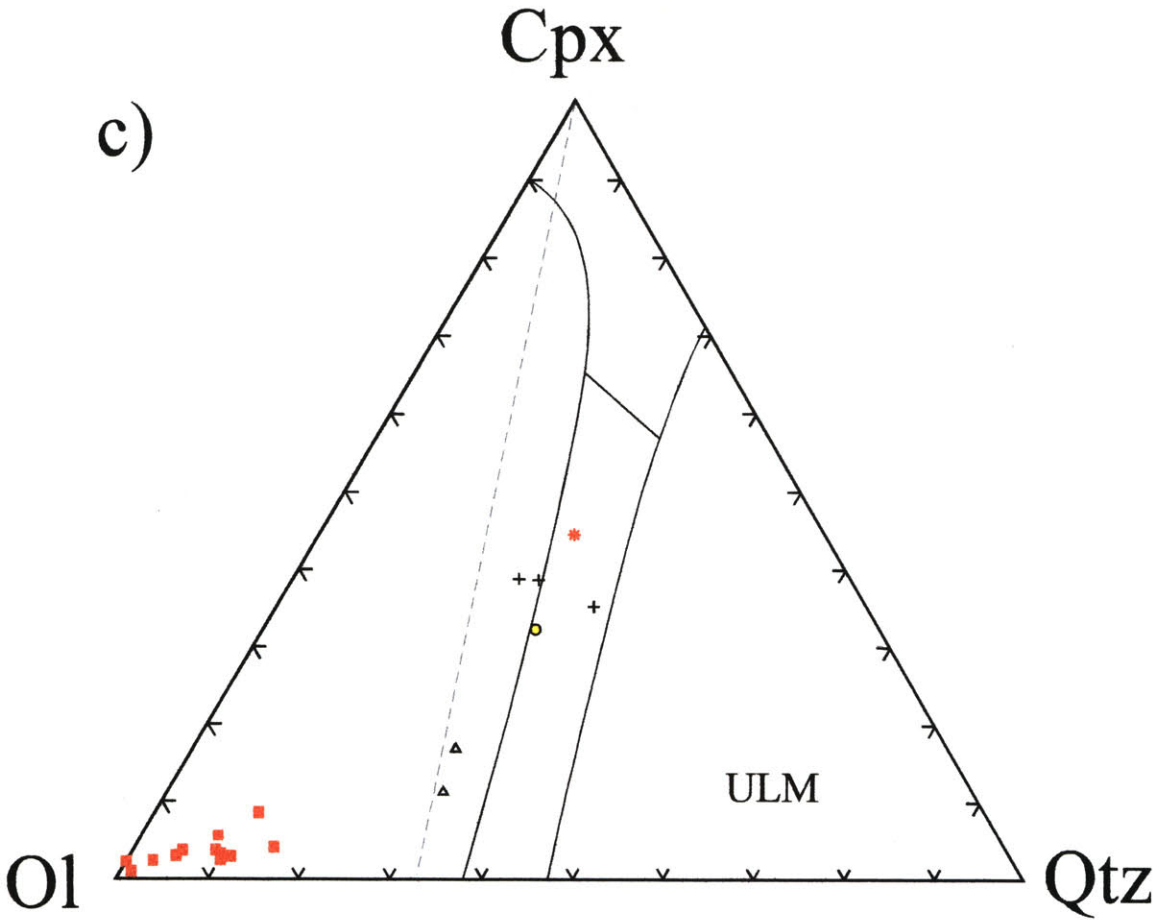

■	Ureilite Bulk Compositions	●	ULM	+	Liquids
✱	Average	□	80%ULM 20%Ol	△	Pigeonite
✱	Pu + Fo 83.8 Composition	△	76%ULM 19%Ol 5%Cpx	□	Aug-ite

Figure 3.

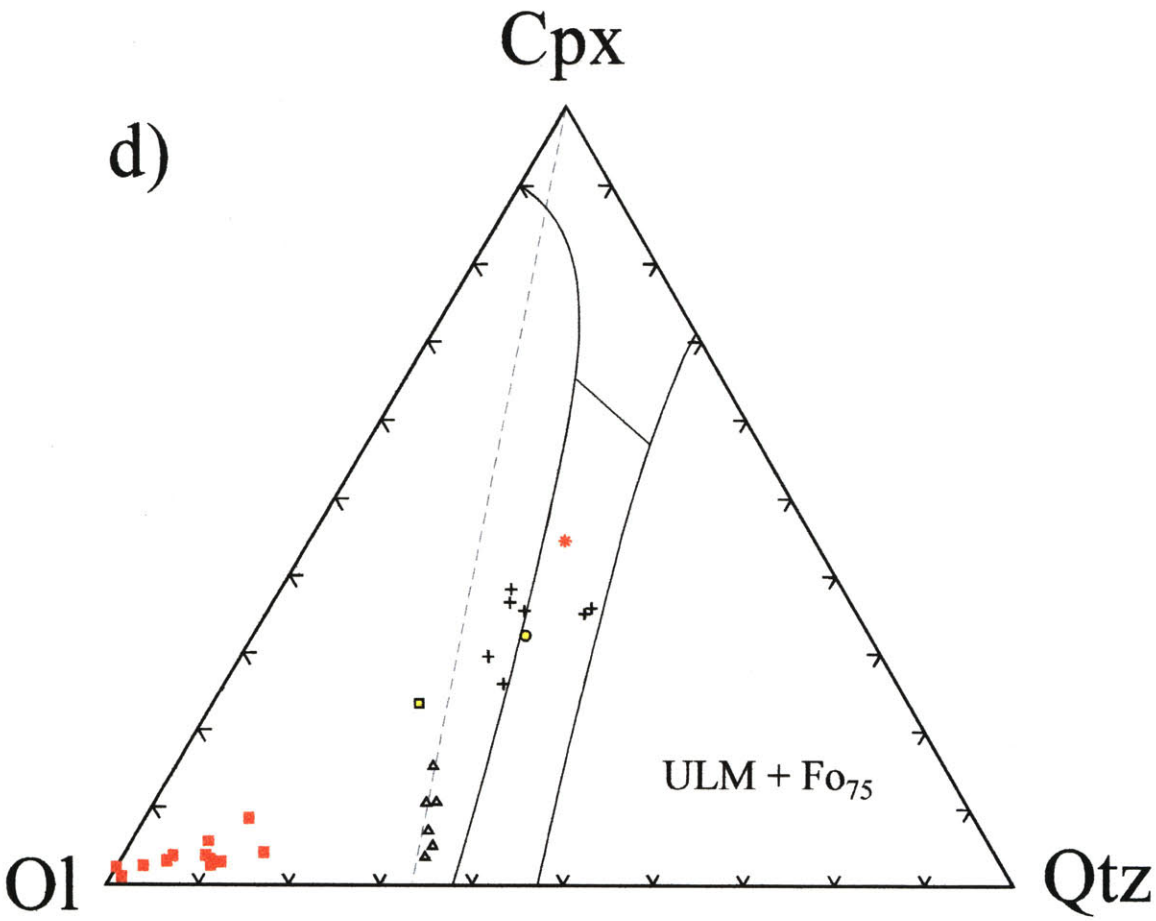

■	Ureilite Bulk Compositions	●	ULM	+	Liquids
✱	Average	□	80%ULM 20%Ol	△	Pigeonite
✱	Pu + Fo 83.8 Composition	△	76%ULM 19%Ol 5%Cpx	□	Augite

Figure 3.

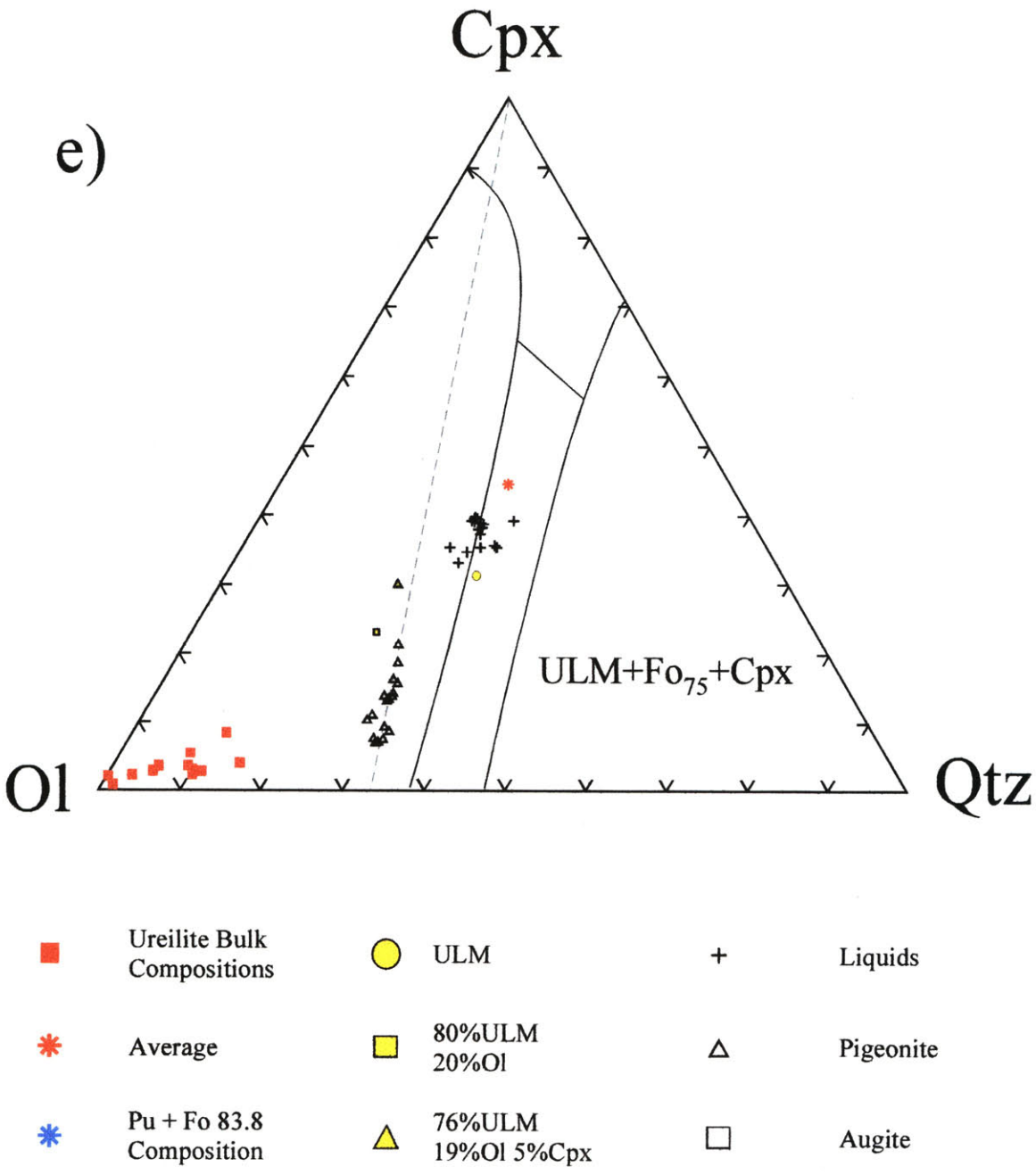
Cpx
e)
ULM+Fo75+Cpx
Ol
Qtz
Ureilite Bulk Compositions
Average
Pu + Fo 83.8 Composition
ULM
80%ULM 20%Ol
76%ULM 19%Ol 5%Cpx
Liquids
Pigeonite
Augite

Figure 4.

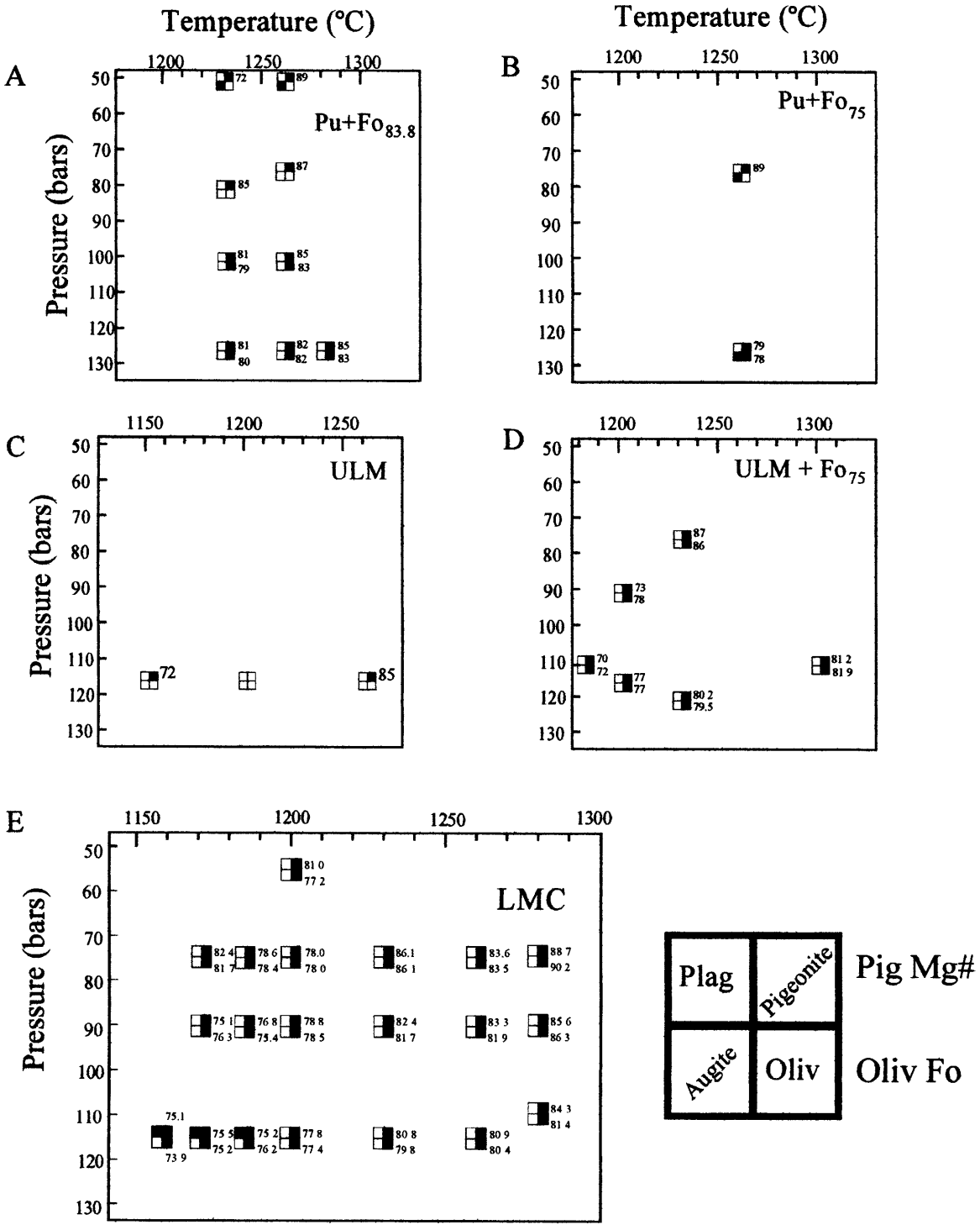
A
Temperature (°C)
Pressure (bars)
Pu+Fo83.8
B
Temperature (°C)
Pu+Fo75
C
ULM
Pressure (bars)
D
ULM + Fo75
E
LMC
Pressure (bars)
Plag
Pigeonite
Augite
Oliv
Pig Mg#
Oliv Fo

Figure 5.

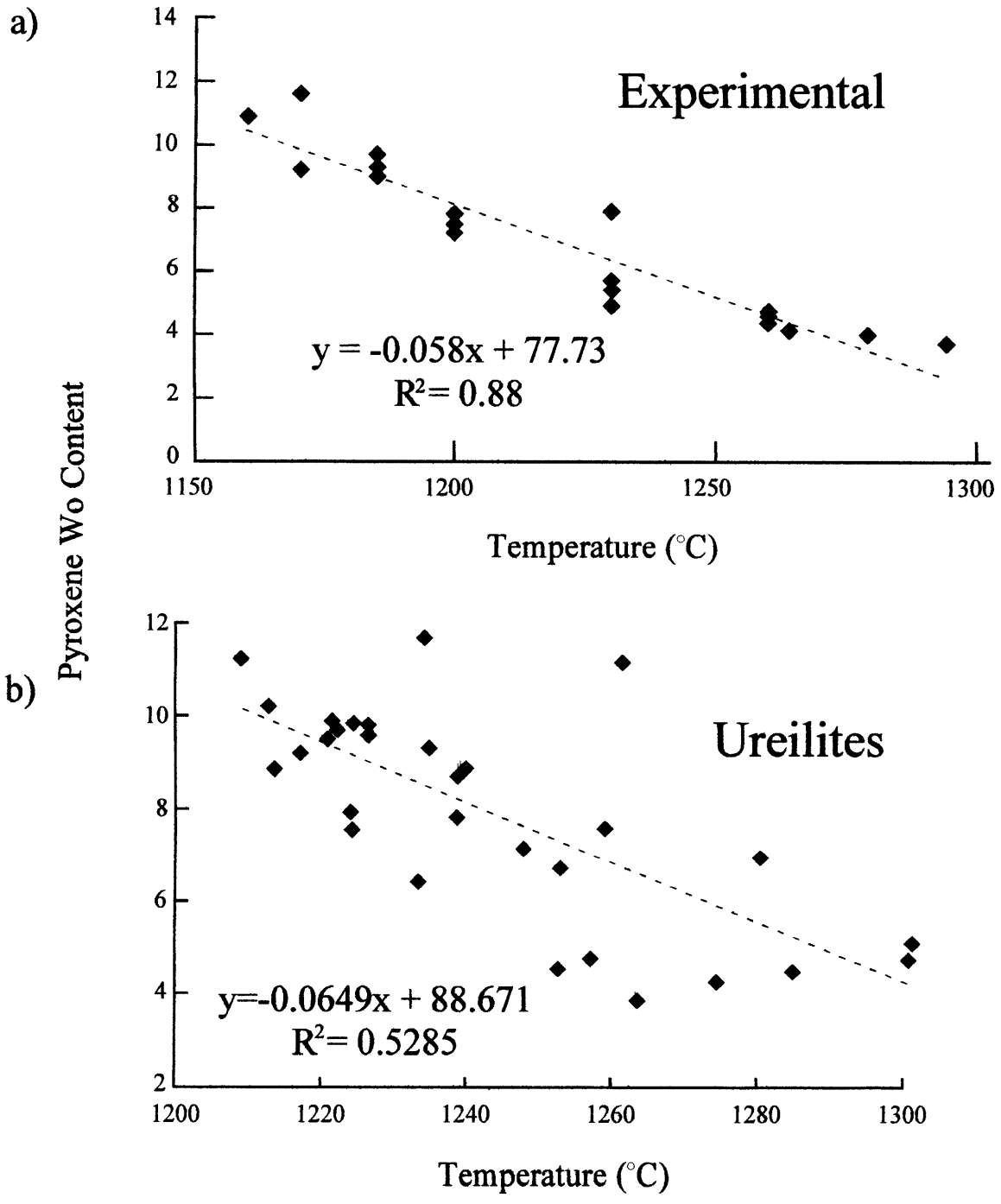
a)
Experimental
y = -0.058x + 77.73
R²= 0.88
Pyroxene Wo Content
Temperature (°C)
b)
Ureilites
y=-0.0649x + 88.671
R²= 0.5285
Temperature (°C)

Figure 6.

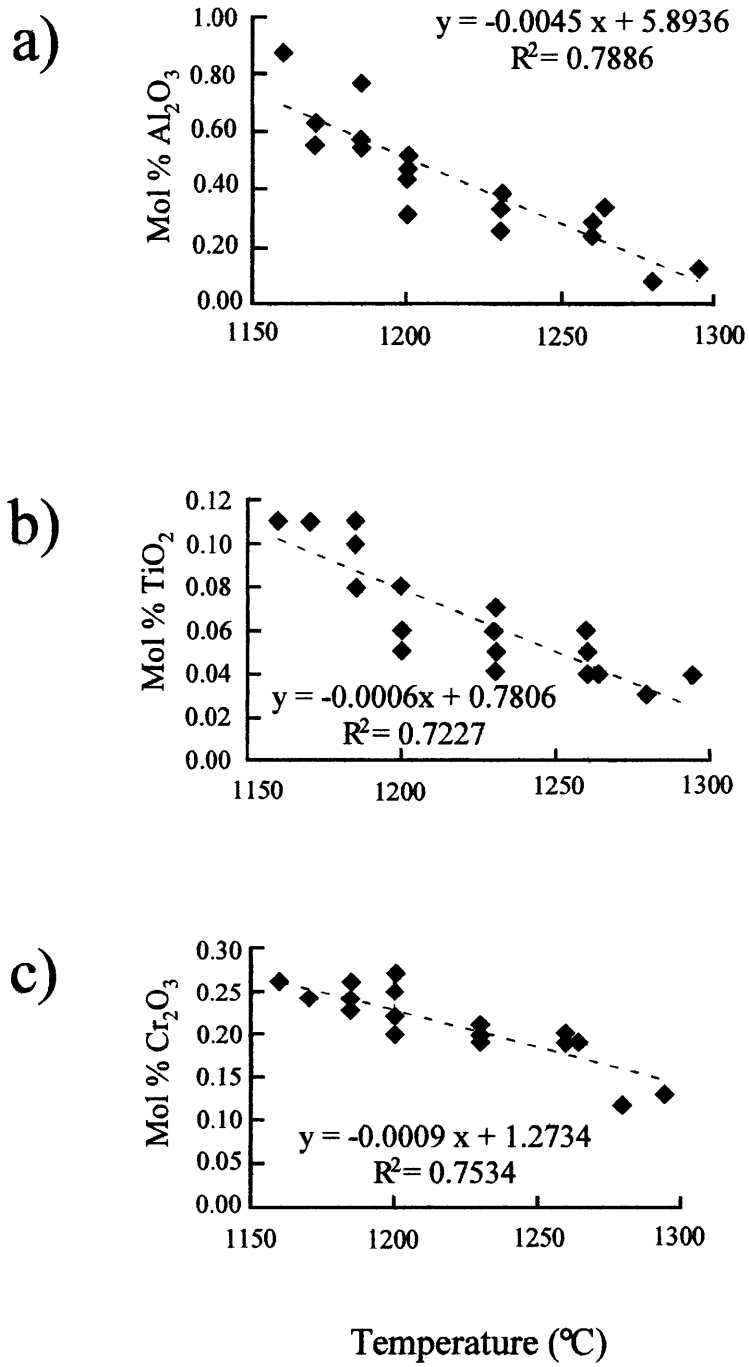
a)
y = -0.0045 x + 5.8936
R2= 0.7886
Mol % Al2O3
1.00
0.80
0.60
0.40
0.20
0.00
1150
1200
1250
1300
b)
Mol % TiO2
0.12
0.10
0.08
0.06
0.04
0.02
0.00
y = -0.0006x + 0.7806
R2= 0.7227
1150
1200
1250
1300
c)
Mol % Cr2O3
0.30
0.25
0.20
0.15
0.10
0.05
0.00
y = -0.0009 x + 1.2734
R2= 0.7534
1150
1200
1250
1300
Temperature (°C)

Figure 7.

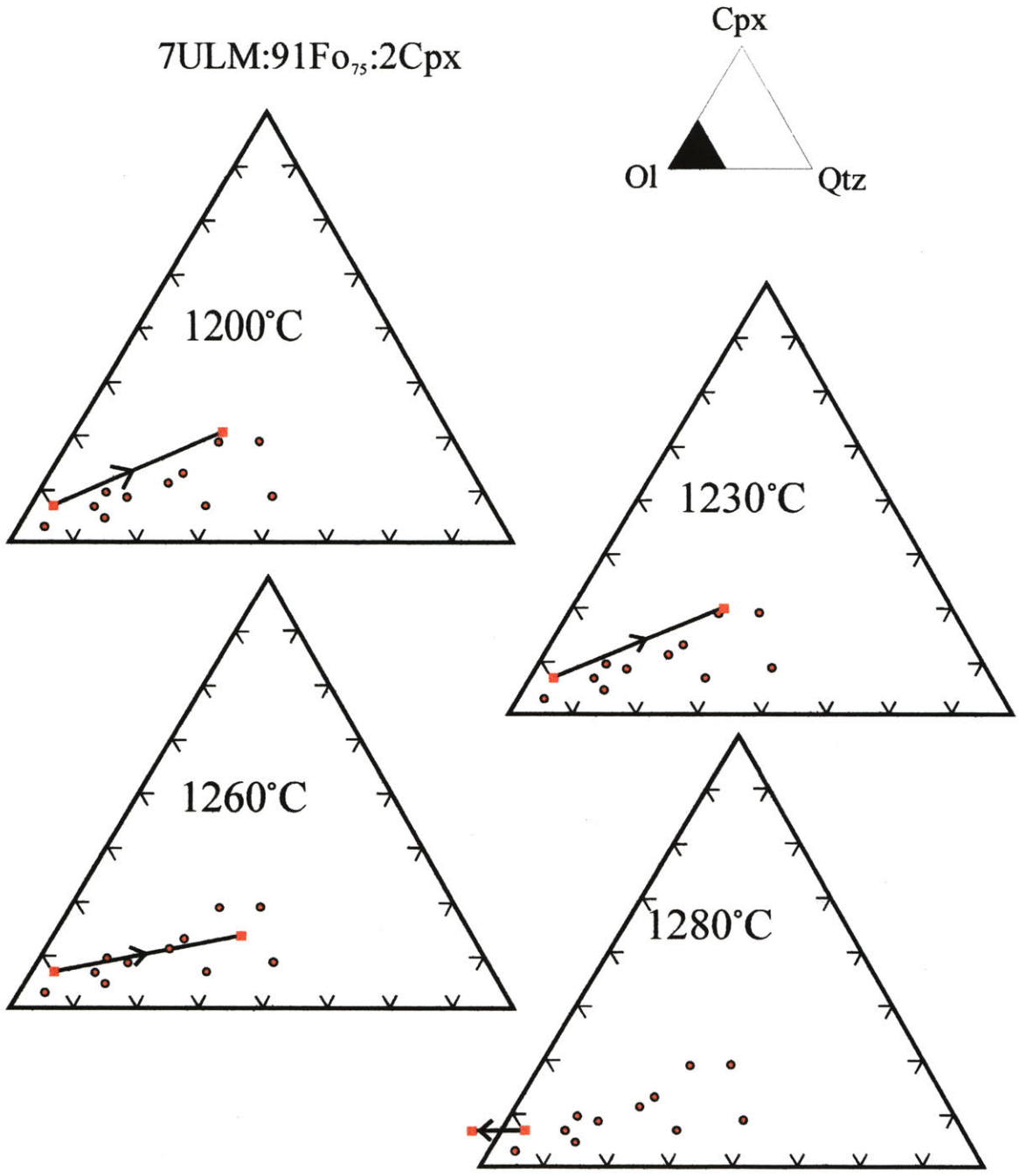

Figure 8.

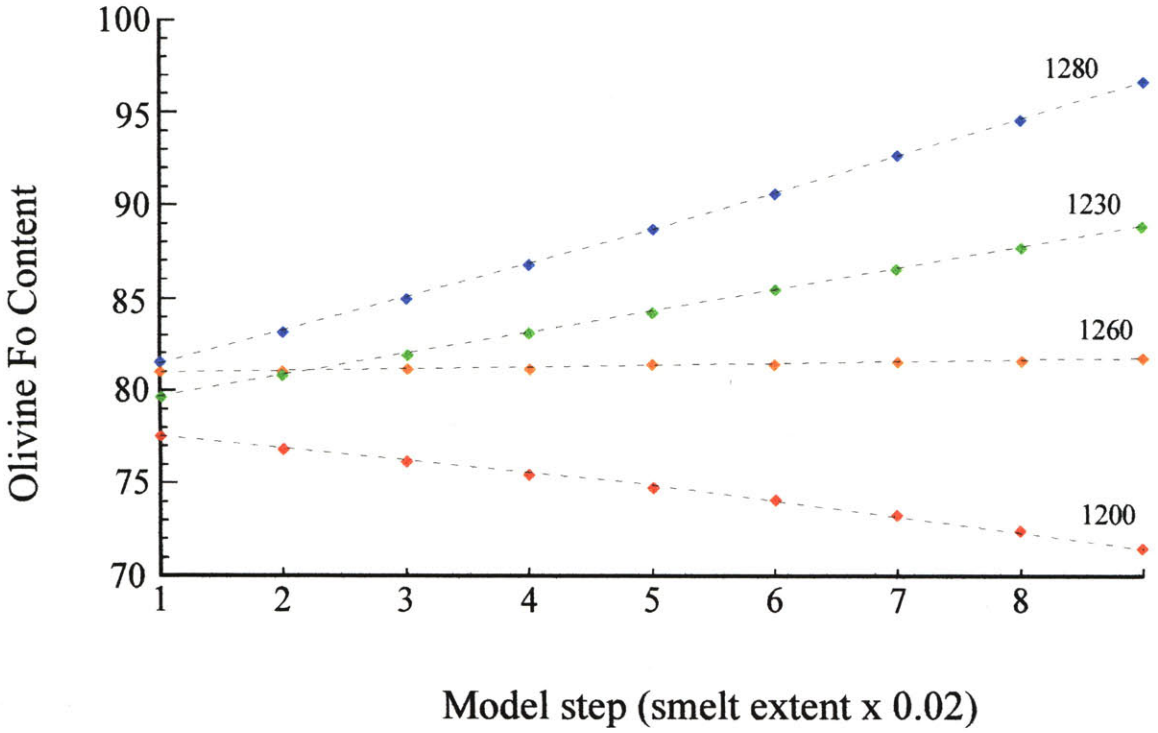
100
95
90
85
80
75
70
Olivine Fo Content
1
2
3
4
5
6
7
8
Model step (smelt extent x 0.02)
1280
1230
1260
1200

Figure 9.

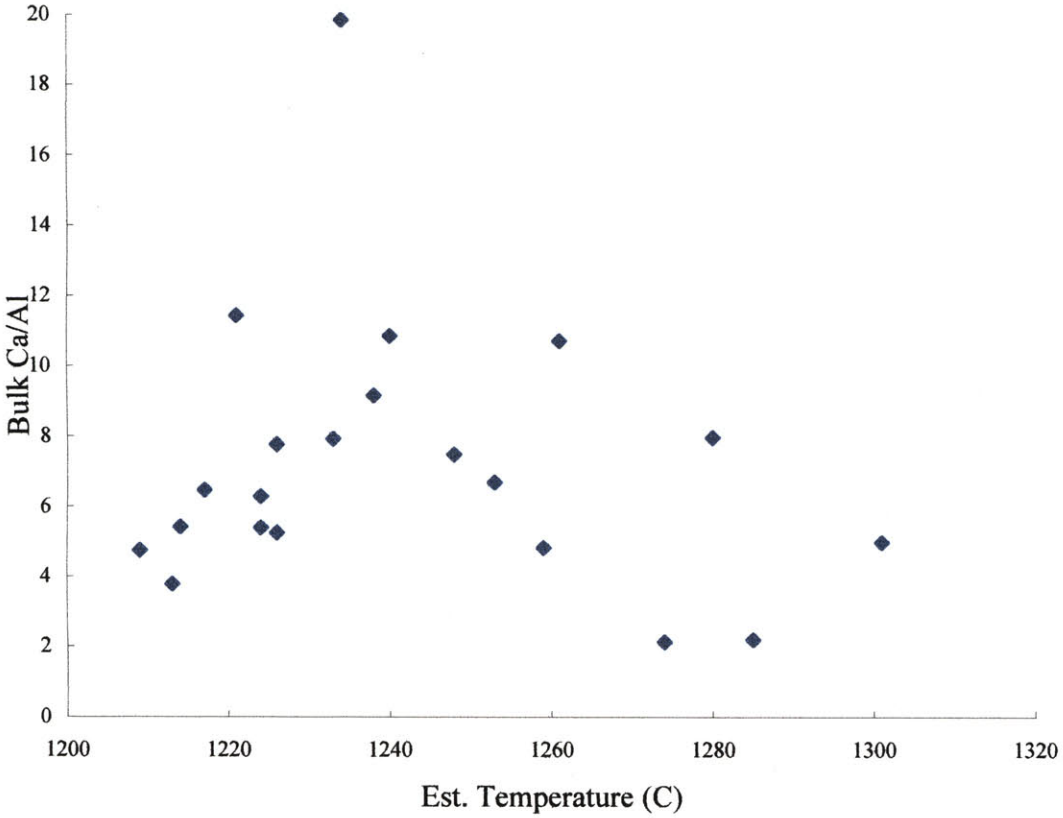
Bulk Ca/Al
20
18
16
14
12
10
8
6
4
2
0
1200
1220
1240
1260
1280
1300
1320
Est. Temperature (C)

Figure 10.

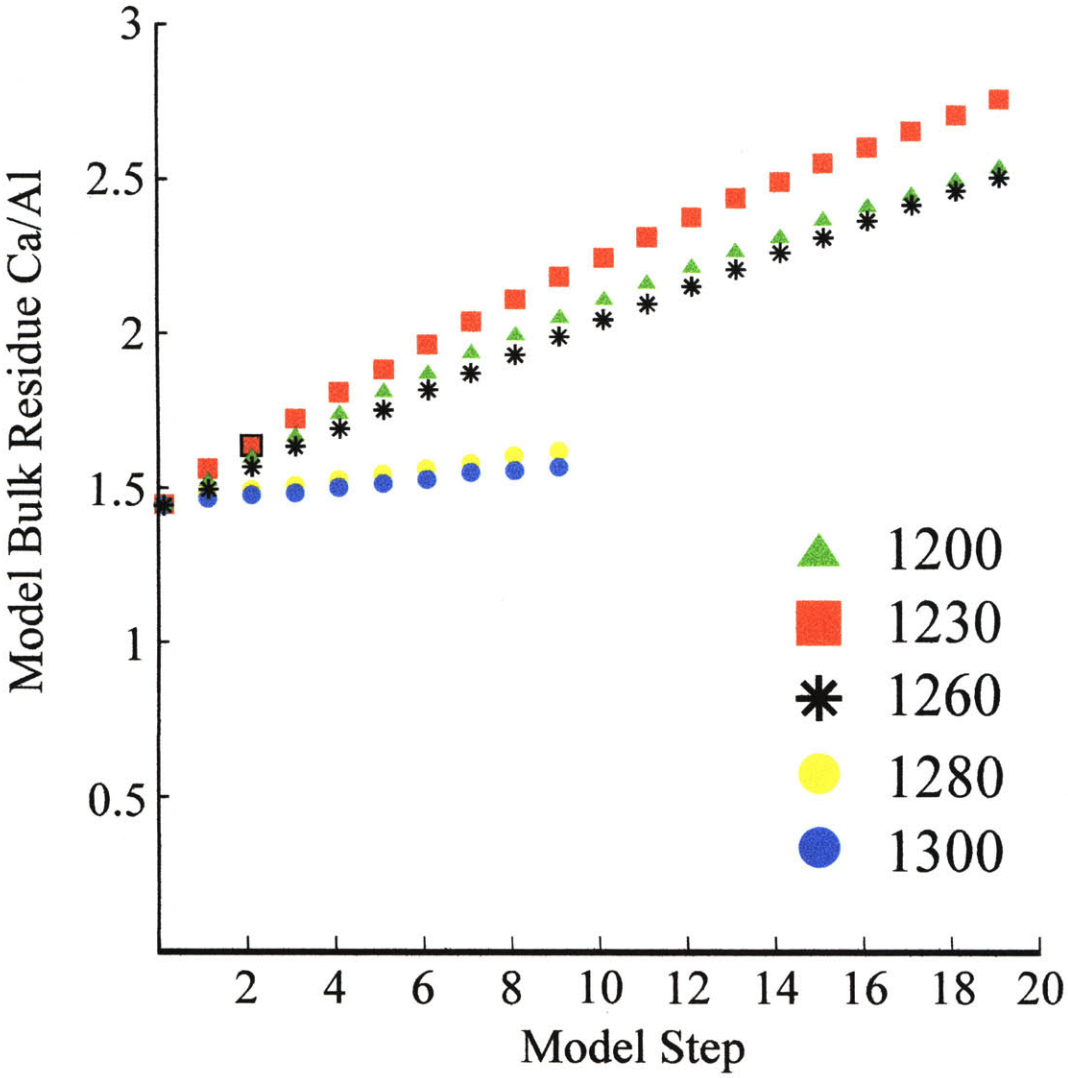
Model Bulk Residue Ca/Al
3
2.5
2
1.5
1
0.5
2
4
6
8
10
12
14
16
18
20
Model Step
1200
1230
1260
1280
1300

Figure 11.

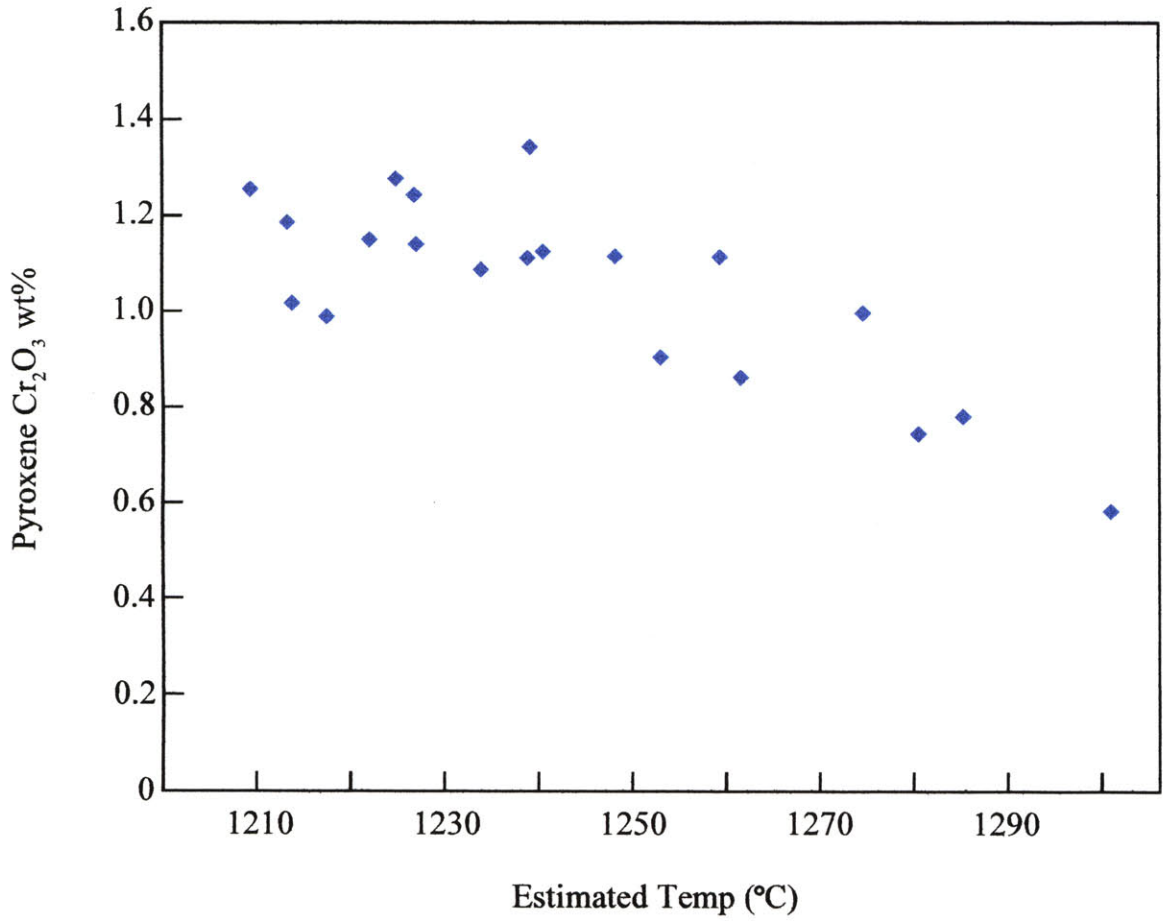
1.6
1.4
1.2
1.0
0.8
0.6
0.4
0.2
0
Pyroxene Cr_2O_3 wt%
1210
1230
1250
1270
1290
Estimated Temp (°C)

Figure 12.

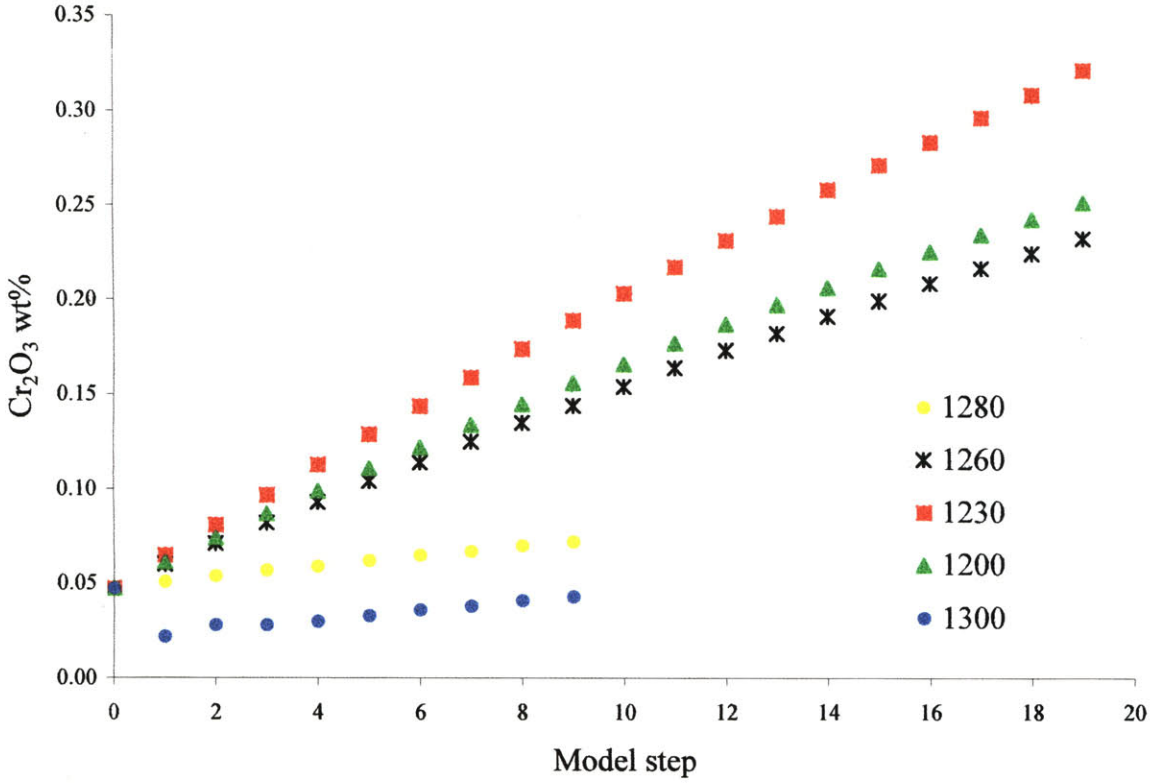
0.35
0.30
0.25
0.20
0.15
0.10
0.05
0.00
Cr_2O_3 wt%
0
2
4
6
8
10
12
14
16
18
20
Model step
1280
1260
1230
1200
1300

Figure 13.

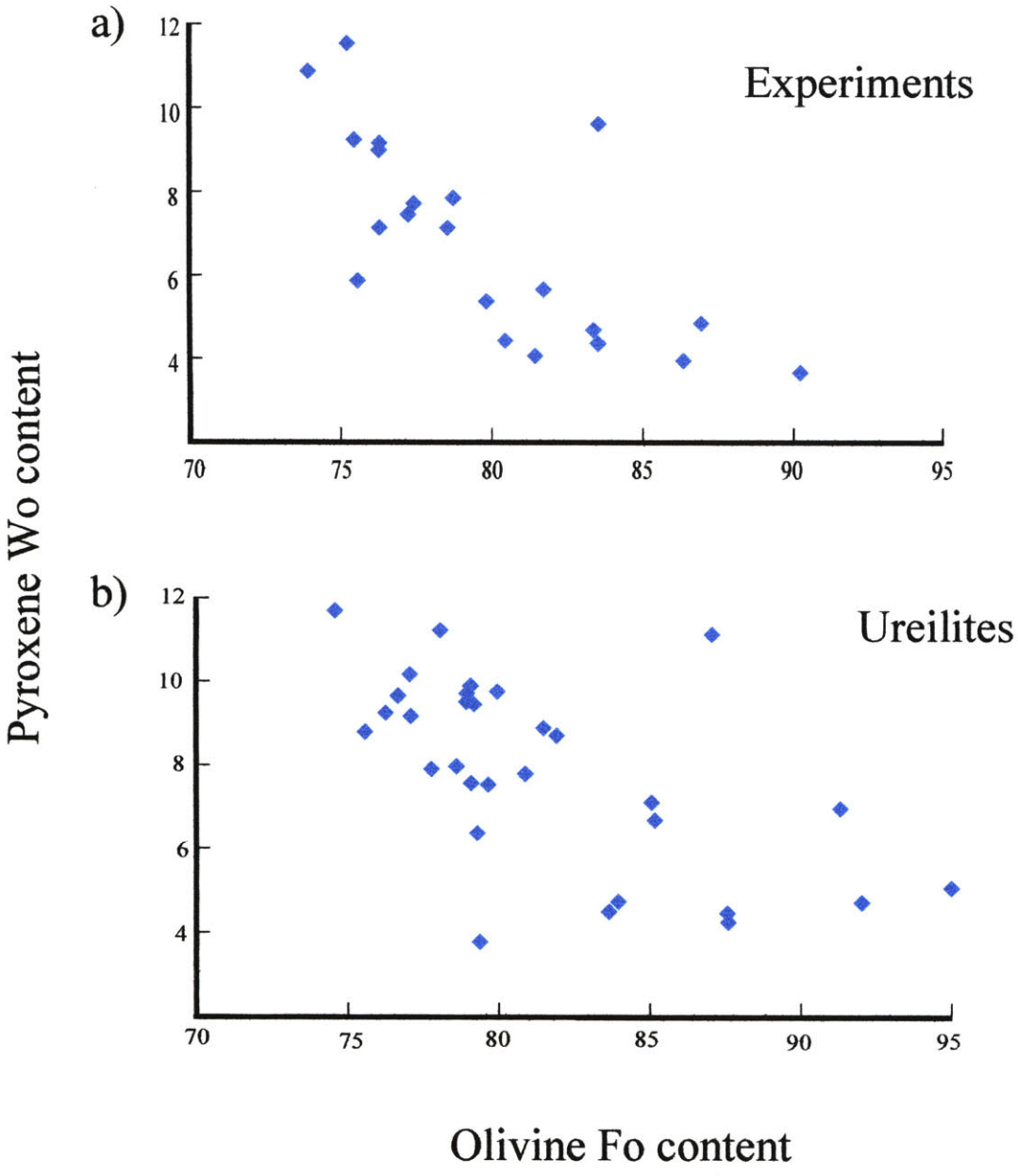
a)
Experiments
b)
Ureilites
Pyroxene Wo content
Olivine Fo content
12
10
8
6
4
70
75
80
85
90
95

Figure 14.

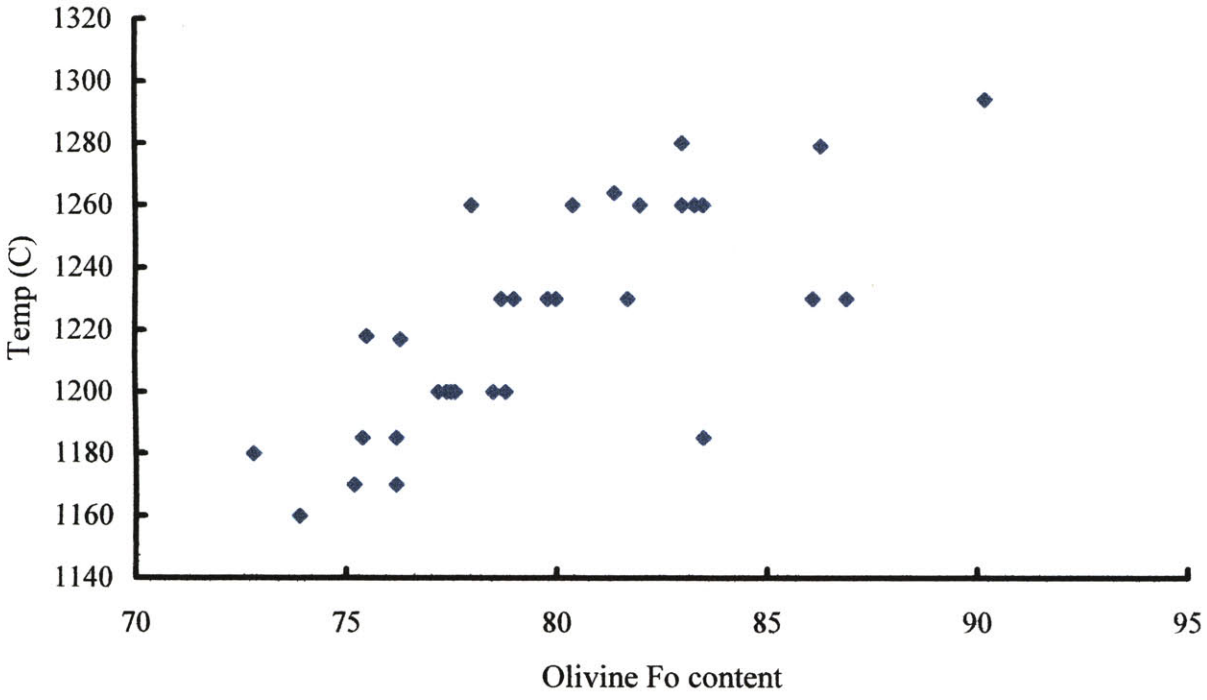
1320
1300
1280
1260
1240
1220
1200
1180
1160
1140
Temp (C)
70
75
80
85
90
95
Olivine Fo content

Figure 15.

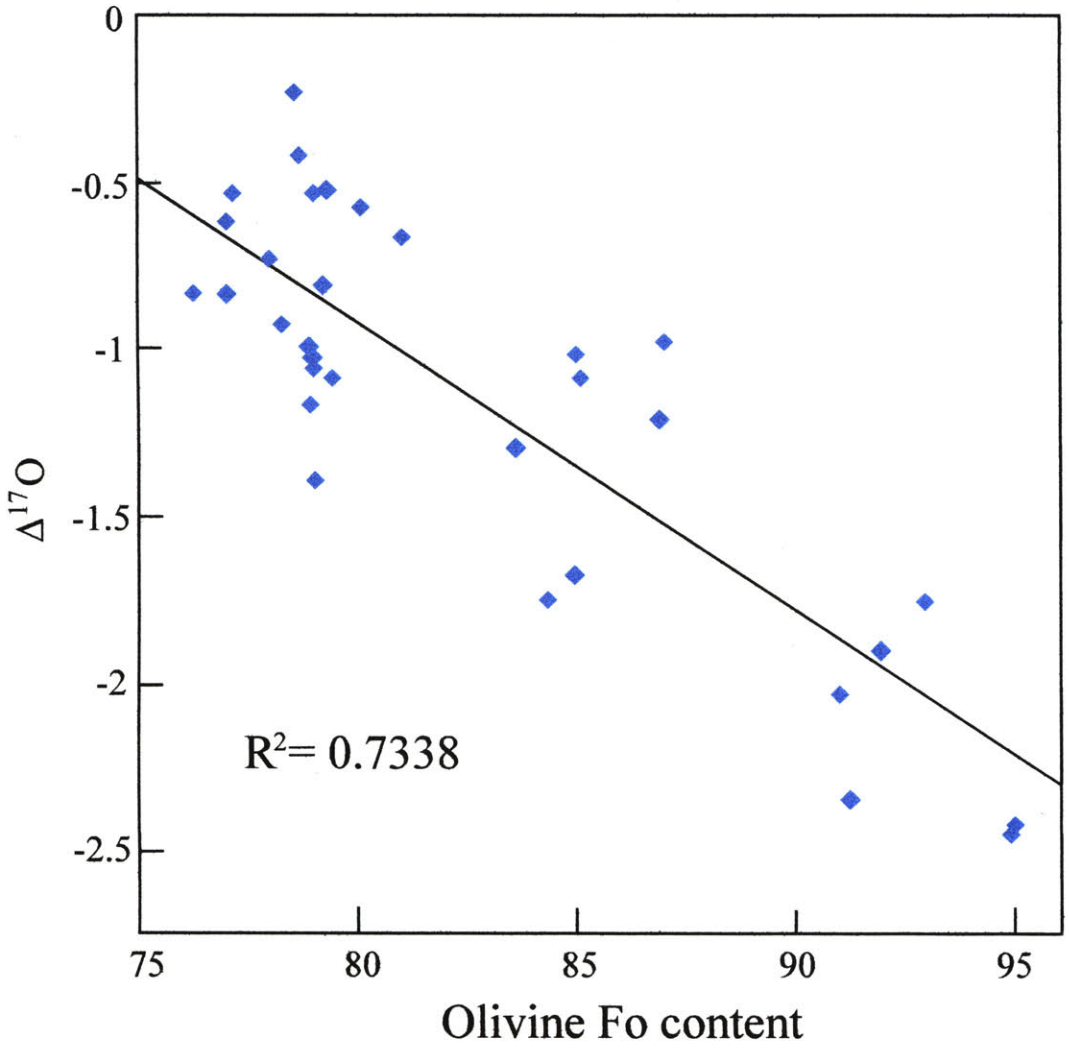
0
-0.5
-1
-1.5
-2
-2.5
$\Delta^{17}O$
R^2= 0.7338
75
80
85
90
95
Olivine Fo content

Figure 16.

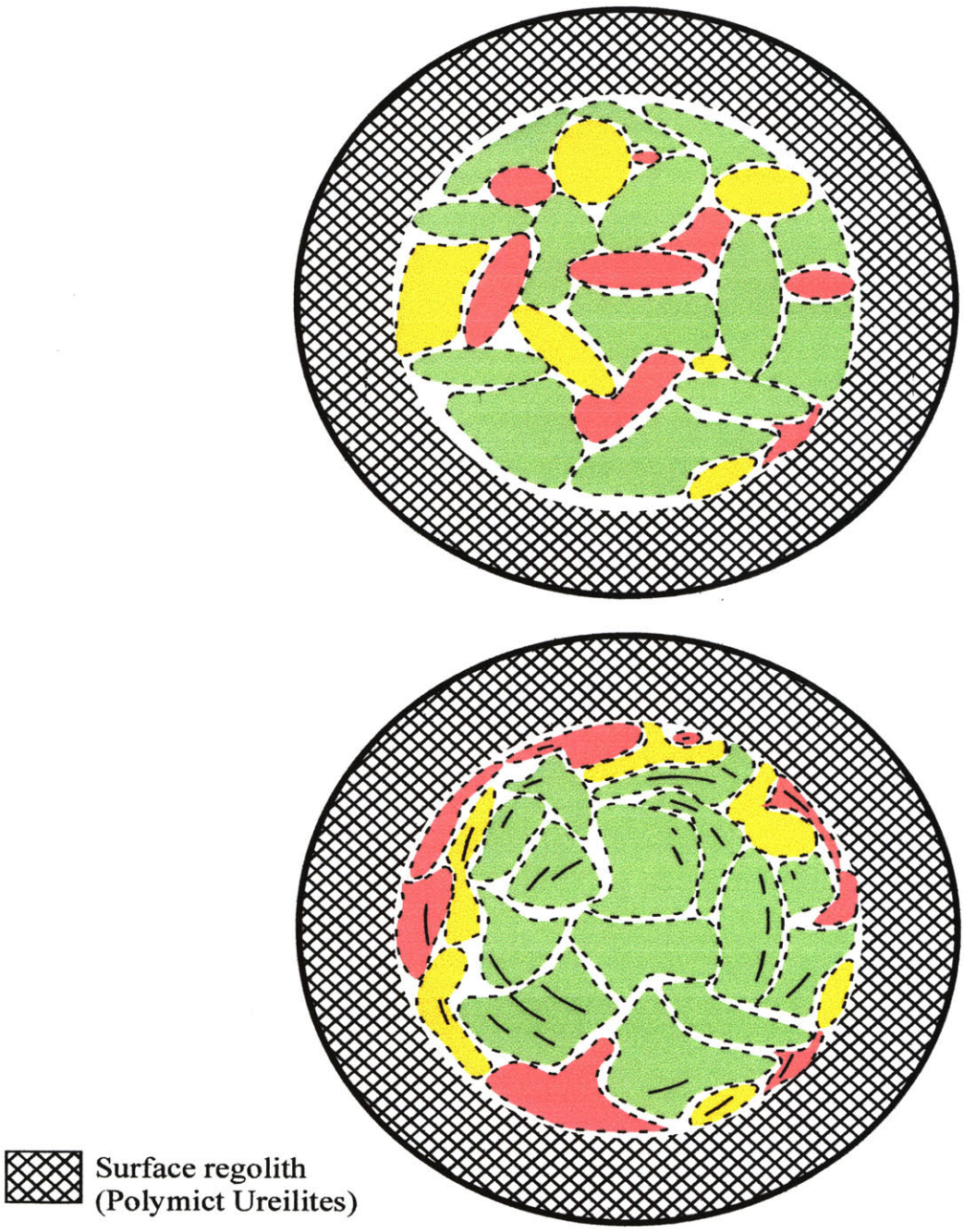

Surface regolith
(Polymict Ureilites)

Areas with high CAI concentrations
(high Mg# ureilites)

Areas of moderate CAI concentrations
(mid Mg# ureilites)

Areas with low CAI concentrations
(low Mg# ureilites)

Table 1. Synthetic bulk compositions used in this study.

	SiO_2	TiO_2	Al_2O_3	Cr_2O_3	FeO	MnO	MgO	CaO
Pu	54.09	0.52	6.56	0.76	14.36	0.21	9.80	13.72
Pu+Fo83.8	49.95	0.37	4.65	0.54	14.67	0.15	19.94	9.74
Pu+Fo75	49.54	0.37	4.65	0.54	16.84	0.15	18.17	9.74
ULM	50.64	0.57	11.97	0.68	14.50	0.32	9.59	11.74
ULM+Fo75	48.19	0.45	9.57	0.54	16.18	0.25	15.41	9.40
ULM+Fo75+Cpx	48.46	0.66	9.08	0.51	15.61	0.24	15.24	10.20

Table 2. Experimental run conditions and results.

Exp # *(bulk)*	t hrs	P bars	T C	Phase (#analysis)	F	SiO_2	TiO_2	Al_2O_3	Cr_2O_3	FeO	MnO	MgO	CaO	Total	mg#	$K_d^{phase/liq}$
Pu-12	13	125	1260	Ol (10)[a]	0.161	39.3(3)[b]	-[c]	-	0.39(2)	17.2(3)	0.15(2)	43.1(2)	0.49(3)	100.63	81.8	0.34
Pu+Fo 83.8				Pig (12)	0.164	56.3(6)	-	0.4(3)	0.56(9)	10.8(2)	0.13(2)	29.0(8)	3.9(6)	101.09	82.8	0.32
				Liquid (8)	0.66	52.1(2)	0.51(3)	6.9(1)	0.54(1)	14.7(2)	0.16(2)	12.5(2)	13.7(2)	101.11	60.3	
Pu-14	15	125	1230	Oliv (16)	0.374	38.8(4)	-	-	0.37(3)	19.0(3)	0.15(3)	41.5(5)	0.51(9)	100.33	79.6	0.32
Pu+Fo 83.8				Aug (2)	-	50.8(1)	0.69(5)	5.8(2)	0.87(3)	12.4(6)	0.12(1)	15.0(9)	15(2)	100.68	68.4	0.57
				Pig (13)	0.286	55.6(3)	0.07(3)	0.47(8)	0.57(6)	11.4(3)	0.14(3)	26.7(5)	5.9(7)	100.85	80.6	0.32
				Glass (33)	0.341	50.5(3)	0.63(7)	8.1(1)	0.46(3)	15.2(3)	0.18(2)	10.5(6)	14.1(4)	99.67	55.2	
Pu-15	8	125	1280	Oliv (5)	0.431	39.6(3)	-	-	0.39(3)	15.6(2)	0.12(2)	44.1(4)	0.45(2)	100.26	83.5	0.33
Pu+Fo 83.8				Pig (7)	0.026	56.9(3)	0.06(1)	0.30(4)	0.55(2)	9.7(3)	0.16(2)	30.0(7)	3.5(3)	101.17	84.6	0.31
				Glass (50)	0.546	52.3(2)	0.43(5)	6.41(7)	0.56(3)	13.9(2)	0.14(2)	13.1(1)	12.8(1)	99.64	62.7	
Pu-16	25	50	1230	Aug (8)	0.378	53.1(6)	0.79(3)	12.4(7)	0.25(8)	10.0(6)	0.14(2)	8(1)	14.7(5)	99.38	59	1.66
Pu+Fo 83.8				Pig (20)	0.468	56(2)	0.11(2)	0.8(3)	0.56(4)	8.0(8)	0.16(3)	29(2)	5.3(4)	99.93	86.8	0.36
				Glass (7)	0.068	53.3(7)	0.66(8)	10(1)	0.39(8)	9.1(6)	0.17(3)	12(3)	14(1)	99.62	70.4	
				Metallic iron	0.071	-	-	-	-	-	-	-	-			
Pu-17	16	50	1260	Pig (22)	0.473	56.5(4)	0.10(3)	0.5(3)	0.58(5)	7(1)	-	30(2)	6(2)	100.68	88.8	0.36
Pu+Fo 83.8				Aug (17)	0.021	55.5(6)	0.15(4)	0.5(1)	0.50(4)	4.0(9)	-	24(2)	15(3)	99.65	91.6	0.26
				Glass (15)	0.423	54.8(3)	1.3(3)	9.1(2)	-	7.6(4)	0.14(7)	12.0(5)	15.2(2)	100.14	73.8	
				Metallic iron	0.084	-	-	-	-	-	-	-	-			
Pu-18	22	75	1260	Pig (23)	0.463	57.1(6)	0.05(2)	0.4(1)	0.54(4)	7.9(5)	0.14(3)	29.3(6)	5.1(5)	100.53	86.8	0.32
Pu+Fo 83.8				Aug (5)	-	52.8(4)	0.60(6)	6(1)	0.8(1)	9.0(8)	0.13(2)	18(2)	14(1)	101.33	77.6	0.60
				Glass (26)	0.475	52.5(3)	0.60(5)	8.32(6)	0.48(3)	10.7(3)	0.15(2)	12.6(2)	14.6(2)	99.95	67.8	
				Metallic iron	0.062	-	-	-	-	-	-	-	-			
Pu-19	11	100	1260	Oliv (8)	0.136	39.8(3)	-	-	0.37(2)	15.8(3)	0.17(3)	43.9(4)	0.50(4)	100.54	83.2	0.33
Pu+Fo 83.8				Pig (21)	0.225	56.6(6)	0.06(2)	0.38(9)	0.51(4)	9.1(5)	0.09(3)	28.9(7)	4.8(5)	100.44	84.9	0.29
				Glass (54)	0.617	52.0(2)	0.47(5)	7.5(1)	0.43(4)	13.5(2)	0.05(3)	12.3(1)	14.0(2)	100.25	61.9	
				Metallic iron	0.022	-	-	-	-	-	-	-	-			
Pu-20	24	100	1230	Pig (18)	0.289	55.7(2)	0.07(2)	0.5(1)	0.52(4)	11.3(5)	0.17(2)	26.3(5)	6.3(7)	100.86	80.6	0.30
Pu+Fo 83.8				Oliv (14)	0.162	38.7(2)	-	-	0.35(1)	19.6(3)	0.16(1)	40.6(2)	0.54(5)	99.95	78.8	0.33
				Glass (18)	0.544	50.7(2)	0.7(1)	8.5(1)	0.40(7)	15.1(3)	0.17(7)	10.5(2)	14.2(1)	100.27	55.4	
				Metallic iron	t	-	-	-	-	-	-	-	-			

[a] Number in parenthesis indicates the number of analyses used for average

[b] Number in parenthesis is one sigma standard deviation in terms of least units cited. Therefore, 38.7(3) should be read as 38.7 ± 0.3wt%

[c] Indicates element not analyzed of below detectability limit

[d] Temperatures are estimated from power consumption levels during the experiment and verified using the Ol-Pig thermometer of Singletary and Grove (2003)

Exp #	t	P	T	Phase	F	SiO_2	TiO_2	Al_2O_3	Cr_2O_3	FeO	MnO	MgO	CaO	Total	mg#	$K_d^{phase/liq}$	SSR
	hrs	bars	C	(#analysis)													
Pu-22	28	80	1230	Pig (12)	0.546	56.3(5)	0.11(2)	0.6(1)	0.59(6)	9.1(6)	0.20(3)	27.9(8)	6.1(6)	100.90	84.6	0.28	1.689
Pu+Fo 83 8				Glass (43)	0.404	51.4(3)	0.6(1)	0.7(2)	0.45(8)	12.5(4)	0.14(4)	10.8(2)	14.5(2)	100.09	60.5		
				Metallic iron	0.050	-	-	-	-	-	-	-	-				
Pu-28	26	125	1260	Oliv (9)	0.182	38.8(5)	-	-	0.40(2)	20.1(7)	0.14(3)	40.1(6)	0.5(2)	100.04	78.1	0.35	0.1406
Pu+Fo 75				Aug (10)	0.398	52.2(5)	0.37(5)	2.4(3)	1.2(2)	13.2(9)	0.14(3)	16(1)	15(1)	100.51	68.8	0.48	
				Pig (3)	0.142	56.0(8)	0.03(1)	0.26(1)	0.56(8)	12.9(1)	0.12(2)	27.8(1)	3.3(1)	100.97	79.4	0.33	
				Glass (47)	0.278	51.0(3)	0.38(5)	6.4(5)	0.46(8)	17.2(9)	0.18(2)	12(1)	12.7(4)	100.32	55.5		
Pu-30	21	75	1260	Aug (6)	0.098	55.1(2)	0.10(2)	0.26(4)	0.52(5)	5.7(5)	0.15(2)	21.9(8)	16(1)	99.73	87.2	0.28	0.4011
Pu+Fo 75				Pig (5)	0.344	56.3(9)	0.08(1)	0.44(2)	0.57(5)	7.0(3)	0.15(2)	31.2(6)	4.3(6)	100.04	88.8	0.24	
				Glass (14)	0.467	55.2(3)	0.5(1)	9(2)	0.4(2)	10(1)	0.15(4)	11(3)	14.1(5)	100.35	63.9		
				Metallic iron	0.092	-	-	-	-	-	-	-	-				
ULM-1	16	115	1260	Pig (4)	0.018	55.7(3)	0.07(2)	0.47(6)	0.9(2)	9.5(4)	0.40(3)	29.3(5)	3.1(5)	99.44	84.6	0.26	0.7758
ULM				Glass (20)	0.946	53.2(4)	0.5(1)	12.0(2)	0.60(7)	11.5(3)	0.39(7)	9.2(2)	12.4(3)	99.79	58.7		
				Metal	0.036	-	-	-	-	-	-	-	-				
ULM-2	26	115	1200	Glass (24)	0.981	50.1(3)	0.6(2)	13.4(2)	0.39(4)	12.6(3)	0.40(5)	9.0(2)	13.2(2)	99.69	55.9		4.9990
ULM				Metal	0.019	-	-	-	-	-	-	-	-				
ULM-4	30	115	1150	Glass (13)	0.144	52.2(4)	0.36(8)	12.1(4)	0.13(6)	14.5(4)	0.36(5)	6.0(6)	12.7(3)	98.35	42.2		5.7007
ULM				Pyx (15)	0.855	53.8(3)	0.07(2)	1.1(4)	0.63(7)	15.8(6)	0.42(5)	22.7(7)	4.5(7)	99.02	72.0	0.29	
				Metal	0.001	-	-	-	-	-	-	-	-				
ULM-5	24	110	1180	Glass (34)	0.720	48.0(3)	0.4(1)	12.6(1)	0.22(6)	15.5(5)	0.31(5)	7.8(4)	12.7(3)	97.53	47.3		0.2540
ULM+Fo 75				Olivine (11)	0.192	37.2(7)	-	0.02(1)	0.18(1)	24(3)	0.28(1)	37(3)	0.43(2)	99.11	72.8	0.33	
				Pyx (14)	0.107	52.9(6)	0.10(1)	0.9(3)	0.63(7)	18(3)	0.27(3)	23(2)	3.1(4)	98.90	70.0	0.38	
				Metal	-0.018	-	-	-	-	-	-	-	-				
ULM-8	20	120 b	1230	Glass (50)	0.886	51.3(3)	0.48(5)	11.0(1)	0.43(3)	15.5(2)	0.22(3)	11.1(2)	10.5(1)	100.53	56.2		0.0887
ULM+Fo 75				Olivine (16)	0.184	38.8(6)	0.03(2)	0.05(1)	0.35(2)	19.5(3)	0.26(2)	41.3(9)	0.36(2)	100.65	79.1	0.34	
				Opx (34)	-0.070	56.2(6)	0.08(3)	1.0(5)	0.72(7)	12.5(4)	0.21(3)	28.2(9)	1.8(3)	100.71	80.2	0.32	
ULM-9	11	110	1300	Glass (21)	0.854	49.7(3)	0.59(5)	11.0(1)	0.43(4)	15.0(4)	0.24(3)	11.6(6)	11.1(4)	99.66	57.9		0.0467
ULM+Fo 75				Olivine (7)	0.111	39.2(4)	0.01(1)	0.05(3)	0.37(5)	16.9(4)	0.23(2)	43.1(7)	0.37(2)	100.23	81.9	0.30	
				Opx (4)	0.023	56.4(2)	0.03(1)	0.33(1)	0.51(2)	12.1(6)	0.22(4)	29.7(5)	1.1(1)	100.39	81.2	0.32	
				Metal	0.012	-	-	-	-	-	-	-	-				
ULM-10	12	75	1230	Glass (85)	0.742	50.2(9)	0.56(7)	12.2(7)	0.50(4)	10.5(4)	0.29(3)	12.2(2)	12.6(6)	99.05	67.4		0.3134
ULM+Fo 75				Olivine (12)	0.177	39.6(8)	0.01(1)	0.03(1)	0.39(2)	13.2(4)	0.27(3)	46(1)	0.34(4)	99.84	86.1	0.34	
				Pyx (24)	0.015	56.6(7)	0.05(2)	0.5(1)	0.58(5)	8.3(6)	0.30(4)	31.4(6)	2.1(2)	99.83	87.0	0.31	
				Metal	0.066	-	-	-	-	-	-	-	-				
ULM-11	18	115	1200	Liquid (70)	0.759	49.8(3)	0.7(1)	12.6(2)	0.26(7)	13.9(4)	0.27(5)	9.1(4)	12.5(2)	99.13	53.8		0.0840
ULM+Fo 75				Olivine (13)	-0.138	38.2(4)	0.02(2)	0.05(1)	0.26(2)	20.7(2)	0.29(3)	39.8(4)	0.43(4)	99.75	77.5	0.34	
				Opx (16)	0.209	55.0(4)	0.07(2)	0.8(2)	0.62(9)	13.8(5)	0.26(3)	27.0(3)	2.6(2)	100.15	77.5	0.33	
				Pig (6)	0.160	54.0(9)	0.14(5)	2.0(9)	0.78(7)	12(1)	0.29(3)	26(1)	4.9(4)	100.11	79.1	0.31	
				Metal	0.010	-	-	-	-	-	-	-	-				

Exp #	t hrs	P bars	T C	Phase (#analysis)	F	SiO_2	TiO_2	Al_2O_3	Cr_2O_3	FeO	MnO	MgO	CaO	Total	mg#	$K_d^{phase/liq}$	SSR
ULM-12	14.5	90	1200	Liquid (7)	0.610	52(2)	0.65(5)	11.7(4)	0.25(8)	15.5(4)	0.28(6)	6.2(6)	12(2)	98.58	41.7		0.0782
ULM+Fo 75				Pig (4)	0.074	53.7(6)	0.15(5)	1(1)	0.62(3)	15.7(2)	0.32(4)	24(1)	3.5(7)	98.99	73.5	0.26	
				Olivine (10)	0.235	38.2(6)	0.03(2)	0.06(1)	0.28(2)	20(2)	0.28(6)	41(1)	0.50(7)	100.35	78.8	0.19	
				Plag (2)	0.079	44(2)	-	29(7)	-	3(2)	-	3(3)	19.6(4)	98.60			
				Metal	0.010	-	-	-	-	-	-	-	-				
LMC-1	12	90	1230	Liquid (66)	0.842	49.9(4)	0.8(1)	10.7(2)	0.46(7)	14.1(3)	0.25(4)	11.7(2)	11.9(2)	99.81	59.8		0.0125
ULM+Fo 75 +CPX				Pyx (7)	0.055	54(1)	0.05(3)	0.6(3)	0.54(3)	11.3(5)	0.20(3)	30(1)	3.0(6)	99.69	82.4	0.32	
				Olivine (19)	0.087	39.0(5)	0.03(2)	0.04(1)	0.37(2)	17.0(3)	0.19(2)	42.8(6)	0.38(3)	99.81	81.7	0.33	
				Metal	0.017	-	-	-	-	-	-	-	-				
LMC-2	23	115	1230	Liquid (26)	0.877	50.7(3)	0.8(1)	10.4(4)	0.38(7)	14.8(2)	0.22(5)	10.8(3)	11.7(2)	99.80	56.6		0.0263
ULM+Fo 75 +CPX				Pyx (18)	-0.051	55.7(5)	0.08(4)	0.7(5)	0.61(6)	12.1(1)	0.18(2)	28.5(7)	2.8(4)	100.67	80.8	0.31	
				Olivine (6)	0.173	38.5(3)	-	0.04(1)	0.27(7)	18.7(2)	0.19(2)	41.4(3)	0.36(3)	99.46	79.8	0.33	
				Metal	t	-	-	-	-	-	-	-	-				
LMC-3	24	115	1200	Liquid (16)	0.762	49.5(3)	0.8(1)	11.7(1)	0.38(8)	14.3(4)	0.18(4)	9.1(1)	12.8(2)	98.76	53.2		0.0151
ULM+Fo 75 +CPX				Pyx (11)	0.081	54.4(5)	0.08(3)	0.9(1)	0.70(5)	13.3(2)	0.22(2)	26.0(6)	4.0(4)	99.60	77.8	0.32	
				Olivine (3)	0.154	38.5(9)	-	0.06(2)	0.35(2)	20.5(3)	0.27(2)	39.5(4)	0.42(2)	99.60	77.4	0.33	
				Metal	0.003	-	-	-	-	-	-	-	-				
LMC-4	23	90	1200	Liquid (19)	0.762	49.7(3)	0.8(1)	11.7(2)	0.35(8)	13.8(3)	0.16(4)	9.5(1)	12.7(2)	98.71	54.9		0.0224
ULM+Fo 75 +CPX				Pyx (11)	0.098	54.6(4)	0.09(3)	0.8(4)	0.6(1)	12.9(5)	0.22(2)	26.8(6)	3.7(4)	99.71	78.8	0.33	
				Olivine (3)	0.129	38.0(4)	-	0.03(2)	0.35(2)	20.0(3)	0.24(2)	40.9(4)	0.42(4)	99.94	78.5	0.33	
				Metal	0.011	-	-	-	-	-	-	-	-				
LMC-5	27	115	1185	Liquid (24)	0.844	49.6(3)	0.9(1)	12.2(3)	0.31(5)	14.5(4)	0.21(4)	8.7(2)	12.6(2)	99.02	51.6		0.0496
ULM+Fo 75 +CPX				Olivine (8)	0.193	38.0(6)	-	0.10(2)	0.31(2)	21.7(2)	0.29(2)	39.0(5)	0.49(5)	99.89	76.2	0.33	
				Pyx (14)	0.014	54.0(6)	0.11(3)	1.0(2)	0.65(7_	14.5(5)	0.25(3)	24.7(7)	4.6(8)	99.81	75.2	0.35	
				Metal	t	-	-	-	-	-	-	-	-				
				Plag (2)	q	45.4(5)	-	32.1(5)	-	1.8(6)	-	2.0(2)	17.3(5)	98.60			
LMC-6	24	55	1200	Liquid (18)	0.782	50.5(4)	0.9(1)	11.6(3)	0.42(7)	15.0(4)	0.25(4)	8.8(5)	12.7(3)	99.87	51.0		0.0125
ULM+Fo 75 +CPX				Olivine (9)	0.184	38.0(6)	-	0.06(2)	0.38(2)	21.0(4)	0.21(4)	40.0(8)	0.42(4)	100.07	77.2	0.31	
				Pyx (16)	0.383	54.8(6)	0.12(4)	1.0(3)	0.76(9)	12(1)	0.23(3)	27.7(8)	3.8(5)	100.41	81.0	0.24	
				Metal	t	-	-	-	-	-	-	-	-				
LMC-7	24	75	1200	Liquid (78)	0.803	50.8(7)	0.8(1)	11.3(4)	0.34(7)	15.0(4)	0.17(4)	9.2(3)	12.6(2)	100.21	52.2		0.0308
ULM+Fo 75 +CPX				Olivine (10)	0.189	38.8(4)	-	-	0.37(3)	20(1)	0.22(3)	40.5(7)	0.42(6)	100.31	78.5	0.30	
				Pyx (10)	0.083	55.2(3)	0.09(3)	0.6(2)	0.56(7)	13.5(6)	0.21(2)	26.9(5)	3.7(2)	100.76	78.0	0.31	
				Metal	t	-	-	-	-	-	-	-	-				
LMC-8	26	115	1170	Liquid (64)	0.707	49.2(3)	1.0(1)	12.8(2)	0.31(6)	14.8(3)	0.16(4)	8.2(2)	13.1(2)	99.57	49.5		0.0348
ULM+Fo 75 +CPX				Olivine (7)	0.156	38.3(5)	-	0.07(2)	0.30(1)	22.5(4)	0.23(2)	38.3(5)	0.51(5)	100.21	75.2	0.32	
				Pyx (56)	0.137	54.0(6)	0.16(4)	1.2(4)	0.67(9)	14.0(7)	0.24(3)	24(1)	6(1)	100.27	75.5	0.32	
				Plag (12)	t	43.6(6)	-	34.5(9)	-	1.1(4)	-	0.6(5)	19.4(3)	99.20			
				Metal	t	-	-	-	-	-	-	-	-				

Exp #	t hrs	P bars	T C	Phase (#analysis)	F	SiO_2	TiO_2	Al_2O_3	Cr_2O_3	FeO	MnO	MgO	CaO	Total	mg#	$K_d^{phase/liq}$	SSR
LMC-9	23 h	75 b	1170	Liquid (33)	0.705	49.2(5)	0.9(2)	12.8(4)	0.33(6)	14.5(4)	0.22(4)	8.3(3)	13.1(2)	99.35	50.3		0.0739
ULM+Fo 75 +CPX				Oliv (22)	0.145	38.4(6)	-	0.05(2)	0.32(2)	21.6(5)	0.20(3)	38.8(7)	0.45(3)	99.82	76.2	0.32	
				Pig (15)	0.148	54.8(7)	0.16(4)	1.0(4)	0.68(8)	13.5(3)	0.18(4)	25.5(6)	4.7(5)	100.52	77.1	0.30	
				Metal	0.002	-	-	-	-	-	-	-	-				
LMC-10	22 h	115 b	1160	Liquid (107)	0.798	49.1(4)	0.9(1)	12.4(5)	0.27(7)	15.3(3)	0.21(4)	8.1(8)	12.8(8)	99.08	48.4		0.0574
ULM+Fo 75 +CPX				Pig (19)	0.046	53.9(7)	0.16(9)	2(1)	0.72(9)	14.0(4)	0.23(3)	24(2)	5.4(9)	100.41	75.1	0.31	
				Oliv (12)	0.208	38.1(9)	-	-	0.26(2)	23.1(7)	0.20(2)	37(2)	-	98.66	73.9	0.33	
				Plag(5)	-0.031	45(1)	-	31(4)	-	2(1)	-	-	18(2)	96.00			
				Metal	-0.021	-	-	-	-	-	-	-	-				
LMC-11	14	75	1230	Liquid(26)	0.823	51.9(4)	0.84	11.00	0.41	11.18	0.20	11.41	12.16	99.10	64.5		0.0240
ULM+Fo 75 +CPX				Pig (14)	0.015	56.7(5)	0.09(3)	0.5(1)	0.56(4)	8.8(8)	0.21(2)	30.7(8)	2.5(3)	100.06	86.1	0.29	
				Oliv(5)	0.115	40.1(2)	-	0.06(1)	0.33(8)	12.4(1)	0.17(2)	46.2(9)	0.37(5)	99.63	86.9	0.27	
				Metal	0.048	-	-	-	-	-	-	-	-				
LMC-12	18	90	1170	Liquid (15)	0.754	49.8(2)	0.9(1)	12.2(4)	0.26(7)	15.2(6)	0.23(6)	8.4(9)	12.7(5)	99.69	49.6		0.1349
ULM+Fo 75 +CPX				Olivine (6)	0.165	36.9(3)	-	-	0.15(5)	22.0(3)	0.08(2)	39.8(2)	0.50(4)	99.43	76.3	0.31	
				Pyx (2)	0.090	53.9(3)	.04(3)	0.14(6)	0.19(4)	15(1)	0.09(2)	25.8(5)	3.7(2)	98.86	75.1	0.33	
				Metal	0.009	-	-	-	-	-	-	-	-				
ULM+Fo 75 +CPX				Olivine (5)	0.128	39.5(5)	-	-	0.38(1)	17.3(4)	0.18(2)	42.7(7)	0.34(5)	100.40	81.4	0.33	
				Pyx (7)	-0.009	56.2(4)	0.07(2)	0.4(1)	0.54(4)	10.0(4)	0.18(3)	30.2(4)	2.1(2)	99.69	84.3	0.27	
				Metal	0.012	-	-	-	-	-	-	-	-				
LMC-17	16	90	~1280[d]	Liquid (14)	0.819	51.2(3)	0.8(1)	11.1(1)	0.45(9)	11.8(3)	0.19(3)	11.4(3)	12.1(1)	99.04	63.2		0.0380
ULM+Fo 75 +CPX				Pyx (12)	0.048	56.4(7)	0.04(3)	0.2(1)	0.4(1)	9.5(4)	0.13(5)	31.6(6)	2.1(2)	100.37	85.6	0.29	
				Olivine (4)	0.091	38.2(6)	-	0.03(2)	0.20(3)	13.3(4)	0.09(2)	47.2(7)	0.29(4)	99.31	86.3	0.27	
				Metal	0.042	-	-	-	-	-	-	-	-				
LMC-18	9	75	~1280[d]	Liquid (10)	0.826	52.8(4)	0.74(2)	10.9(1)	0.56(8)	9.1(2)	0.24(3)	12.8(2)	12.2(2)	99.34	71.4		0.0029
ULM+Fo 75 +CPX				Olivine (2)	0.076	40.6(6)	-	0.06(0)	0.41(0)	9.4(3)	0.16(1)	48.7(9)	0.37(1)	99.70	90.2	0.27	
				Pyx (5)	0.027	56.4(5)	0.06(2)	0.3(2)	0.4(1)	7.5(2)	0.17(5)	32.7(8)	2.0(3)	99.53	88.7	0.32	
				Metal	0.071	-	-	-	-	-	-	-	-				
LMC-21	18	75	1185	Liquid (12)	0.711	49.9(4)	0.9(1)	12.8(1)	0.40(6)	13.2(2)	0.19(6)	8.6(1)	13.1(2)	99.09	53.9		
ULM+Fo 75 +CPX				Olivine (5)	0.278	38.6(3)	-	-	0.36(6)	19.7(3)	0.21(2)	40.1(3)	0.6(2)	99.57	78.4	0.32	
				Pyx (20)	0.146	54.9(7)	0.15(4)	1.1(3)	0.7(1)	12(1)	0.24(3)	25(1)	4.8(6)	98.89	78.6	0.32	
				Metal	0.021	-	-	-	-	-	-	-	-				
LMC-22	21	75	1260	Liquid (28)	0.772	49.1(4)	0.81(9)	12.1(1)	0.53(6)	12.5(3)	0.23(5)	11.6(3)	12.2(3)	99.07	62.1		
ULM+Fo 75 +CPX				Olivine (14)	0.027	39.1(4)	-	0.03(1)	0.36(3)	15.6(7)	0.15(3)	44.1(8)	0.34(5)	99.68	83.5	0.33	
				Pyx (25)	0.172	56.0(4)	0.06(2)	0.5(1)	0.53(5)	10.5(5)	0.20(3)	30.0(8)	2.3(4)	100.09	83.6	0.32	

Exp #	t	P	T	Phase	F	SiO_2	TiO_2	Al_2O_3	Cr_2O_3	FeO	MnO	MgO	CaO	Total	mg#	$K_d^{phase/liq}$	SSR
	hrs	bars	C	(#analysis)													
LMC-23	12	90	1260	Liquid (20)	0.888	52.0(3)	0.82(8)	10.3(2)	0.51(8)	13.0(3)	0.18(3)	12.3(2)	11.5(2)	100.61	62.8		
ULM+Fo $_{75}$ +CPX				Olivine (15)	0.128	39.0(5)	-	-	0.39(3)	15.8(5)	0.17(2)	44.4(8)	0.33(3)	100.09	83.3	0.34	
				Pyx (9)	-0.047	56.0(6)	0.08(2)	0.5(2)	0.57(4)	11.5(4)	0.18(3)	29.2(4)	2.4(5)	100.43	81.9	0.37	
				Metal	0.026	-	-	-	-	-	-	-	-				
LMC-24	15	115	1260	Liquid (20)	0.923	50.4(2)	0.8(1)	9.8(1)	0.44(5)	14.7(4)	0.12(4)	11.5(2)	11.3(2)	99.06	41.9		
ULM+Fo $_{75}$ +CPX				Olivine (8)	0.168	39.1(3)	0.03(1)	0.03(1)	0.35(3)	18.2(2)	0.18(2)	42.2(7)	0.37(3)	100.46	80.4	0.34	
				Pyx (12)	-0.084	55.6(5)	0.08(2)	0.5(1)	0.54(5)	12.2(4)	0.19(2)	28.8(6)	2.4(3)	100.31	80.9	0.33	
				Metal	t	-	-	-	-	-	-	-	-				
LMC-25	23	90	1185	Liquid (13)	0.710	49.8(2)	0.9(1)	12.6(1)	0.21(5)	14.9(4)	0.18(4)	8.3(2)	13.2(2)	100.09	49.8		
ULM+Fo $_{75}$ +CPX				Olivine (14)	0.149	37.8(4)	0.04(2)	0.07(3)	0.27(6)	22.7(3)	0.22(3)	39.1(3)	0.48(5)	100.68	75.4	0.32	
				Pyx (19)	0.138	54.6(7)	0.15(7)	1.4(8)	0.72(7)	13.7(3)	0.23(2)	25(1)	4.8(8)	100.60	76.8	0.30	
				Metal	t	-	-	-	-	-	-	-	-				

Table 3. Liquid normalized reaction coefficents (in wt%)

Subtraction of Modal Proportions

Temp (C)	ΔP	Bulk	C	+	Ol	+	Liq	=>	Pyx	+	Fe	+	CO	10%
1280	40	LMC	0.23		1.21		1		0.43		1.06		0.53	N
1280	25	LMC	0.10		0.74		1		0.79		0.46		0.23	N
1260	25	Pu+Fo83.8	0.06		0.52		1		1.18		0.28		0.14	Y
1260	25	Pu+Fo83.8	0.05		0.96		1		1.68		0.22		0.11	Y
1260	50	Pu+Fo83.8	0.05		0.84		1		1.55		0.23		0.12	Y
1230	25	Pu+Fo83.8	0.04		1.94		1		0.80		0.20		0.10	N
1230	20	Pu+Fo83.8	0.04		1.16		1		1.84		0.16		0.08	Y
1230	25	LMC	0.08		2.46		1		3.03		0.37		0.19	Y
1230	40	LMC	0.15		1.07		1		1.21		0.68		0.34	Y
1230	15	LMC	0.27		1.45		1		2.08		1.24		0.62	N
1200	15	LMC	0.05		1.45		1		2.14		0.25		0.12	Y
1200	40	LMC	0.02		0.86		1		1.74		0.10		0.05	Y

Mass Balance

Temp (C)	ΔP	Bulk	C	+	Ol	+	Liq	=>	Pyx	+	Fe	+	CO	10%
1280	40	LMC	0.18		0.56		1		0.35		0.88		0.44	Y
1280	25	LMC	0.08		0.24		1		0.72		0.37		0.19	Y
1260	15	LMC	0.02		0.93		1		1.92		0.09		0.04	Y
1260	40	LMC	0.04		0.86		1		1.62		0.17		0.07	Y
1260	25	Pu+Fo83.8	0.05		0.52		1		1.32		0.23		0.12	Y
1260	25	LMC	0.11		0.68		1		0.62		0.53		0.27	N
1230	25	Pu+Fo83.8	0.03		0.53		1		1.18		0.12		0.05	N
1230	50	ULM	0.07		1.11		1		1.79		0.33		0.16	Y
1230	40	LMC	0.13		0.65		1		0.98		0.61		0.30	Y
1230	25	LMC	0.07		2.37		1		3.03		0.30		0.15	Y
1230	15	LMC	0.24		2.00		1		2.14		1.11		0.56	N
1200	40	LMC	0.04		1.33		1		2.43		0.20		0.10	N
1200	15	LMC	0.08		1.71		1		2.66		0.35		0.18	N
1200	60	LMC	0.14		3.66		1		4.79		0.67		0.34	N
1200	35	LMC	0.20		3.88		1		4.47		0.92		0.46	N
1200	20	LMC	0.01		0.29		1		1.33		0.03		0.01	Y
1200	25	LMC	0.14		7.93		1		6.47		0.63		0.32	N

Table 4. Normalized Smelting Reaction Coefficients

Subtration of Modal Proportions

Temp (C)	ΔP	Bulk	C	+	Ol	+	Liq	=>	Pyx	+	Fe	+	CO
1260	25	Pu+Fo83.8	0.04		0.34		0.63		0.75		0.18		0.07
1260	25	Pu+Fo83.8	0.02		0.48		0.50		0.84		0.11		0.05
1260	50	Pu+Fo83.8	0.03		0.44		0.53		0.82		0.12		0.06
1230	20	Pu+Fo83.8	0.02		0.53		0.45		0.84		0.07		0.09
1230	25	LMC	0.03		0.69		0.28		0.86		0.10		0.04
1230	40	LMC	0.07		0.48		0.45		0.55		0.31		0.14
1200	15	LMC	0.02		0.58		0.40		0.86		0.10		0.04
1200	40	LMC	0.01		0.46		0.53		0.93		0.05		0.02

Mass Balance

Temp (C)	ΔP	Bulk	C	+	Ol	+	Liq	=>	Pyx	+	Fe	+	CO
1280	40	LMC	0.10		0.32		0.58		0.20		0.51		0.29
1280	25	LMC	0.06		0.18		0.76		0.55		0.28		0.17
1260	15	LMC	0.01		0.48		0.51		0.94		0.04		0.02
1260	40	LMC	0.02		0.45		0.53		0.85		0.09		0.06
1260	25	Pu+Fo83.8	0.03		0.33		0.64		0.79		0.14		0.07
1230	50	ULM	0.03		0.51		0.46		0.79		0.14		0.07
1230	40	LMC	0.07		0.37		0.56		0.52		0.32		0.16
1230	25	LMC	0.02		0.69		0.29		0.87		0.09		0.04
1200	20	LMC	0.01		0.22		0.77		0.97		0.02		0.01

Table 5. Sample Model out put at 1260°C

Step #	Phase		SiO_2	TiO_2	Al_2O_3	Cr_2O_3	FeO	MgO	CaO
Input	Residue		39.60	0.04	0.84	0.05	22.01	36.11	1.34
	Liquid		50.40	0.80	9.80	0.44	14.70	11.50	11.30
1	Olivine	Fo=80.9	39.33	-	-	-	18.00	42.67	-
	Pigeonite		56.27	0.04	0.43	0.40	10.66	29.77	2.44
	Residue		38.83	0.04	0.81	0.06	21.40	34.65	1.35
	Liquid		50.80	0.83	10.11	0.44	14.68	11.56	11.59
2	Olivine	Fo=81.0	39.34	-	-	-	17.91	42.75	-
	Pigeonite		56.28	0.04	0.43	0.40	10.60	29.82	2.44
	Residue		39.22	0.04	0.81	0.07	21.44	34.22	1.40
	Liquid		50.66	0.84	10.31	0.44	14.50	11.50	11.76
3	Olivine	Fo=81.1	39.36	-	-	-	17.82	42.82	-
	Pigeonite		56.30	0.04	0.43	0.40	10.54	29.86	2.44
	Residue		39.57	0.04	0.81	0.08	21.47	33.82	1.45
	Liquid		50.51	0.86	10.52	0.43	14.32	11.43	11.93
4	Olivine	Fo=81.2	39.38	-	-	-	17.73	42.90	-
	Pigeonite		56.31	0.04	0.43	0.40	10.49	28.90	2.44
	Residue		39.97	0.04	0.80	0.09	21.50	3.42	1.50
	Liquid		50.36	0.88	10.73	0.43	14.13	11.36	12.11
5	Olivine	Fo=81.3	39.39	-	-	-	17.63	42.97	-
	Pigeonite		56.33	0.04	0.43	0.40	10.42	29.94	2.45
	Residue		40.33	0.04	0.80	0.10	21.53	33.03	1.54
	Liquid		50.20	0.89	10.95	0.43	13.94	11.30	12.30
6	Olivine	Fo=81.4	39.41	-	-	-	17.53	43.05	-
	Pigeonite		56.34	0.04	0.43	0.40	10.36	29.99	2.45
	Residue		40.69	0.04	0.80	0.11	21.56	32.64	1.59
	Liquid		50.05	0.91	11.17	0.42	13.74	11.22	12.48
7	Olivine	Fo=81.5	39.43	-	-	-	17.43	43.14	-
	Pigeonite		56.36	0.04	0.43	0.40	10.30	30.04	2.45
	Residue		41.04	0.04	0.79	0.13	21.59	32.27	1.63
	Liquid		49.88	0.93	11.40	0.42	13.55	11.15	12.67
8	Olivine	Fo=81.6	39.45	-	-	-	17.33	43.22	-
	Pigeonite		56.38	0.04	0.43	0.40	10.23	30.08	2.45
	Residue		41.38	0.04	0.79	0.14	21.16	31.90	1.68
	Liquid		49.72	0.95	11.64	0.41	13.34	11.08	12.86
9	Olivine	Fo=81.7	39.47	-	-	-	17.22	43.31	-
	Pigeonite		56.39	0.04	0.43	0.40	10.16	30.13	2.45
	Residue		41.71	0.04	0.79	0.14	21.64	31.54	1.72
	Liquid		49.55	0.97	11.87	0.41	13.14	11.00	13.06

Chp. 3 Partial Melting Experiments of Allende CV3 material

Abstract

Models of planetary formation frequently ignore the effects of small body processes. Early models assumed the formation of a planetary sized body of primitive composition then allow differentiation to occur. Such models have encountered problems when applied to the Earth. Models of Earth formation and differentiation from a CI chondrite starting composition require silica removal to the core that results in a residual, silica undersaturated mantle, and leads to an overabundance of platinum group elements in the mantle.

We present new data from reconnaissance low pressure melting experiments on the Allende CV3 meteorite. The experiments were designed to explore the melting behavior of primitive compositions on small bodies in the early solar system and to examine the effect of removal of that melt on the residue composition. The results are then applied to previous models of planetary formation. We find that moderate pressures of ~10 MPa, equivalent to depths of ~100 km, greatly influence the composition of melt generated from primitive materials. Melting experiments using the Allende CV3 meteorite at 0.1 MPa show that some of the achondrite meteorites can be linked to the primitive meteorites in our collections. Low degree melts enriched in K, Al, Na are removed from the parent bodies and may provide a residue capable of generating ureilites.

Introduction

The carbonaceous chondritic meteorites (CC) are widely accepted as representing the most primitive materials represented in our meteorite collections. They contain similar abundances of non-gaseous elements compared to the solar photosphere (Anders and Grevesse, 1989) and can be considered as an approximation of the composition of the primitive solar nebula. The compositions of the different CCs have been used in modeling and experimental studies to gain insight into the processes that occurred in the early solar nebula and to understand how the planetary bodies in the solar system came to acquire their unique compositional characteristics (e.g. Ringwood, 1966a; Seitz and Kushiro, 1974; Agee, 1990; Jurewicz *et al*, 1993; Agee *et al*, 1995). This study presents

the results of a set of reconnaissance experiments using the Allende CV3 meteorite at pressures and temperatures appropriate for small bodies (<100 km radius) that are being heated by decay of short lived isotopes during early solar system evolution. We use the results of these experiments to explore the consequences of partial melting and differentiation on small parent bodies.

Previous Experimental Studies

Several experimental studies have been performed to explore planetary differentiation using CC meteorites. Agee *et al* (1995) determined the phase relations for Allende from pressures of 1 to 27 GPa. Their phase diagram is shown in Figure 1. At 1.0 GPa, Agee *et al* (1995) found only olivine and spinel as liquidus phases. Jurewicz et al (1993) investigated the 0.1 MPa melting behavior of Allende and Murchison (CM2) over a range of temperatures and oxygen fugacities. They found the solidus to be at ~1140°C with olivine and spinel as the most abundant phases along with trace amounts of plagioclase and ± metal dependent upon oxygen fugacity. Jurewicz *et al* (1993) also found that at fO_2 values below Iron-Wustite (IW), low degree partial melts of Allende had eucritic affinities, while at higher fO_2 (IW+2) angritic type melts were generated. All of the experimental melts in the Jurewicz *et al* (1993) study are severely depleted in Na_2O and P_2O_5. Similar results have been obtained by other workers who have studied the melting behavior and phase assemblages of Allende at similar pressures and temperatures (Seitz and Kushiro, 1974; Agee, 1990, 1993).

While the previous investigations contributed much to our knowledge of the igneous evolution of the solar system, an important region of pressure-temperature space remains unexplored – specifically pressures of 2.5 to 25 MPa that would reproduce the conditions expected on bodies greater than 50 km but less than 250 km in radius. The presence of bodies of this size in the early solar system is implied from the existence of various meteorite types that have old ages and record igneous processing at such pressures. One such group, the ureilites, records the effects of smelting – a process that is suppressed at pressures exceeding 25 MPa (Walker and Grove, 1993; Singletary and Grove, 2003).

Experimental Procedure

All experiments reported here were performed in the MIT Experimental Petrology Laboratory. Allende CV3 whole rock powder was used as the starting material for these experiments. A 10g chunk of Allende, donated by R. Kempton of New England Meteoritical Services, was gently crushed in an agate mortar and then sieved to a grain size <54μm. Great care was taken to ensure that all of the material passed through the sieve and that there was no differentiation of material (i.e. metal being left behind).

Approximately 10 to 15 mg of the WR powder was packed into a handcrafted carbon capsule. The carbon capsule was then inserted into a platinum tube that was welded shut on one end and loosely crimped on the other. A small hole was made in the crimped end to ensure the gas pressure and fO_2 of the interior environment were fully transmitted to the interior of the experimental charge. The finished assembly, with the welded end at the bottom, was loaded into the pressure vessel.

The experiments were performed in a rapid quench, externally heated, ZHM alloy, cold seal pressure vessel contained in an inconel 600 sheath. The pressure vessel has an inner diameter of 0.25" and was surrounded by argon to prevent oxidation. Once sealed, the vessel is pressurized with CO gas that serves both as the pressure medium and to ensure a reducing environment. The vessel is then placed in a vertical Del Tech furnace and brought to run temperature. At the end of the experiment, the vessel is extracted from the furnace and inverted to drop the experimental charge to the cold region of the vessel. Rapping the end of the pressure vessel with a wrench assists in making sure the charge falls to the cooling head.

Experiments were then removed from the pressure vessel and extracted from the Pt tube and carbon capsule. Frequently the experiment would come out as a coherent charge of melt and crystals and other times as a loose aggregate of glass beads and crystals. The bead(s) and/or crystals were then crushed in a Plattner mortar and mounted in epoxy. The mounts were then polished and carbon coated for microprobe analysis (see Fig. 2 and 3 for examples of prepared experiments).

Microprobe analysis was performed using the MIT JEOL 733 Superprobes utilizing the appropriate glass and silicate standards. Crystal phases in the experiments were analyzed using a beam current of 10 nA, accelerating voltage of 15 kV and a spot size of 2 μm. Glasses were analyzed under the same conditions but with a spot size of 10 μm to reduce the effects of small quench phases. The CITZAF correction package of Armstrong (1995) was used to reduce the data. The atomic number correction of Duncomb and Reed, the Heinrichs tabulation of absorption coefficients, and the fluorescence correction of Armstrong were used to obtain a quantitative analysis (Armstrong, 1995).

Approach to Equilibrium

The use of a natural starting material makes the evaluation of equilibrium crucial as pre-existing phases must be homogenized so that accurate results can be obtained. The first three experiments listed in Table 1 were performed with a 93 μm powder. Frequently, relict, unreacted grains were observed (see Figure 2). The lack of re-equilibration in the 93 μm experiments led to the decision to regrind the WR powder to a finer fraction and rerun the experiments. This produced a single population of olivine and homogenized pre-existing crystalline material. Since olivine is the only saturating silicate phase, we feel that the experiments are close to a state of equilibrium. However, the experimental liquids have undergone quench modification and corrections need to be made for that.

At the temperature and pressure conditions of the runs, melting extents were small and thus equilibrium depends somewhat on the solid state diffusion in the saturating crystalline phases. The melt analyses are systematically depleted in MgO as shown by the olivine-melt Fe-Mg exchange coefficient if equilibrium is assumed. Values of 0.29-0.33 are indicative of equilibrium between olivine and melt, however, the values from our experiments range between 0.10 and 0.24. This is most likely due to the removal of MgO from the liquid due to the growth of quench phases along the margins of the crystalline silicate phases during termination of the experiment (Kring and McKay, 1984). Attempts to measure liquid compositions away from solid phases were unsuccessful as the melt pools were extremely small (Figure 3). Attempts to measure the glass composition with a smaller beam size did not improve the results.

A second line of evidence was used to evaluate equilibrium. The $D_{CaO}^{Oliv\text{-}Melt}$ values should not be affected by the growth of Mg-rich quench phases during experiment termination. The $D_{CaO}^{Oliv\text{-}Melt}$ values for each experiment were calculated and compared to the equilibrium values predicted by Jurewicz and Watson (1988). Equilibrium values for the compositions of the experimentally produced olivine should be ~0.035. The range of values calculated from our experiments is 0.057 to 0.027, with average values of 0.042. This is within 20% of the predicted equilibrium value of Jurewicz and Watson (1988) indicating the assumption of crystal/melt equilibrium is not out of the realm of possibility (Jurewicz *et al*, 1993).

If we assume equilibrium was achieved and that the low MgO liquid contents are directly attributable to quench phases, then the liquid compositions can be recalculated to compensate for the MgO loss. Recalculation of the liquid composition was accomplished by increasing the MgO content of the liquid until the olivine-melt $K_d^{Fe\text{-}Mg}$ equaled 0.33. The liquid compositions were then renormalized and are reported in Table 2.

Experimental Results

The experimental run conditions and products are reported in Table 1. Six reconnaissance experiments were conducted to evaluate the melting behavior of CV3 material at pressures, temperatures and oxygen fugacities appropriate for a small, carbon-bearing planetesimal. Experimental temperatures spanned the range 1180 to 1260°C and pressures of 5.5 to 12 MPa. The first three experiments listed in Table 1 were performed with Allende WR powder that was crushed and sieved to 93 μm. Those experiments

were saturated with olivine and liquid, however it was apparent that unreacted crystalline materials present in the starting material were also present. This was most evident in the 1200°C; 11 MPa experiment where it appears that no melting and/or homogenization took place (Figure 4). Pre-existing phases were also observed in higher temp experiments as is demonstrated by the two populations of olivine observed in AM-2. One population is assumed to have grown during the experiment with Fo_{78} and $K_d^{Fe\text{-}Mg}$ value of 0.11. A pre-existing population of almost pure forsterite (Fo_{95}) with a Fe-Mg exchange coefficient value indicating severe disequilibrium is also observed (see Fig. 2 for example). These magnesian olivines are presumably unreacted olivine from chondrules in Allende. The remaining three experiments we report were performed with powder that was subsequently crushed and sieved to <54 μm in an effort to achieve homogenization.

The three experiments performed with the smaller size fraction powder were performed at 1200 and 1180°C and at pressures of 10, 9 and 5.5 MPa (Table 1). In all three experiments liquid, olivine and metal phases were observed. No attempt was made to analyze the metal phases. Analytical efforts were focused on the melt and olivine compositions. Olivine Fo contents range from 63 to 68. The Fe-Mg exchange coefficients are low and are most likely due to modification of the liquid composition by quench growth.

The experimentally produced liquids are extremely FeO rich and have most likely suffered the effects of quench crystallization as discussed previously. MgO was added back to the liquid compositions to obtain reasonable olivine-melt Fe-Mg exchange coefficients (see Approach to Equilibrium section above). The reconstituted liquid

compositions are shown in Table 2. At 10 MPa, 1200°C the liquid contains 2.7 wt% Na_2O and 1.28 wt% P_2O_5. The Na_2O and P_2O_5 contents at 9 MPa, 1180°C are very similar at 2.8 and 1.3 wt%, respectively. As pressure decreases, so do the Na_2O and P_2O_5 contents – 2.0 and 0.9 wt% at 5.5 MPa, 1200°C (Figure 5).

The recalculated MgO added liquid compositions are plotted in the Olivine-Clinopyroxene-Anorthite ternary diagram in Figure 6 and in the Olivine-Quartz-Anorthite ternary in Figure 7. The experimental liquids of Jurewicz *et al* (1993) are also plotted for comparison. The 5.5 MPa, 1200°C experiment plots in the olivine primary phase volume in the vicinity of the 0.1 MPa, 1200°C experiment of Jurewicz *et al* (1993) in both diagrams. However, the two higher pressure experiments plot much nearer to the plagioclase primary phase volume in Ol-Cpx-An space and in the spinel primary phase volume in the Ol-Qtz-An diagram.

Discussion

The experimental liquid compositions change significantly with pressure, moving towards plagioclase saturation with increasing pressure. Volatile element contents (i.e. Na and P) are enriched in the melt at elevated pressures. This effect is probably due to two competing factors. The first is the pressure dependence of the vaporization reaction equilibrium constant and the second is the loss of the volatile species to the gas phase in large volumes of gas at low pressures. One can write an expression for equilibrium between volatile components in the liquid (e.g. Na_2O and P_2O_5) and their dissociated species in a coexisting gas phase. An example of such a reaction for Na_2O is:

$$Na_2O^{liquid} <-> Na^{gas} + 1/2O_2 \ (1)$$

A similar reaction can be written for P_2O_5 and its dissociated species. In 0.1 MPa gas mixing experiments and in the low gas partial pressure of the solar nebula, loss of Na from the melt to the enclosing gas would be expected. This process was recognized by Tormey *et al* (1987) who characterized the loss of Na_2O and showed that the Na loss problem increased as oxygen fugacity of the gas mixture decreased. The Jurewicz *et al* (1993) experiments were conducted at 0.1 MPa and low fO_2 and experienced significant loss of Na_2O and P_2O_5 during the course of the experiments. In this respect the Jurewicz *et al* (1993) experiments may resemble the processes that would occur in the near vacuum conditions that were present during chondrule formation. As pressure increases, the volume change of reaction (1) would drive the equilibrium to the condensed (Na_2O in liquid) side of the reaction, allowing the volatile species to remain in the liquid phase. Our experiments at modest pressures demonstrate the vapor pressure of Na in gas is very low by the time pressure has reached 9 MPa. Thus the moderate pressure of ~10 MPa is enough to retain most of the Na_2O and P_2O_5 in the melt generated from the Allende material. Partial melting at pressures of just 5 MPa generates melts that have somewhat lower Na_2O and P_2O_5 contents of 1.97 and 0.92 wt%. At this pressure the lower values for these elements is probably a result of the loss of Na and P to the gas phase to establish an equilibrium partial pressure. Experiments at 9 and 10 MPa essentially retain all of the Na and are enriched in plagiophile elements Al, Ca and Na relative to the 5.5 MPa experiment (see Table 1).

The increase in Na content of the melt is a major control on the location of the melt in the Ol-Cpx-An ternary. As pressure increases, the melt compositions migrate towards the

olivine-plagioclase boundary (Figure 6). The reason for this is that each mole of Na_2O in the liquid is associated with one mole of Al_2O_3 and 6 moles of SiO_2. Thus, a small addition of Na_2O in the liquid results in a big increase in plagioclase content and decrease in silica in the melt. The 5.5 MPa experiment plots in the same position as the Jurewicz *et al* (1993) IW-1 experiment at the same temperature.

The melt compositions also show a pressure effect in the Ol-Qtz-An ternary diagram (Figure 7). The 9 and 10 MPa experiments plot in the spinel stability field, near the plagioclase-spinel boundary. The 5.5 MPa experimental liquid plots in the olivine primary phase volume. The IW-1 experimental liquids of Jurewizc *et al* (1993) also plot in the olivine primary phase volume but towards more pyroxene rich compositions. The IW+2 liquids plot at negative quartz values and are not shown.

The fact that the composition of high pressure (>10 MPa) partial melts of Allende are closer to plagioclase saturation may have important implications for the residue composition and may tie into and help explain the petrogenesis of other meteorite types. We explore this in the following sections.

Application to Ureilite petrogensis

Ureilites are primitive achondrites that are hypothesized to be the residues of partial melting (Boynton *et al*, 1976; Scott *et al*, 1993; Wasson *et al*, 1976). Experimental data constrain their depths of origin to be between 25 and 7.5 MPa (Singletary and Grove, 2003; Walker and Grove, 1993). Ureilites are composed of coarse grained olivine and pyroxene that display equilibrated textures and have equilibrated mineral chemistries. They also possess many primitive geochemical characteristics that imply they have

undergone very little processing which stands in stark contrast to the textures, mineralogy and chemistry.

A key constraint in all models of ureilite petrogenesis is the presence of superchondritic Ca/Al ratios and the depletion of plagiophile elements (Na, Al, K, and Ca) relative to chondrites (Boynton *et al*, 1976) Based on these geochemical data, many authors have argued that the ureilite source material must have had a plagioclase component removed from it at some point (e.g. Goodrich *et al*, 1987). Melting models of chondritic source materials can not produce ureilite residues. The models point to the ureilite parent source as requiring superchondritic Ca/Al ratios as well a depletion of the plagiophile elements (Goodrich, 1999). Both lines of evidence have been interpreted to indicate extensive and prolonged episodes of igneous processing of the ureilite parent material.

The results of the experiments conducted in this study indicate that CV3 material partially melted at ~10 MPa will produce melts that are very enriched in plagiophile elements (Na, Ca and Al). The moderate pressures inside a small parent body allow volatile elements, normally lost during low pressure melting (i.e. Na_2O and P_2O_5), to remain in the melt and play a significant role in controlling the compositions of the melt. Removal of a melt such as this will leave behind a residue depleted in plagiophile elements. Since the melts are enriched in Na_2O, normative plagioclase compositions will most likely be albite rich.

Polymict ureilites are a small subset of the ureilite population and are described as fragmental breccias (Mittlefehldt *et al*, 1998). They commonly contain 2 modal % feldspars that span the range of An_0 to An_{100}. Also observed in the polymict ureilites are

clasts of feldspathic glass (An_{50}) that contain crystals of olivine, low-Ca pyroxene and phosphate (Prinz *et al*, 1988). The elevated Na_2O and P_2O_5 contents of the high pressure experimental liquid makes a link between high pressure partial melting of CV3 material and ureilite petrogenesis tantalizing and plausible.

Application to Larger Planetary Bodies

Models of planetary accretion typically involve a nebular cloud of dust collapsing into a star, with the remaining material forming planets, asteroids and comets orbiting about the star. Formation of the planetary bodies occurs as bodies grow from meter to kilometer and finally thousand kilometer sized bodies through impacts (Wetherill and Stewart, 1989). The existence of bodies on the order of tens to hundreds of kilometers has been inferred from models and such bodies are observed in the asteroid belt today. It is therefore reasonable to assume that early during solar system formation, when abundant heat-producing, short-lived radioactive isotopes (i.e. ^{26}Al) were actively decaying, igneous processing would have been occurring at pressures investigated in this study (Taylor and Norman, 1990). If partial melting is occurring in these bodies, the obvious question is how can that affect the residues, and subsequently, the geochemical characteristics of larger bodies assembled from the smaller, processed bodies?

Igneous processing occurring at pressures found in the small bodies will smelt and produce melts enriched in volatiles. Smelting will occur at low pressures if fO_2 is below IW (Singletary and Grove, 2003; Walker and Grove, 1993). The reconnaissance experiments conducted here are used to infer the behavior of the bulk composition of a

body of primitive composition that is undergoing low-degrees of partial melting and the effects on larger bodies assembled from the processed residues.

A major goal of planetary science has been to link primitive materials to the larger bodies so as to estimate the bulk composition of the larger bodies. Ringwood (1966a) was one of the first to examine the feasibility and implications of assembling a planetary sized body from material with primitive compositions. Ringwood began with a CI bulk compositions and performed a series of calculations to simulate differentiation of an Earth sized body with a CI bulk composition. After differentiation of a metallic core and several assumptions involving the behavior of H_2O, sulfur and oxygen, a model silicate mantle composition was calculated from the residuum that indicated our present mantle may be silica undersaturated. The problem of mantle silica undersaturation vexes us to this day (Jagoutz *et al*, 1979; Hart and Zindler, 1988).

Further work also indicated the mantle is enriched in platinum group elements (PGEs) compared to chondritic material (Ringwood, 1966b). The PGE overabundance has been attributed by many workers to the addition of a late veneer of chondritic material after core segregation (Drake, 2000). Previously ideas suggested the overabundance was due to a change in the composition of the material accreting to the Earth (Wanke, 1981). Others have suggested the either high pressure or compositional controls on the partitioning of PGE during a magma ocean phase may also be responsible (e.g. Murthy, 1991; Jana and Walker, 1997)

In Table 3, we reproduce the Ringwood (1966a) calculation and explore the effects of varying the bulk composition by removal of melts generated at moderate pressures. We

use updated meteorite bulk compositions from Jarosewich (1990). The other difference in our calculations is that in the original work, Ringwood removed silica from the mantle to bring the mantle/core mass ratio into line with geophysically determined mantle/core mass constraints and to bring the mantle silica contents into agreement with his favored estimate of mantle composition (i.e. pyrolite; Ringwood, 1966a). Here we do not remove silica to the core and our model mantle SiO_2 contents are higher than in the original work. Recent high pressure experiments suggest that silica is not the light element in the core (Agee *et al*, 1995). However, it is certain some light element must be present in the Fe,Ni core from size and density constraints. We assume sulfur is partitioned into the core for consistency in the calculations and provide an estimate of how much sulfur is needed in each model to obtain the correct core density (Table 3).

Table 3b displays the results of the calculation using the CV3 bulk composition of Jarosewich (1990). To a first order, it does not provide as good a match to the mantle/core mass balance constraints of 69/31 as does the CI bulk composition. However, the major element oxides match to the model pyrolite composition of McDonough and Sun (1994) within 5% with the exception of SiO_2, MgO and Na_2O. The SiO_2 and Na_2O contents are high with lower MgO contents (by ~9%).

Tables 3c, d, and e list the results of the calculation removing 1, 5 and 10 wt% melt from the bulk composition. The melt composition is taken from the 1180°C; 9 MPa experiment and is meant to model the effects of melt removal and subsequent geochemical make up of a body assembled from the residue. As the melt fraction is removed from the CV3 bulk composition, the mantle/core mass value decreases from 78.8/21.2 to 77.9/22.1.

The renormalized silicate whole mantle compositions of each model run are displayed in Table 4 and are compared to the model pyrolite composition of McDonough and Sun (1994). While the SiO_2 contents of the residues decreases with melt removal, they do not descend to the levels of the model pyrolite. There is good agreement with many of the major element oxides, core/mantle mass issues not withstanding.

The removal of low degrees of partial melt from small parent bodies changes the bulk composition of the parent body. In a planetismal that is undergoing smelting and melting, these melts are lost to space, either by explosive volcanism (Warren and Kallemeyn, 1992; Keil and Wilson, 1993; Wilson and Keil, 1996)) or are removed with other material via impact gardening. The melt fraction constitutes a relatively small portion by mass of the original processed material and may be very difficult to identify in our collections. Larger bodies that are formed by coalescence of these smaller processed bodies therefore will not have a bulk composition equal to that of the primitive starting material.

Table 3f lists the original calculation but this time using the CM2 bulk composition of Jarosewich (1990). It is interesting to note that the mantle/core mass value is 68.6/31.4, very near that predicted for the Earth. However the corresponding renormalized mantle composition has SiO_2 contents higher than any of the other calculated compositions and is more depleted in MgO than any other composition produced here. FeO, CaO and Al_2O_3 are all within 12wt% of the McDonough and Sun (1994) pyrolite composition.

Conclusions

Partial melting experiments of the Allende CV3 meteorite indicate that at moderate pressures, melts are enriched in volatile elements (i.e. Na_2O) compared to melts generated at 0.1 MPa. The pressures investigated here are appropriate for bodies <200 km in diameter. Such bodies are present in the solar system and were most likely present during early solar system evolution. Igneous processes would have been initiated at such moderate pressures and the resulting residues and melts would have been affected as described here. The melting of CV3 compositions at 10 MPa could produce a residue that is depleted in plagiophile elements, possibly leading the parent material of the ureilites. The enriched melts may be preserved in the polymict ureilites.

While the results of this study are preliminary in nature, they indicate the geochemical signatures of the larger planets could have been affected by processes occurring on these small bodies. Subsequent larger bodies assembled from the smaller, processed bodies may show the effects of the early processing. If alkali and silica rich melts generated at low pressures are lost to space, then a silica undersaturated silicate portion is left behind. Jana and Walker (1997) demonstrated that silicate melt composition plays a strong role in the distribution of siderophile elements, with the siderophiles favoring ultramafic compositions. Its possible the alkalic nature of the melts is forcing siderophiles to remain in the residue, thereby enriching the small bodies in those elements and may be another mechanism for producing the observed terrestrial PGE overabundances. Re-examining Ringwood's original calculations, it seems that maybe CM2 chondrites provide a better match for the masses of core and mantle but not to mantle composition. The use of a CM2 composition does not solve the problem of mantle siderophile over abundance

however. Perhaps a planetesimal residue modified by low pressure melting could resolve this discrepancy.

References

Agee C.B. (1990) A new look at differentiation of the Earth from melting experiments on the Allende meteorite. *Nature* **346**, 834-837.

Agee C.B. (1993) High-pressure melting of carbonaceous chondrite. *J. Geophys. Res.* **98**, 5419-5426.

Agee C.B., Li J., Shannon M.C. and Circone S. (1995) Pressure-temperature phase diagram for the Allende meteorite. *J. Geophy. Res.* **100**, 17,725-17,740.

Anders E. and Grevesse N. (1989) Abundances of the elements: Meteoritic and solar. *Geochim. Cosmochim. Acta* **53**, 197-224.

Armstrong J.T. (1995) Citzaf - a package of correction programs for the quantitative electron microbeam x-ray-analysis of thick polished materials, thin-films, and particles. *Microbeam Analysis* **4**, 177-200.

Boynton W. V., Starzyk P. M. and Schmitt R. A. (1976) Chemical evidence for genesis of ureilites, achondrite chassigny and nakhlites. *Geochim. Cosmochim. Acta* **40**, 1439-1447.

Drake M.J. (2000) Acccretion and primary differentiation of the Earth: A personal journey. *Geochim. Cosmochim Acta* **64**, 2363-2370.

Goodrich C.A., Jones J.H. and Berkley J.L. (1987) Origin and evolution of the ureilite parent magma: Multi-stage igneous activity on a large parent body. *Geochim. Cosmochim. Acta* **51**, 2255-2273.

Goodrich C.A. (1999) Are ureilites residues from partial melting of chondritic material? The answer from MAGPOX. *Met. & Planet. Sci.* **34**, 109-119.

Jana D. and Walker D (1997) The influence of silicate melt composition on distribution of siderophile elements among metal and silicate liquids. *Earth Planet. Sci. Lett.* **150**, 463-472.

Jarosewich E. (1990) Chemical analyses of meteorites: A compilation of stony and iron meteorite analyses. *Meteoritics* **25**, 323-337.

Jurewicz A.J.G. and Watson E.B. (1988) Cations in olivine, Part 1: Calcium partitioning and calcium-magnesium distribution between olivines and coexisting melts, with petrologic applications. *Contrib. Mineral. Petrol.* **99**, 176-185.

Jurewicz A.J.G., Mittlefehldt D.W. and Jones J.H. (1993) Experimental partial melting of the Allende (CV) and Murchison (CM) chondrites and the origin of asteroidal basalts. *Geochim. Cosmochim. Acta* **57**, 2123-2139.

Keil K. and Wilson L. (1993) Explosive volcanism and the composition of cores of differentiated asteroids. *Earth Plant. Sci. Lett.* **117**, 111-124.

Kring D.A. and McKay G.A. (1984) Chemical gradients in glass adjacent to olivine in experimental charges and Apollo 15 green glass vitrophyres. *Lunar Planet. Sci. Conf.* **XV**, 461-462 (abstr).

Mittlefehldt D.W., McCoy T.J., Goodrich C.A. and Kracher A. (1998) Non-chondritic meteorites from asteroidal bodies. In *Planetary Materials* (ed. J. Papike), **36**.

Murthy V.R. (1991) Early differentiation of the Earth and the problem of mantle siderophile elements: A new approach. *Science* **253**, 303-306.

Prinz M. Weisberg M.K. and Nehru C.E. (1988) Feldspathic components in polymict ureilites. *Lunar. Planet. Sci. Conf.* **IXX**, 947-948.

Ringwood A.E. (1966a) The chemical composition and origin of the Earth. *In* Advances in Earth Sciences. P.M. Hurley (ed) M.I.T. Press, Cambridge, MA. 287-356.

Ringwood A.E. (1966b) Chemical evolution of the terrestrial planets. *Geochim. Cosmochim. Acta* **30**, 41-104.

Scott E.R.D., Taylor G.J. and Keil K. (1993) Origin of ureilite meteorites and implications for planetary accretion. *Geophys. Res. Lett.* **20**, 415-418.

Seitz M.G. and Kushiro I. (1974) Melting relations of the Allende meteorite. *Science* **183**, 954-957.

Singletary S.J. and Grove T.L. (2003) Early petrologic processes on the ureilite parent body. *Met. & Planet. Sci.* **38**, 95-108.

Taylor S.R. and Norman M.D. (1990) Accretion of differentiated planetesimals to the Earth. *In* Origin of the Earth. Eds. H.E. Newsom and J.H. Jones, Oxford Univ. Press, New York, pp. 29-44.

Tormey D.R., Grove T.L. and Bryan W.B. (1987) Experimental petrology of normal MORB near the Kane Fracture Zone: 22 – 25, mid-Atlantic ridge. *Contrib. Mineral. Petrol.* **96**, 121-139.

Walker D. and Grove T. (1993) Ureilite smelting. *Meteoritics* **28**, 629-636.

Wanke H. (1981) Constitution of terrestrial planets. *Phil. Trans. R. Soc. Lond.* **303**, 287-302.

Warren P.H. and Kallemeyn G.W. (1992) Explosive volcanism and the graphite oxygen fugacity buffer on the parent asteroid(s) of the ureilite meteorites. *Icarus* **100**, 110-126.

Wasson J.T., Chou C.L., Bild R.W. and Baedecker P.A. (1976) Classification of and elemental fractionation among Ureilites. *Geochim. Cosmochim. Acta* **40**, 1449-1458.

Wetherill G.W. and Stewart G.R. (1989) Accumulation of a swarm of small planetesmals, *Icarus* **77**, 330-357.

Wilson L. and Keil K. (1996) Clast sizes of ejecta from explosive eruptions on asteroids: Implications for the fate of the basaltic products of differentiation. *Earth Planet. Sci. Lett.* **140**, 191-200.

Figure Captions

Figure 1. Pressure-temperature grid showing the phase relations of the Allende CV3 chondrite up to pressures of 27 GPa and temperatures in excess of 2000°C.

Figure 2. Back scattered electron image of experiment AM-5 displaying the presence of relict minerals that did not homogenize over the course of the experiment.

Figure 3. Back scattered electron image of experiment AM-6 showing the nature of the experimental melts. Melt pockets were small, generally on the order of 10's of microns. Light areas around the crystalline phases are most likely quench crystals that grew during experiment termination. These have a significant effect on melt composition when melt fractions are small.

Figure 4. Back scattered electron image of experiment AM-3. This experiment was performed with the 93 μm sized fraction. The experimental charge shows no effects of homogenization and prompted a regrinding of the Allende WR powder to a smaller grain size.

Figure 5. Na_2O and P_2O_5 wt% of the experimental liquids plotted against run pressure. There is an overall trend of decreasing wt% with decreasing pressure such that the Na_2O and P_2O_5 approach the 0.1 MPa liquid values of Jurewicz *et al* (1993).

Figure 6. Olivine-Clinopyroxene-Anorthite ternary diagram. Experimental liquids from this study and the Jurewicz *et al* (1993) study are plotted. The increase in pressure serves to drive the melts to more plagioclase rich compositions at the same temperature.

Figure 7. Olivine-Quartz-Anorthite ternary diagram. Data points as in Figure 6. The IW+2 experimental liquids of Jurewicz *et al* (1993) plot at negative quartz values

in this system and have been left out. In this system, higher pressures move the melts into the spinel primary phase volume.

Figure 1.

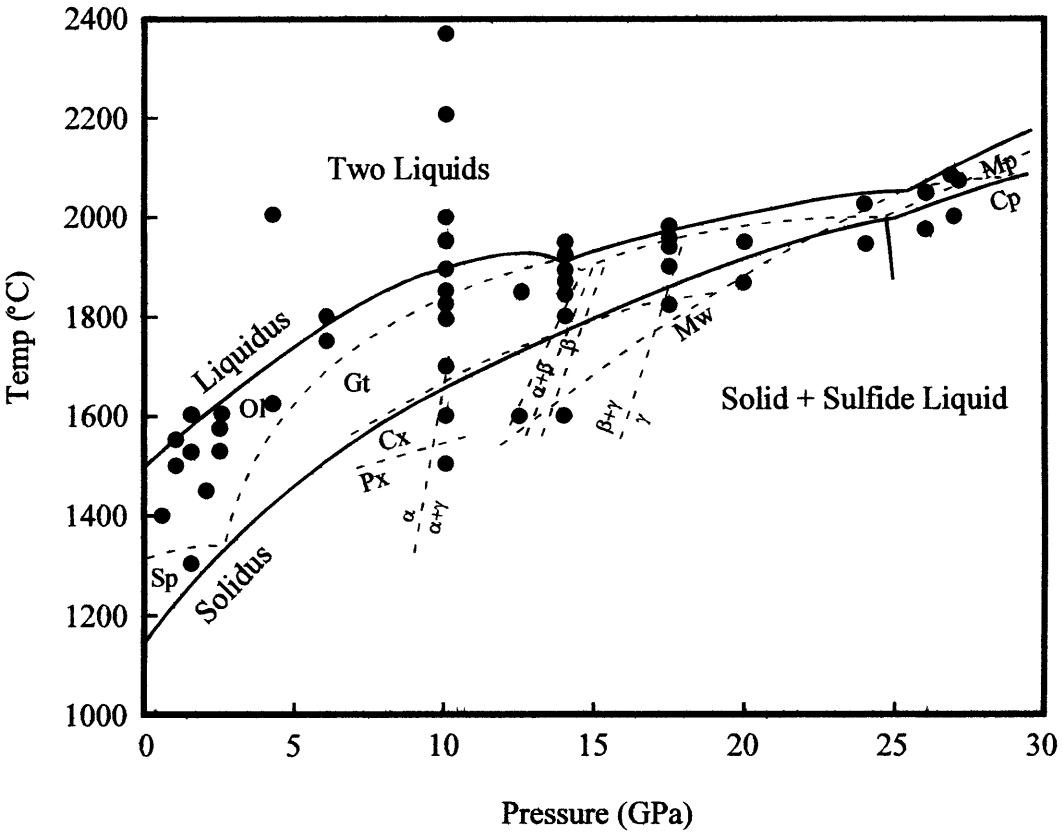
2400
2200
2000
1800
1600
1400
1200
1000
Temp (°C)
0
5
10
15
20
25
30
Pressure (GPa)
Two Liquids
Liquidus
Solidus
Gt
Ol
Cx
Px
Sp
α
α+γ
α+β
β
β+γ
γ
Mw
Mp
Cp
Solid + Sulfide Liquid

Figure 2.

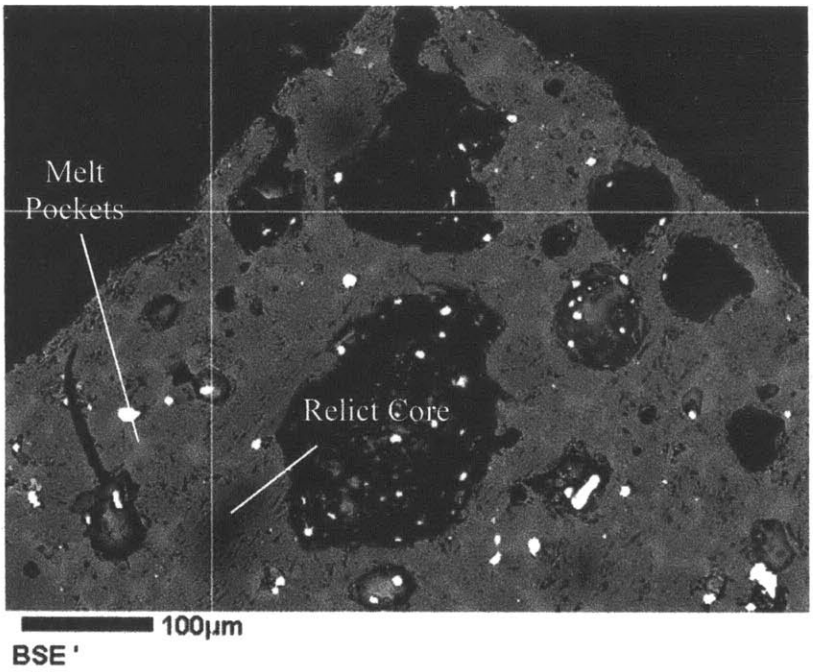

Figure 3.

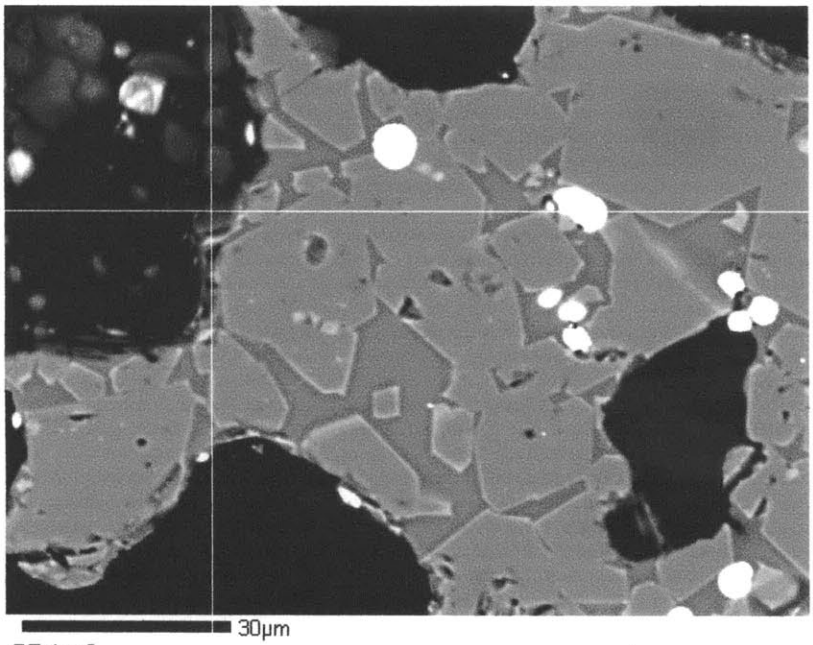

Figure 4.

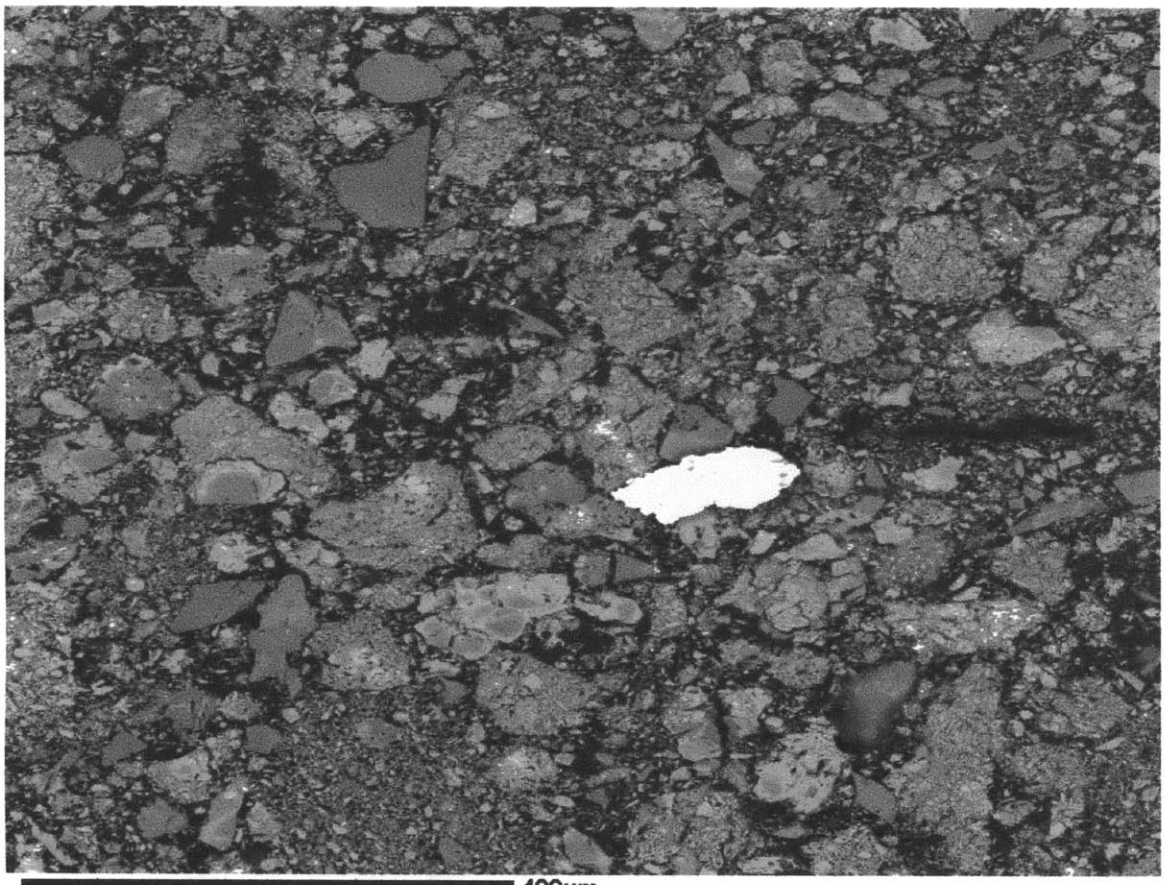

Figure 5.

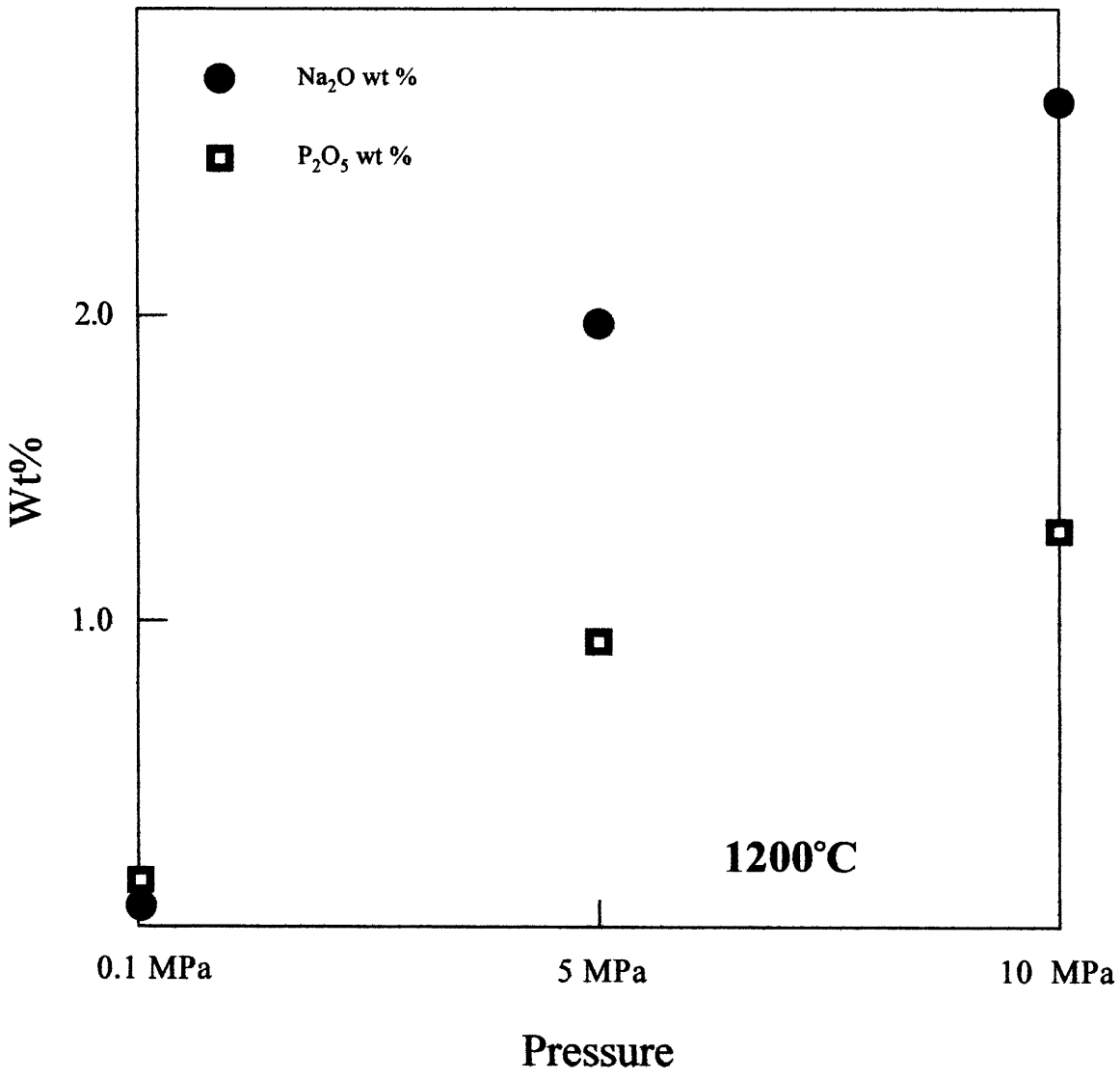

Figure 6.

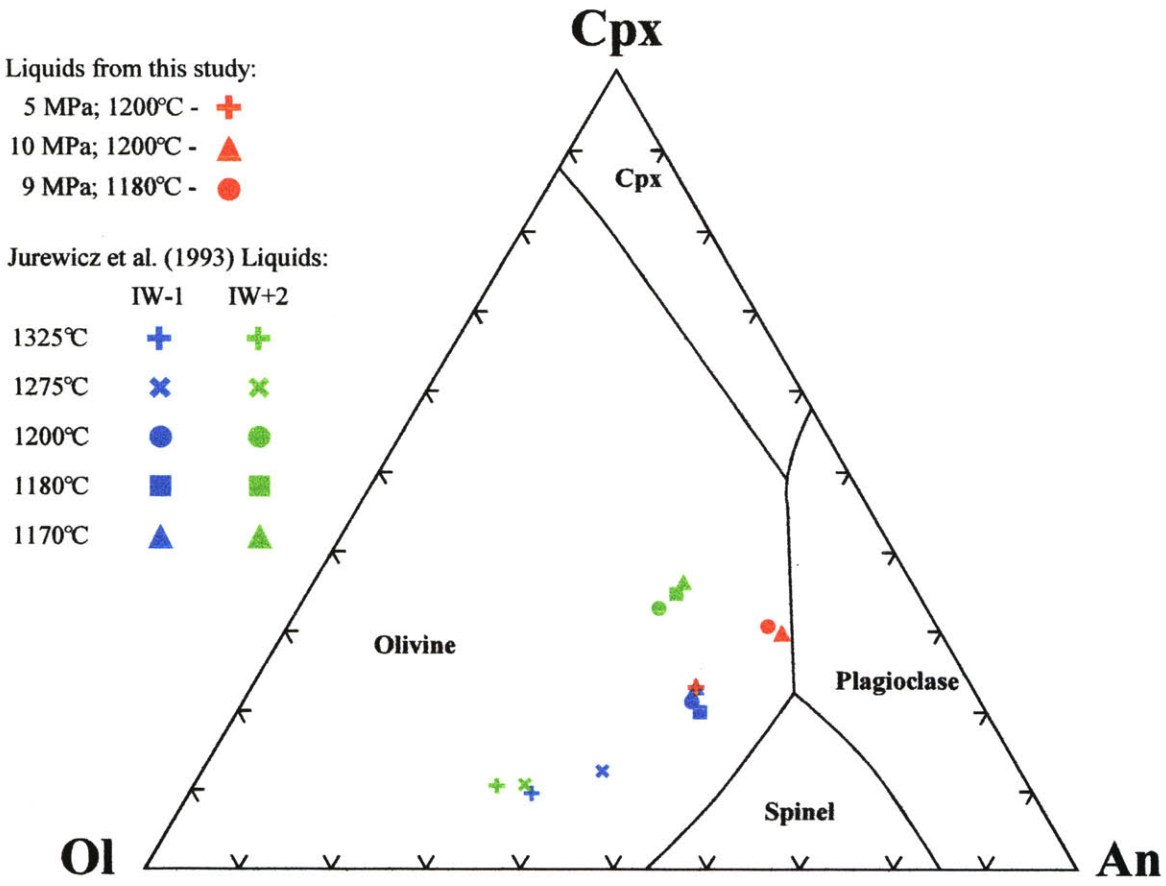
Cpx
Liquids from this study:
5 MPa; 1200°C -
10 MPa; 1200°C -
9 MPa; 1180°C -
Jurewicz et al. (1993) Liquids:
IW-1
IW+2
1325°C
1275°C
1200°C
1180°C
1170°C
Cpx
Olivine
Plagioclase
Spinel
Ol
An

Figure 7.

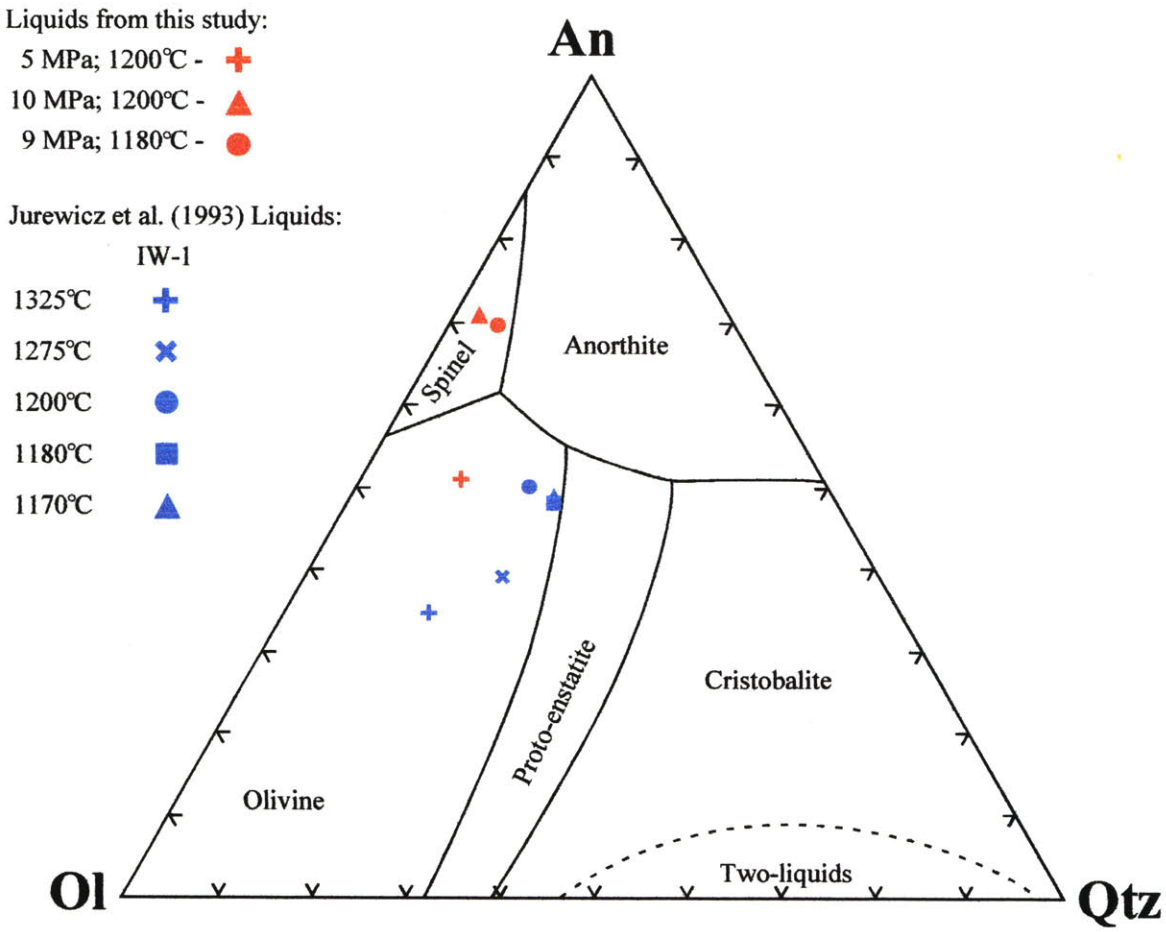
Liquids from this study:
5 MPa; 1200°C -
10 MPa; 1200°C -
9 MPa; 1180°C -
Jurewicz et al. (1993) Liquids:
IW-1
1325°C
1275°C
1200°C
1180°C
1170°C
An
Spinel
Anorthite
Proto-enstatite
Cristobalite
Olivine
Two-liquids
Ol
Qtz

Table 1. Experimental run conditions and products.

Exp #	t hrs	P MPa	T C	Phase (#analysis)	SiO_2	TiO_2	Al_2O_3	Cr_2O_3	FeO	MnO	MgO	CaO	Na_2O	K_2O	P_2O_5	S	Total	mg#	$K_d^{ol/liq}$	D_{CaO}
AM-2	16	12	1260	Glass (10)	51(1)[a]	0.6(1)	12.7(6)	0.43(7)	17(2)	0.18(4)	3.8(6)	11.6(5)	1.7(2)	0.15(3)	0.4(1)	0.03(2)	99.6	29.1		0.023
				Olivine (23)	38.0(6)	0.02(1)	-[b]	0.5(1)	19.9(7)	0.24(5)	40.8(7)	0.27(5)	-	-	-	-	99.7	78.5	0.11	
				Olivine*(2)	41.4(7)	-	-	0.15(7)	5(3)	0.08(5)	52(3)	-	-	-	-	-	98.6	94.7	0.02	
AM-5	23	10	1230	Glass(17)	42.9(4)	0.6(1)	12.6(4)	0.25(5)	24.3(5)	0.19(4)	7.0(7)	10.6(3)	1.45(8)	0.10(3)	0.7(2)	0.20(9)	100.9	33.9		0.037
				Olivine(3)	37.1(2)	-	0.06(1)	0.25(1)	28.4(2)	0.22(1)	34.1(2)	0.39(1)	-	-	-	-	100.5	68.2	0.24	
AM-6	25	9	1180	Glass(9)	43.0(7)	0.82(7)	16.0(8)	0.07(2)	17(2)	0.14(4)	3(1)	16(1)	2.8(2)	0.17(1)	1.3(1)	0.15(4)	100.5	20		0.042
				Olivine(9)	35.9(3)	0.03(1)	-	0.12(3)	32.0(6)	0.18(2)	30.8(6)	0.7(1)	-	-	-	-	99.8	63.2	0.15	
AM-7	16	10	1200	Glass(12)	42.4(4)	0.81(5)	16.5(3)	0.10(4)	17.6(7)	0.13(2)	1.8(2)	15.8(3)	2.7(1)	0.21(1)	1.28(9)	0.17(3)	99.6	15.3		0.042
				Olivine(11)	35.8(3)	-	0.10(7)	0.15(3)	31.5(5)	0.17(1)	31.2(5)	0.67(8)	-	-	-	-	99.7	63.7	0.10	
AM-8	21.5	5.5	1200	Glass(16)	44.7(3)	0.61(6)	14.0(3)	0.24(3)	20.3(5)	0.19(3)	5.5(3)	12.0(2)	2.0(1)	0.17(1)	0.9(1)	0.18(3)	100.8	32.5	0.22	0.042
				Olivine(13)	36.6(4)	-	-	0.3(2)	28.1(2)	0.24(2)	34.8(3)	0.51(5)	-	-	-	-	100.6	68.8		

* Second population of olivine most likely relict cores.

[a] Number in parenthesis is one sigma standard deviation in terms of least units cited. Therefore, 38.7(3) should be read as 38.7 ± 0.3wt%

[b] Indicates element not analyzed of below detectability limit

Table 2. Reconstituted liquid compositions.

	10 MPa; 1200°C	9 MPa; 1180°C	5.5 MPa; 1200°C
SiO_2	41.00	42.03	43.24
TiO_2	0.79	0.80	0.59
Al_2O_3	16.00	15.64	13.50
Cr_2O_3	0.09	0.07	0.23
FeO	17.03	16.73	19.66
MnO	0.12	0.14	0.19
MgO	5.61	5.28	8.03
CaO	15.28	15.15	11.59
Na_2O	2.63	2.71	1.91
K_2O	0.20	0.17	0.17
P_2O_5	1.24	1.28	0.89
	99.99	100.00	100.00

Table 3 a.

Ringwoods original CI calculation

1[a]	wt %		2[b]	Moles	Moles after Core Formation		Mantle Wt% after Core Form.	Renorm.		Renorm. Mantle component wt %
H_2O	19.29	SiO_2	33.21	0.5527	0.5527	SiO_2	33.21	35.74		48.76
C	3.97	MgO	23.42	0.5810	0.5810	MgO	23.42	25.21		34.39
Org. Mat.	5.53	FeO	35.70	0.4968	0.0792	FeO	5.69	6.13		8.36
Na_2O	0.74	Al_2O_3	2.41	0.0236	0.0236	Al_2O_3	2.41	2.59		3.53
MgO	15.96	CaO	2.29	0.0408	0.0408	CaO	2.29	2.46		3.36
Al_2O_3	1.64	Na_2O	1.09	0.0175	0.0175	Na_2O	1.09	1.17		1.59
SiO_2	22.63	NiO	1.89	0.0253	0.0000			**73.29**	% mantle	**100.00**
P_2O_5	0.35		100.00	1.738	1.29		**Core wt%**			
K_2O	0.07					Fe	23.32	25.10		
CaO	1.56					Ni	1.49	1.61		
TiO_2	0.07						92.92	**26.71**	%core	
Cr2O3	0.34									
MnO	0.22	Moles of FeO to the core=>		0.4176			Mantle + Core=>	100.00		
FeO	10.42	Mantle Fe# after core=>		0.12	(held constant to match					**Core Density[c]**
FeS	16.73				the observed mantle					7.93 g/cm^3
CoO	0.06				data)					
NiO	1.29									**Wt% Sulfur required[d] to obtain core density**
										5.57%

Oxide wt%s used in calculation:
SiO2+MgO+FeO+Al2O3+CaO+Na2O+NiO= 68.15

[a] Meteorite bulk composition from Jarosewich (1990)

[b] Renormalization of oxides used in the actual calculation. Corresponds to column 2 of Ringwood (1966a).

[c] Density of core formed by just Fe,Ni metal segregation

[d] Assuming sulfur is the light element in the core, wt% of sulfur needed to bring the core density into the range suggested by moment of inertia calculations

Table 3b.

CV3

1[a]	wt %		2[b]	Moles	Moles after Core Formation
H_2O	1.04	SiO_2	36.49	0.6073	0.6073
C	0.54	MgO	26.41	0.6553	0.6553
Org. Mat.	0	FeO	29.44	0.4097	0.0894
Na_2O	0.41	Al_2O_3	3.51	0.0344	0.0344
MgO	24.62	CaO	2.82	0.0503	0.0503
Al_2O_3	3.27	Na_2O	0.44	0.0071	0.0071
SiO_2	34.01	NiO	0.89	0.0119	0.0000
P_2O_5	0.27		100.00	1.776	1.44
K_2O	0.04				
CaO	2.63				
TiO_2	0.31				
Cr2O3	0.51	Moles of metallic iron=>		0.03	
MnO	0.19	Moles of FeO to the core=>		0.3203	
FeO	23.62	Mantle Fe# after core=>		0.12	(held constant to match
FeS	4.59				the observed mantle
CoO	0.03				data)
NiO	0.83				
Fe(metal)	1.94				

Oxides used in calculation:

SiO_2+MgO+FeO+Al_2O_3+CaO+Na_2O+NiO= 93.21

	Mantle Wt% after Core Form.	Renorm.		Renorm. Mantle component wt %
SiO_2	36.49	38.54		47.95
MgO	26.41	27.90		34.71
FeO	6.42	6.78		8.44
Al_2O_3	3.51	3.71		4.61
CaO	2.82	2.98		3.71
Na_2O	0.44	0.46		0.58
		80.37	% mantle	**100.00**
	Core wt%			
Fe	17.89	18.89		
Ni	0.70	0.74		
	94.69	**19.63**	% core	
Mantle + Core=>		100.00		

Core Density[c]

7.91 g/cm^3

Wt% Sulfur required[d] to obtain core density

5.20%

Table 3c.

CV3 - 1% melt at 1180C; 10 MPa

1[a]	wt %		2[b]	Moles	Moles after Core Formation		Mantle Wt% after Core Form.	Renorm.		Renorm. Mantle component wt %
H_2O	1.05	SiO_2	36.56	0.6084	0.6084	SiO_2	36.56	37.82		47.99
C	0.54	MgO	26.67	0.6616	0.6616	MgO	26.67	27.59		35.01
Org. Mat.	0	FeO	29.60	0.4120	0.0902	FeO	6.48	6.71		8.51
Na_2O	0.38	Al_2O_3	3.37	0.0331	0.0331	Al_2O_3	3.37	3.49		4.43
MgO	24.68	CaO	2.69	0.0480	0.0480	CaO	2.69	2.78		3.53
Al_2O_3	3.12	Na_2O	0.41	0.0066	0.0066	Na_2O	0.41	0.42		0.54
SiO_2	33.83	NiO	0.70	0.0094	0.0000			**78.82**	% mantle	**100.00**
P_2O_5	0.25		100.00	1.779	1.45		**Core wt%**			
K_2O	0.04					Fe	19.92	20.61		
CaO	2.49					Ni	0.55	0.57		
TiO_2	0.3						96.65	**21.18**	% core	
Cr2O3	0.51	Moles of metallic iron=>		0.03						
MnO	0.19	Moles of FeO to the core=>		0.3217			Mantle + Core=>	100.00		
FeO	23.56	Mantle Fe# after core=>		0.12	(held constant to match					**Core Density[c]**
FeS	4.61				the observed mantle					7.90 g/cm^3
CoO	0.03				data)					
NiO	0.65									**Wt% Sulfur required[d] to obtain core density**
Fe(metal)	1.95									5.02%

Oxides used in calculation:

SiO_2+MgO+FeO+Al_2O_3+CaO+Na_2O+NiO= 92.54

Table 3d.

CV3 - 5% melt at 1180C; 10 MPa

1[a]	wt %		2[b]	Moles	Moles after Core Formation
H_2O	1.04	SiO_2	36.29	0.6039	0.6039
C	0.54	MgO	27.61	0.6849	0.6849
Org. Mat.	0	FeO	29.96	0.4171	0.0934
Na_2O	0.28	Al_2O_3	2.82	0.0276	0.0276
MgO	25.48	CaO	2.12	0.0379	0.0379
Al_2O_3	2.6	Na_2O	0.30	0.0049	0.0049
SiO_2	33.49	NiO	0.90	0.0120	0.0000
P_2O_5	0.2		100.00	1.788	1.45
K_2O	0.03				
CaO	1.96				
TiO_2	0.28				
Cr2O3	0.53	Moles of metallic iron=>		0.03	
MnO	0.19	Moles of FeO to the core=>		0.3236	
FeO	23.84	Mantle Fe# after core=>		0.12	(held constant to match
FeS	4.59				the observed mantle
CoO	0.03				data)
NiO	0.83				
Fe(metal)	1.94				

Oxides used in calculation:

SiO_2+MgO+FeO+Al_2O_3+CaO+Na_2O+NiO= 92.30

	Mantle Wt% after Core Form.	Renorm.		Renorm. Mantle component wt %
SiO_2	36.29	37.57		47.84
MgO	27.61	28.59		36.40
FeO	6.71	6.95		8.85
Al_2O_3	2.82	2.92		3.71
CaO	2.12	2.20		2.80
Na_2O	0.30	0.31		0.40
		78.54	% mantle	**100.00**
	Core wt%			
Fe	20.01	20.72		
Ni	0.71	0.73		
	96.57	**21.46**	% core	
	Mantle + Core=>	100.00		

Core Density[c]

7.91 g/cm^3

Wt% Sulfur required[d] to obtain core density

5.14%

Table 3e.

CV3 - 10% melt at 1180C; 10 MPa

1[a]	wt %		2[b]	Moles	Moles after Core Formation
H_2O	1.16	SiO_2	35.88	0.5972	0.5972
C	0.54	MgO	28.89	0.7166	0.7166
Org. Mat.	0	FeO	30.91	0.4302	0.0977
Na_2O	0.15	Al_2O_3	2.04	0.0200	0.0200
MgO	26.59	CaO	1.34	0.0238	0.0238
Al_2O_3	1.88	Na_2O	0.16	0.0026	0.0026
SiO_2	33.03	NiO	0.78	0.0105	0.0000
P_2O_5	0.15		100.00	1.801	1.46
K_2O	0.03				
CaO	1.23				
TiO_2	0.25				
Cr2O3	0.53	Moles of metallic iron=>		0.04	
MnO	0.19	Moles of FeO to the core=>		0.3325	
FeO	24.24	Mantle Fe# after core=>		0.12	(held constant to match
FeS	5.07				the observed mantle
CoO	0.03				data)
NiO	0.72				
Fe(metal)	2.15				

Oxides used in calculation:
SiO2+MgO+FeO+Al2O3+CaO+Na2O+NiO= 92.05

	Mantle Wt% after Core Form.	Renorm.		Renorm. Mantle component wt %
SiO_2	35.88	37.12		47.63
MgO	28.89	29.88		38.34
FeO	7.02	7.26		9.32
Al_2O_3	2.04	2.11		2.71
CaO	1.34	1.38		1.77
Na_2O	0.16	0.17		0.22
		77.93	% mantle	**100.00**
	Core wt%			
Fe	20.72	21.43		
Ni	0.62	0.64		
	96.67	**22.07**	% core	
	Mantle + Core=>	100.00		

Core Density[c]
7.90 g/cm^3

Wt% Sulfur required[d] to obtain core density
5.05%

Table 3f.

CM2

1[a]	wt %		2[b]	Moles	Moles after Core Formation		Mantle Wt% after Core Form.	Renorm.		Renorm. Mantle component wt %
H_2O	11.94	SiO_2	31.84	0.5299	0.5299	SiO_2	31.84	34.68		50.46
C	1.72	MgO	20.96	0.5201	0.5201	MgO	20.96	22.84		33.23
Org. Mat.	0	FeO	40.33	0.5614	0.0709	FeO	5.10	5.55		8.08
Na_2O	0.45	Al_2O_3	2.69	0.0264	0.0264	Al_2O_3	2.69	2.93		4.27
MgO	18.45	CaO	1.99	0.0355	0.0355	CaO	1.99	2.17		3.15
Al_2O_3	2.37	Na_2O	0.51	0.0083	0.0083	Na_2O	0.51	0.56		0.81
SiO_2	28.02	NiO	1.67	0.0224	0.0000			**68.73**	% mantle	**100.00**
P_2O_5	0.23		100.00	1.704	1.19		**Core wt%**			
K_2O	0.05					Fe	27.39	29.84		
CaO	1.75					Ni	1.32	1.42		
TiO_2	0.12						91.80	**31.25**	% core	
Cr2O3	0.42	Moles of metallic iron=>		0.00						
MnO	0.23	Moles of FeO to the core=>		0.4904			Mantle + Core=>	99.98		
FeO	30	Mantle Fe# after core=>		0.12	(held constant to match					**Core Density[c]**
FeS	6.61				the observed mantle					7.92 g/cm^3
CoO	0.27				data)					
NiO	1.47									**Wt% Sulfur required[d] to obtain core density**
Fe(metal)	0.12									5.32%

Oxides used in calculation:

SiO_2+MgO+FeO+Al_2O_3+CaO+Na_2O+NiO= 88.00

Table 4. Model mantle compositions

	CI	CV3	CV3-1% melt	CV3-5% melt	CV3-10% melt	CM2	Pyrolite*
SiO_2	48.76	47.95	47.99	47.84	47.63	50.46	45.36
MgO	34.39	34.71	35.01	36.40	38.34	33.23	38.10
FeO	8.36	8.44	8.51	8.85	9.32	8.08	8.11
Al_2O_3	3.53	4.61	4.43	3.71	2.71	4.27	4.49
CaO	3.36	3.71	3.53	2.80	1.77	3.15	3.58
Na_2O	1.59	0.58	0.54	0.40	0.22	0.81	0.36
	100.0	100.0	100.0	100.0	100.0	100.0	100.0

*Preferred pyrolite composition of McDonough and Sun (1994).

Chp. 4 Origin of lunar high-titanium ultramafic glasses: A hybridized source?

Abstract

Two new hypotheses for the origin of the lunar high-Ti ultramafic glasses are considered in this study. These new models are motivated by the results of experiments on a model hybridized lunar magma ocean cumulate composition. These models are also motivated by the failure of current models to adequately account for the processes that lead to the origin of these unique lunar ultramafic magmas. In the first model we propose that the observed compositional variability at the high-Ti end of the glass spectrum is created by melting of compositionally heterogeneous source materials produced during the late stages of magma ocean crystallization. The lunar hybridized source composition that we have investigated can produce the major element compositional characteristics of the Apollo 17 orange glass and is saturated with olivine and orthopyroxene as residual phases in the source. Models of high-Ti glass generation that include fractional crystallization and/or melting involving these two phases is an attractive possibility because all lunar ultramafic melts show evidence of high pressure multiple saturation with these phases. However, crystallization of these phases in the proportions indicated from high pressure experimental results will not produce the entire spectrum of high-Ti glasses. Perhaps the compositional variability is caused by heterogeneity in the phase proportions stored as late-stage cumulate residues. In the second model, low degree partial melts of the hybridized magma ocean source are segregated during partial melting and sink into and interact with underlying hotter olivine + orthopyroxene cumulates, giving rise to the compositional spectrum observed in the high-Ti ultramafic glasses. In this model, the Apollo 17 high-Ti orange glass is produced by the highest degree of melting of the hybridized source. Higher-Ti ultramafic glasses (e.g. Apollo 15 red and Apollo 14 black glasses) are produced by smaller degrees of melting of the hybridized source when olivine + orthopyroxene + clinopyroxene are still present as saturating phases.

Introduction

Volcanic lunar glasses collected during the Apollo missions vary widely in Ti content (0.26-16.4 wt%; Delano, 1986). Various scenarios have been proposed to explain the origin of the high-Ti glasses. The high Ti contents of the glasses are often attributed to remelting of late stage magma ocean cumulates rich in ilmenite (Anderson, 1971; Taylor and Jakes, 1974; Hubbard and Minear, 1975; Ringwood and Kesson, 1976; Hess, 1991, Snyder *et al*, 1992; Shearer and Papike, 1993, 1999; Hess and Parmentier, 1995; Wagner and Grove, 1997). Some models of high-Ti glass genesis call for the assimilation of late-stage cumulates by low-Ti magmas (Hubbard and Minear, 1975; Wagner and Grove, 1997). Melting of a

heterogeneous mantle source produced by total overturn of the cumulate pile has also been invoked as a method to produce the high-Ti glasses (Ringwood and Kesson, 1976; Hess and Parmentier, 1995). Each model for the production of the high-Ti glasses has different and distinct implications for the chemistry of the lunar mantle. A re-examination of the competing hypotheses for the origin of the high-Ti magmas (Elkins-Tanton *et al*, 2002) reviews the strengths and weaknesses of the various hypotheses. They suggest several tests to provide further insight into late stage magma ocean hybridization processes and the origin of ultramafic lunar glasses through remelting of a hybridized source. We present experimental results of melting a hybridized model magma ocean cumulate source region to place constraints on the origin of these unique lunar ultramafic melts.

Experimental studies of the high-Ti glasses indicate they were derived from olivine-orthopyroxene bearing sources. Experimentally determined multiple saturation points suggest the glasses were last in equilibrium with their sources over a range of depths in the lunar mantle from deep (480 km, 2.4 GPa, ~1460°C, Apollo 15 red, Delano, 1980) to relatively shallow (300 km, 1.5 GPa, 1430°C, Apollo 14 black, Wagner and Grove, 1997). The inferred depths lie within the range proposed for storage of magma ocean cumulates, but are deeper than the hypothesized late stage, Ti-rich magma ocean cumulates (70-100 km) (Snyder *et al*, 1992; Hess and Parmentier, 1995). Even though these glasses are characterized by elevated TiO_2 contents, ilmenite is not a liquidus phase for any of the high-Ti glasses. If ilmenite is present in the source region, then it must be exhausted by any melting process that leads to the origin of the lunar glasses.

Assimilation models for the petrogenesis of the high-Ti glasses were evaluated by Wagner and Grove (1997). They found that assimilation of late stage ilmenite bearing cumulates by

low Ti magmas can produce the lower TiO_2 glasses within the boundaries imposed by the thermal energy budget. However, the high TiO_2 glasses (Apollo 12, 14, 15 red and Apollo 14 black) are not as well modeled by assimilation processes. The experiments of Van Orman and Grove (2000) were designed to test the idea of remelting late-stage, ilmenite bearing magma-ocean cumulates as a mechanism to generate the high TiO_2 glasses. They found it was not possible to generate a partial melt of the late stage cumulates that would produce the characteristics of the high TiO_2 magmas (Van Orman and Grove, 2000). The inability to reproduce the high TiO_2 magmas by previous studies through assimilation and/or remelting of late stage cumulates suggests other processes maybe occurring.

We present new experimental data to evaluate the model of Ringwood and Kesson (1976) that suggests the high-Ti ultramafic glasses were generated by melting of a hybridized lunar mantle source. The hybrid source is a mixture of cumulates precipitated from the lunar magma ocean (see Table 1). The first component consists of a 50:50 mix of orthopyroxene and olivine with mg# 87. This component is from deep (~400km) within the magma ocean cumulate pile and is the inferred composition in the differentiation model of Hess and Parmentier (1995). The late stage high-Ti model cumulate of Snyder et al. (1992) used in the Van Orman and Grove (2000) study is the second component. This component is composed of pigeonite, clinopyroxene, ilmenite and a small amount of entrained plagioclase. Its mineralogy is that inferred to precipitate from the lunar magma ocean after ~95% crystallization. The component compositions and bulk hybrid composition are reported in Table 1.

Experimental Procedure

The near liquidus phase relations of the model hybrid source composition were determined in synthesis experiments over the pressure range of 1 to 2 GPa. A synthetic analog of the starting composition (Table 1) was prepared by mixing together high purity reagent grade oxides and Fe^0 sponge (Grove and Bence, 1977). Grinding under ethanol for ~6 hours produced a homogeneous powder. Approximately 500 mg of the powder was pressed into a pellet using Elvanol as a binding agent. The pellet was hung on 0.004" Pt wire in the hotspot of a Deltech DT31VT vertical quenching furnace. It was then conditioned at an oxygen fugacity corresponding to the Fe-FeO buffer at 1000°C for 24 hours using constant mixing proportions of H_2 and CO_2 gases with flow rates of approximately 0.1 mL/s. Oxygen fugacity was monitored using a ZrO_2-CaO electrolyte cell calibrated at the Fe-FeO and Cu-Cu_2O buffers. Temperature was monitored with Pt-$Pt_{90}Rh_{10}$ thermocouples calibrated against the melting points of NaCl, Au and Pd on the IPTS 1968 temperature scale.

After conditioning, 10 mg of the starting powder was packed into a graphite crucible that was placed into an alumina sleeve with powdered graphite packed around the graphite crucible to ensure it remained centered and positioned in the hotspot. These assemblies were then positioned in the hotspot of a graphite heater using MgO spacers. Experiments were performed in a 0.5" piston-cylinder apparatus, similar to the design of Boyd and England (1960), using $BaCO_3$ as the pressure medium. Pressure was calibrated against the transition of anorthite-gehlenite-corundum to Ca-Tschermak's pyroxene as determined by Hays (1965). Temperature was monitored with $W_{97}Re_3$-$W_{75}Re_{25}$ thermocouples with no correction for pressure. The thermal gradient near the hotspot was measured at 20°C/0.1". Sample thickness is <0.05", resulting in a thermal gradient of, <10°C. Runs were pressurized cold to

1.0 GPa and then heated to 865°C at 100°C/min where they were held for 6 min. They were then pumped to the desired run pressure and heated to final run temperature at 50°C/min. To obtain crystal-free glasses, the experiments were quenched by shutting off the power to the furnace and simultaneously dropping the pressure on the experiments to 0.8 GPa.

The experimental charges were mounted in 1" epoxy disks, polished and carbon-coated. Electron microprobe analysis of the charges was performed using the MIT JEOL-JXA 733 superprobes. Crystalline phases were analyzed at an accelerating voltage of 15kV, beam current of 10nA, and a beam diameter of ~2 microns. Quench crystal free glasses in the experimental charges were analyzed with a beam diameter of 10 microns. Frequently, quench free areas could not be located (Figure 1). In those cases, the entire quenched melt area was analyzed using a 20 micron beam in a grid pattern and the composition of the melt phase was obtained by averaging these analyses. Typically 15 or more analyses were necessary to obtain a reliable estimate. This method was shown to provide a reasonable approximation of the glass composition by Parman and Grove (2003) who compared analyses of glassy regions to quench mineral regions in hydrous melting experiments.

The CITZAF correction package of Armstrong (1995), using the atomic number correction from Duncumb and Reed, the absorption corrections with Heinrich's tabulation of mass-absorption coefficients, and the fluorescence corrections from Reed was used to reduce the data and obtain quantitative analyses. A materials balance calculation was used to estimate phase proportions and to assess whether Fe had been lost from the experimental charge. The results are reported in Table 2 as the R^2, the sum of squared residuals, and as phase proportions.

Experimental Results

The experimental data set is shown graphically in Figure 2. Fourteen experiments span a temperature range of 1300 to 1600°C and pressures of 1.0 to 2.0 GPa. At 1.0 GPa, olivine is the first liquidus phase to appear at 1550°C. Orthopyroxene joins the assembly ~100°C later. Olivine and orthopyroxene co-crystallize on the liquidus at 1580°C and 1.5 GPa. These two phases are also present with liquid at 1550°C. The next experiment at ~1450°C, is below the solidus and contains clinopyroxene and ilmenite in addition to olivine and orthopyroxene. Two experiments at 1.7 GPa, 1550 and 1530°C are co-saturated with olivine, orthopyroxene and liquid. At 2.0 GPa, orthopyroxene is the sole liquidus phase at 1580°C but is joined quickly by olivine ~30°C later.

Liquid bulk compositions are plotted in the olivine-clinopyroxene-quartz ternary in Figure 3. The liquid from the 1450°C, 1.0 GPa experiment is closest to clinopyroxene saturation. All the liquids array themselves along the olivine-orthopyroxene reaction boundary. In general, high temperature experiments plot closer to the olivine-quartz join while higher pressures move the liquids towards the olivine-clinopyroxene join.

The TiO_2 and CaO contents of the experimental liquids are plotted against each other in Figure 4. The bulk MOCH composition plots at low CaO and TiO_2 (4.8 and 4.2 wt% respectively) well to the left of the high-Ti lunar glass trend. The TiO_2 contents of the experimental liquids range from 4.2 wt% in experiments above the liquidus, to as high as 10.6 wt% TiO_2 in the lowest temperature experiment (see Figure 4). CaO in the experimental liquids correlates positively with TiO_2. The liquid trend from the MOCH bulk composition intersects the lunar glass trend between 4 and 8 wt% TiO_2.

Discussion

Melting experiments on the MOCH bulk composition produce liquids that plot in the region of the lunar ultramafic glasses. The highest TiO_2 contents of experimental liquids that match the lunar glasses are ~8 wt% which would equate to the Apollo 17 orange glass. Table 3 lists the major element oxides of that lunar glass and the matching experimental liquid. The experimental liquids contain as much as 10 wt % TiO_2 however, the compositions are too CaO rich and do not plot along the lunar glass trend. The same problem was encountered by Van Orman and Grove (2000) in trying to produce high Ti liquids.

The MOCH bulk composition does not have ilmenite as a liquidus phase. Ilmenite is present as a subsolidus phase of this bulk composition along with clinopyroxene. A characteristic feature of the high Ti glasses is the lack of ilmenite as a liquidus phase. Melting of this hypothesized hybridized lunar mantle source cannot produce the TiO_2 contents observed in the Apollo red and black glasses and only manages to produces liquids that match the lowest TiO_2 content orange glasses. So the question remains – how are the ultramafic glasses with elevated TiO_2 contents generated? Two possibilities present themselves based on the results of this study. Either the bulk composition is wrong or the glasses were not generated by a simple melting process of a hybridized lunar mantle source. Below we explore both possibilities.

The liquid trend generated by the hybridized composition displays a positive correlation of TiO_2 to CaO. The experiments of Van Orman and Grove (2000) also generate liquids that display a positive correlation of TiO_2 to CaO. If simple melting of a source is called upon to generate the high Ti glasses, then the source is required to have elevated TiO_2 and moderate CaO contents as shown in Figure 5. The TiO_2 and CaO contents of the hybridized source

region are controlled primarily by the composition of the ilmenite bearing late stage magma ocean cumulate that is added to the deep cumulate. In order for the bulk composition to plot in the region of interest, the proportion of ilmenite in the late stage cumulate must be increased and the amount of pyroxene decreased. Alternatively, the CaO content of the late stage cumulate could be reduced by replacing augite with pigeonite. This scenario however, implies the lunar chemical evolution model of Snyder *et al* (1992) does not account for the total variation in composition of cumulate residues that are left after differentiation and solidification of the magma ocean. One possibility is that the layering developed during cumulate formation did not preserve modal proportions of the crystallizing phases, as is commonly observed in some parts of terrestrial layered intrusions (e.g. the Middle Banded Zone of the Stillwater layered intrusion, McCallum *et al,* 1980). Melting of modally variable residues could explain the variations in composition observed in the lunar ultramafic glasses. Such a scenario is plausible because the melting temperature of clinopyroxene + ilmenite residues has been shown by Van Orman and Grove (2000) to occur >100°C below the temperature of multiple saturation of the high-Ti lunar ultramafic glasses. The necessary compositional criterion (as noted above) is higher modal ilmenite, an effect that would be expected to lower the melting point of the cumulate.

The second possibility is that simple melting of a hybridized source is not the only process at work. Once the liquid is generated it may interact with other surrounding material before being sampled at the lunar surface as an ultramafic magma. Liquids rich in TiO_2 and FeO, as those generated in the experiments performed in this study are, will be denser than the surrounding mantle and sink where they will encounter hotter temperatures that lead to further melting. The experimental assemblages produced in this study indicate that as

pressure increases, the olivine-orthopyroxene reaction boundary migrates towards more olivine rich compositions. For the descending liquids to remain olivine-orthopyroxene saturated, as previous experimental studies indicate they must, then the liquids must dissolve olivine and precipitate orthopyroxene (see Figure 6). A possible model for generating the high-Ti ultramafic glasses is that the hybridized source regions experienced small degrees of melting and the low-degree melts sink into hotter mantle where they react with hotter cumulates, resulting in further melting and modification.

In order to asses the behavior of a hybridized source region during melting, we have used the experimental results and the available phase equilibrium data on lunar ultramafic magmas and primitive terrestrial magmas to estimate the melting/crystallization behavior of the MOCH bulk composition. It was necessary to perform this petrologic modeling exercise because of our inability to produce low extents of melting in the mafic MOCH composition. Experimental liquids at 1.0 and 2.0 GPa were selected for modeling. The compositional characteristics of the residual liquids in the olivine + orthopyroxene + clinopyroxene ± spinel saturated melts using the technique of Kinzler and Grove (1992). These boundaries at 1.0 and 1.5 GPa are shown in Figure 5. These boundaries were assumed to approximate the point at which clinopyroxene appears as a liquidus phase. Using these projected phase boundaries to predict the appearance of clinopyroxene, the observed proportions of olivine and orthopyroxene from the MOCH experiments at 1.0 and 2.0 GPa were used to calculate a liquid line of descent for the MOCH composition until clinopyroxene appears as a saturating phase. This point was taken to be when the olivine + orthopyroxene curve reached the predicted multiple saturation point (Fig. 5). Liquids were calculated in 2% crystallization intervals and the compositions of olivine and orthopyroxene were calculated to be in

equilibrium with the residual liquid at each step as described in Yang *et al* (1996). When clinopyroxene saturation commences, the phase proportions were calculated using the composition of olivine, orthopyroxene and clinopyroxene from the MOCH experiment, with Mg and Fe properly adjusted for exchange equilibrium and the minor element and Ca contents of the pyroxenes fixed at values of the 1450°C, 1.5 GPa experiment.

In the case of the 1.0 GPa liquid (MOCH 2-19), its composition is very close to the predicted multiple saturation point at 1.0 GPa, so it crystallized olivine + orthopyroxene + clinopyroxene in the model calculation. The crystallization model was carried out until the TiO_2 content of the residual liquid reached 18 wt%. For the 2.0 GPa calculation (MOCH 2-5), the liquid continues to precipitate olivine + orthopyroxene until clinopyroxene saturation is reached, where crystallization continues at the reaction boundary until a TiO_2 content of 18 wt% is obtained. These crystallization models may be thought of as the reverse of partial melting models for the MOCH source material. The CaO vs TiO_2 variation of these liquids is plotted in Figure 7. The important result of these models is that melting with clinopyroxene present follows a trend that parallels that of the high-Ti lunar ultramafic glasses. The modeled trend for 1.0 GPa lies at higher CaO contents. The trend of partial melting for the 2.0 GPa data passes through the CaO vs. TiO_2 trend at the upper end of the glass trend. Note that neither of the modeled high TiO_2 partial melt compositions are a match for the high Ti ultramafic glasses. The abundances of SiO_2, CaO, TiO_2 and Al_2O_3 are within the range of values spanned by the high-Ti glasses (see Table 4). The value of TiO_2 at which ilmenite saturation occurs has not been measured directly. Wagner and Grove (1997) found ilmenite saturation along with olivine and orthopyroxene at >18 wt% TiO_2 in their experiments on the Apollo 14 black glass composition. Longhi (1996) also determined the

TiO_2 content of ilmenite saturation for model hybrid mare source compositions at 2.5 and 3 GPa. He found ilmenite saturation between ~20 and 22 wt% TiO_2. Thus a melt containing 18 wt% TiO_2 can be thought of as a melt from a MOCH source region in which ilmenite has been exhausted.

These model results can be used to frame a dynamic model for the origin of the high-Ti glasses in the context of the hypothesis of Elkins-Tanton *et al* (2002) who suggest that high-Ti melts sink into the lunar interior and interacts with underlying magma ocean cumulates. If a hybridized magma ocean cumulate were to undergo low extents of melting, the melt would percolate to greater depths, where it would encounter high temperature cumulates with which it would react, melt further and change composition by dissolving magnesian silicate cumulates (Figure 6) and diluting its major element composition. Thus a high-Ti, low-degree partial melt, such as the 1.0 GPa model example, could dilute its CaO and TiO_2, bringing it down to the ultramafic glass array and increase its MgO content as it equilibrates with deeper, Mg-rich cumulates. Such a melt might continue to sink to deeper levels until it reaches a stage of neutral, then finally positive buoyancy. This might be the maximum depth of origin of the magma which is not controlled by an in-situ melting event but a multi-stage dissolution process that ends when high-Ti melts become eruptable.

Conclusions

The hypothetical hybridized lunar mantle source composition for the high-Ti ultramafic glasses used in this study cannot give rise to the glasses with >10wt% TiO_2. Although experimental liquids with 10 wt% TiO_2 were generated by melting of this composition, the CaO contents were too high and plot off of the lunar glass trend shown in Figure 4. Melting

of this MOCH source can generate glasses with moderate TiO_2 contents such as the Apollo 17 orange compositions.

If simple melting of a hybridized source is called upon for generation of the high-TiO_2 glasses, then the source must have elevated TiO_2 and low CaO contents. Alternatively, melts of a modally variable high-Ti residues or small degree clinopyroxene-saturated melts of the MOCH hybridized source could undergo processing after their generation. In the previous models of high-Ti melting, the multiple saturation points of the glass composition are taken to indicate the depth of origin. This has raised the problem of how such negatively buoyant melts can be erupted (Agee and Cicerone, 1995). It is also possible that the multiple saturation points are not the key to the origin of the high-Ti ultramafic magmas. When the melts are denser then the surrounding mantle, they sink and melting/reaction with hotter underlying mantle occurs. When they experience sufficient reaction to change from negative to positively buoyant then they can erupt. In this case, the experimentally determined multiple saturation points do not represent the depths of origin and the high-Ti Apollo 14 black, Apollo 15 red and Apollo 17 orange come from shallower depths – between 200 and 275 km (Elkins-Tanton *et al*, 2002) where they are positively buoyant. What then is the significance of the multiple saturation points of these melts? The implication is that the liquids are saturated with only olivine in the source when they are erupted and the temperature of the underlying mantle and high-Ti partial melt that sinks into it drives the melting reaction to the point that all but olivine is exhausted from the residue.

References

Agee C.B. and Cicerone S.B. (1995) Crytal-liquid inversions in high-TiO2 basalt. *Lunar Planet. Sci.* **XXVI**, 5-6.

Anderson A.T. (1971) Exotic armalcolite and the origin of Apollo 11 ilmenite basalts. *Geochim. Cosmochim. Acta* **35**, 969-973.

Armstrong J.T. (1995) Citzaf - a package of correction programs for the quantitative electron microbeam x-ray-analysis of thick polished materials, thin-films, and particles. *Microbeam Analysis* **4**, 177-200.

Boyd F.R. and England J.L. (1960) Apparatus for phase equilibrium studies at pressures up to 50 kbars and temperatures up to 1750°C. *J. Geophys. Res.* **65**, 741-748.

Delano J.W. (1980) Chemistry and liquidus relations of Apollo 15 red glass: Implications for the deep lunar interior. *Proc. Lunar Sci. Conf.* **11th**, 251-288.

Delano J.W. (1986) Pristine lunar glasses: Criteria, data, and implications. *J. Geophys. Res.* **91**, D201-D213.

Elkins-Tanton L.T., Van Orman J.A., Hager B.H. and Grove T.L. (2002) Re-examination of the lunar magma ocean cumulate overturn hypothesis: Melting or mixing is required. *Earth Planet. Sci. Lett.* **196**, 239-249.

Green D.H., Ringwood A.E., Hibberson W.O. and Ware N.G. (1975) Experimental petrology of the Apollo 17 mare basalts. *Proc. Lunar Sci. Conf.* **11th**, 871-893.

Grove T.L. and Bence A.E. (1977) Experimental study of pyroxene-liquid interaction in quartz-normative basalt 15597. *Proc Lunar Sci. Conf.* **8th**, 1549-1579.

Hays J.F. (1965) Lime-alumina-silica. *Carnegie Inst. Wash. Yearbk.* **65**, 234-236.

Hess P.C. (1991) Diapirism and the origin of high TiO_2 glasses. *Geophys. Res. Lett.* **18**, 2069-2072.

Hess P.C. and Parmentier E.M. (1995) A model for the thermal and chemical evolution of the Moon's interior: Implications for the onset of mare volcanism. *Earth Planet. Sci. Lett.* **134**, 501-514.

Hubbard N.J. and Minear J.W. (1975) A physical and chemical model of early lunar history. *Proc. Lunar Sci. Conf.* **6th**, 1057-1085.

Kinzler R.J. and Grove T.L. (1992) Primary magmas of mid-ocean ridge basalts 1. Experiments and methods. *J. Geophys. Res.* **97**, 6885-6906.

Longhi J. (1996) Investigation of the origin of hi-Ti basalts by polybaric fractional fusion. *Lunar Planet. Sci. Conf.* **27th**, 767-768.

McCallum I.S.E., Raedke L.D. and Mathez E.A. (1980) Investigations of the Stillwater Complex: Part I. Stratigraphy and structure of the Banded Zone. *Amer. J. Sci.* **280-A**, 59-87.

Parman S.W. and Grove T.L. (2003) Harzburgite melting with and without H2O: Experimental data and predictive modeling. *J. Geophys. Res.* (in press).

Ringwood A.E. and Kesson S.E. (1976) A dynamic model for mare basalt petrogenesis. *Proc. Lunar Sci. Conf.* **7th**, 1697-1722.

Shearer C.K. and Papike J.J. (1993) Basaltic magmatism on the Moon: A perspective from volcanic picritic glass beads. *Geochim. Cosmochim. Acta* **57**, 4785-4812.

Shearer C.K. and Papike J.J. (1999) Magmatic evolution of the Moon. *Am. Mineral.* **84**, 1469-1494.

Shearer C.K., Papike J.J., Simon S.B., Galbreath K.C., Shimizu N., Yurimoto Y. and Sueno S. (1990) Ion microprobe studies of REE and other trace elements in Apollo 14 'volcanic' glass beads and comparison to Apollo 14 mare basalts. *Geochim. Cosmochim. Acta* **54**, 851-867.

Snyder G.A., Taylor, L.A. and Neal C.R. (1992) A chemical model for generating the sources of mare basalts: Combined equilibrium and fractional crystallization of the lunar magmasphere. *Geochim. Cosmochim. Acta* **56**, 3809-3823.

Taylor S.R. and Jakes P. (1974) The geochemical evolution of the Moon. *Proc. Lunar Sci. Conf.* **5th**, 1287-1305.

Van Orman J.A. and Grove T.L. (2000) Origin of lunar high-titanium ultramafic glasses: Constraints from phase relations and dissolution kinetics of clinopyroxene-ilmenite cumulates. *Met. & Planet. Sci.* **35**, 783-794.

Wagner T.P. and Grove T.L. (1997) Experimental constraints on the origin of lunar high-Ti ultramafic glasses. *Geochim. Cosmochim. Acta* **61**, 1315-1327.

Warren P.H. and Wasson J.T. (1979) The origin of KREEP. *Rev. Geophys. Space Phy.* **17**, 73-88.

Yang H.J., Kinzler R.J. and Grove T.L. (1996) Experiments and models of anhydrous, basaltic olivine-plagioclase-augite saturated melts from 0.001 to 10 kbar. *Contrib. Mineral. Petrol.* **124**, 1-18.

Figure Captions

Figure 1. Back scattered electron image of experiment MOCH 2-27. No quench crystal free glass was present in this experiment. The entire quenched area was analyzed in a grid patter with a 20 μm beam and the results averaged to obtain a valid glass composition.

Figure 2. Pressure-Temperature grid of experiments performed during this study. Symbols indicate phases produced. Solid fill denotes crystalline phases.

Figure 3. Olivine-Quartz-Clinopyroxene pseudoternary diagram. Compositions of experimentally produced liquids are plotted as circles. Yellow symbols are liquids from experiments with high sum of squared residuals (see Table 2 and text). The 1.5 and 1.0 GPa olivine-orthopyroxene-clinopyroxene saturated melt compositions from Kinzler and Grove (1992) are also plotted. Main diagram is a subset as indicated by the inset.

Figure 4. CaO vs TiO_2. Experimentally produced liquids are plotted along with the ultramafic lunar glass data of Delano (1986).

Figure 5. CaO vs TiO_2 diagram displaying possible source compositions needed to generate the very high-Ti bearing glasses. Crystallization trends from this study and the Van Orman and Grove (2000) study are translated to intersect at the highest Ti bearing glass (Apollo 12 red) and bracket a region of possible compositions for that glass source.

Figure 6. Ol-Cpx-Qtz ternary diagram showing the migration of the phase boundaries with increasing pressure. The effect of pressure is to decrease the olivine primary phase volume. If a liquid generated at 1.0 GPa (represented by the yellow dot) is

denser than the surrounding mantle it will sink. In order to maintain saturation with olivine and orthopyroxene, the liquid composition must change through assimilation of olivine and precipitation of orthopyroxene.

Figure 7. Model liquid trends. Liquid compositions from two model runs, at 1.0 and 2.0 GPa are plotted in CaO vs TiO_2 space. The liquids are modeled as crystallizing olivine and pyroxene until the liquid composition reaches 18 wt% TiO2(see text). The 2.0 GPa liquid closely follows the lunar glass trend. Arrows at the ends of the crystallization trends indicate the direction the liquid composition would take once ilmenite crystallization begins.

Figure 1.

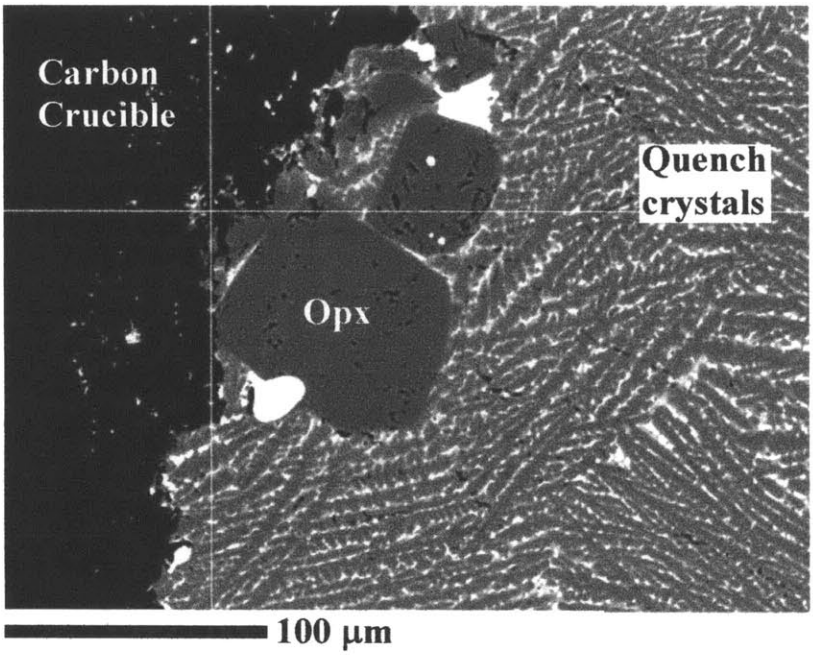

Figure 2.

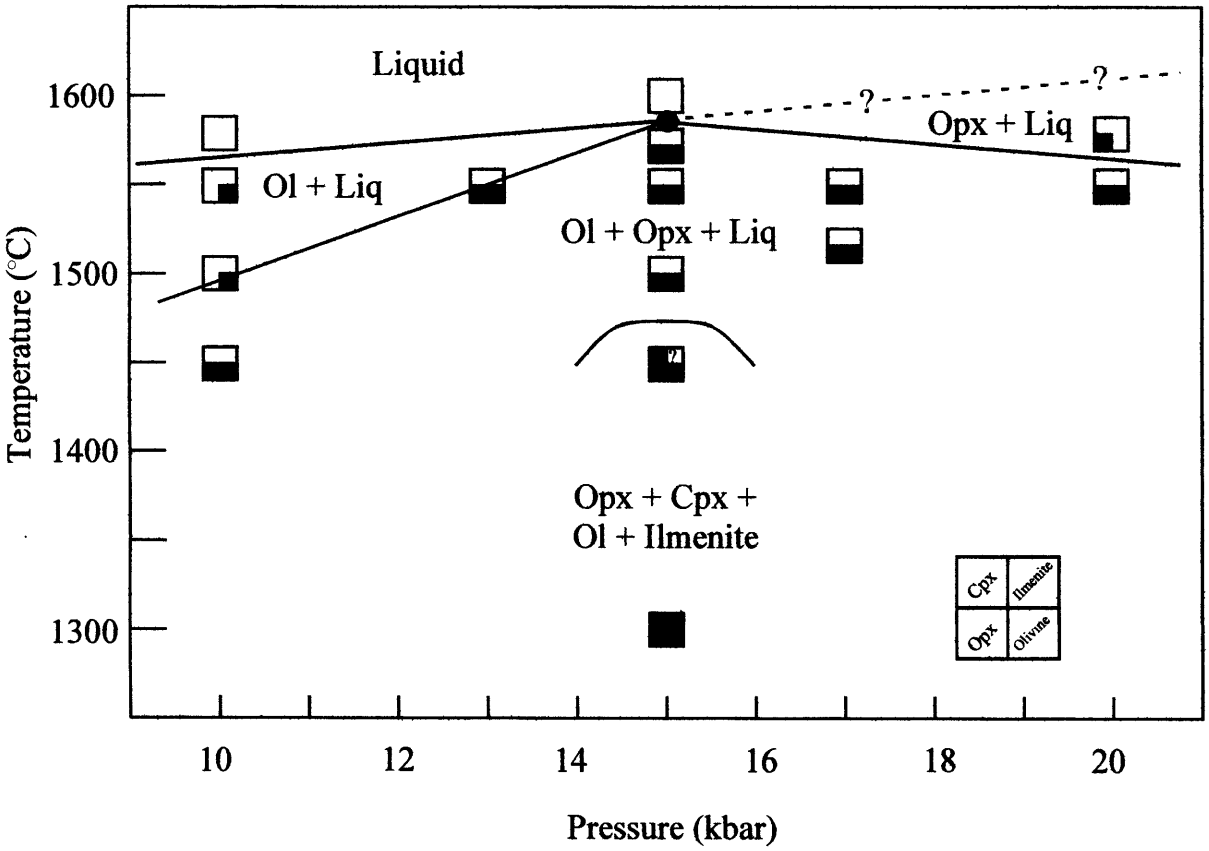
Liquid
Ol + Liq
Ol + Opx + Liq
Opx + Liq
Opx + Cpx +
Ol + Ilmenite
Cpx
Ilmenite
Opx
Olivine
1600
1500
1400
1300
Temperature (°C)
10
12
14
16
18
20
Pressure (kbar)

Figure 3.

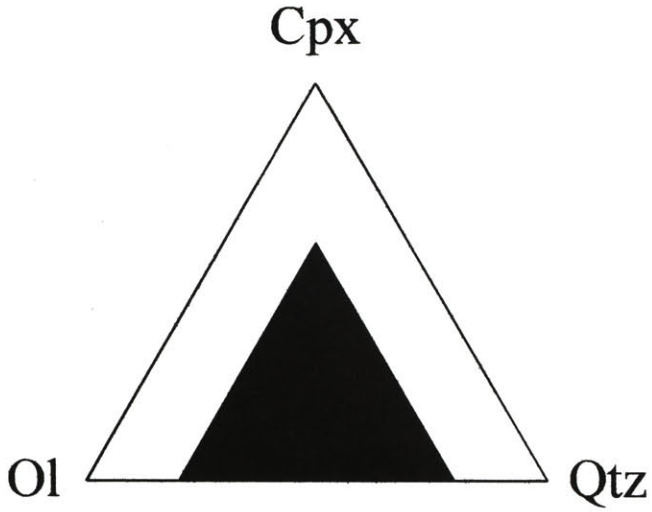
Cpx
Ol
Qtz

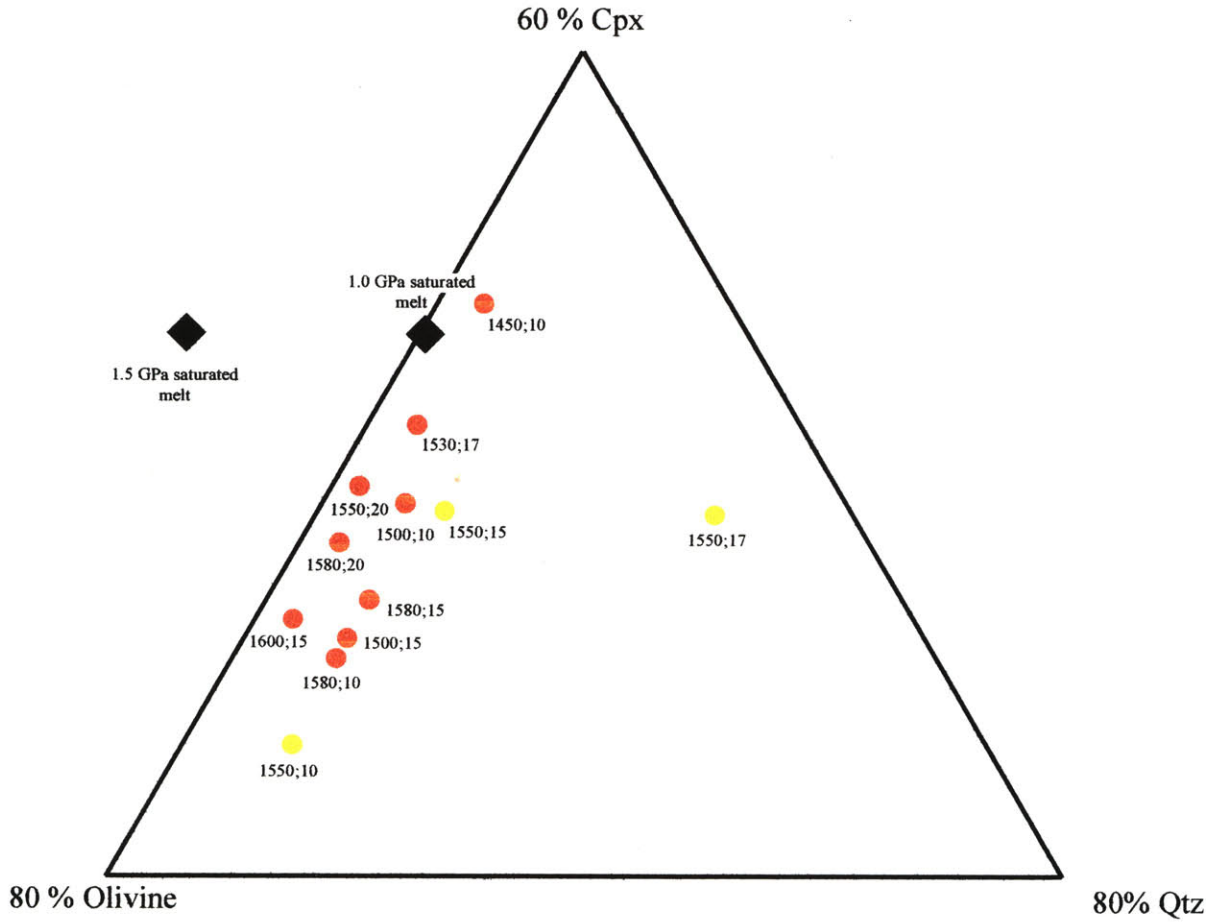
60 % Cpx
1.0 GPa saturated melt
1450;10
1.5 GPa saturated melt
1530;17
1550;20
1500;10
1550;15
1550;17
1580;20
1580;15
1600;15
1500;15
1580;10
1550;10
80 % Olivine
80% Qtz

Figure 4.

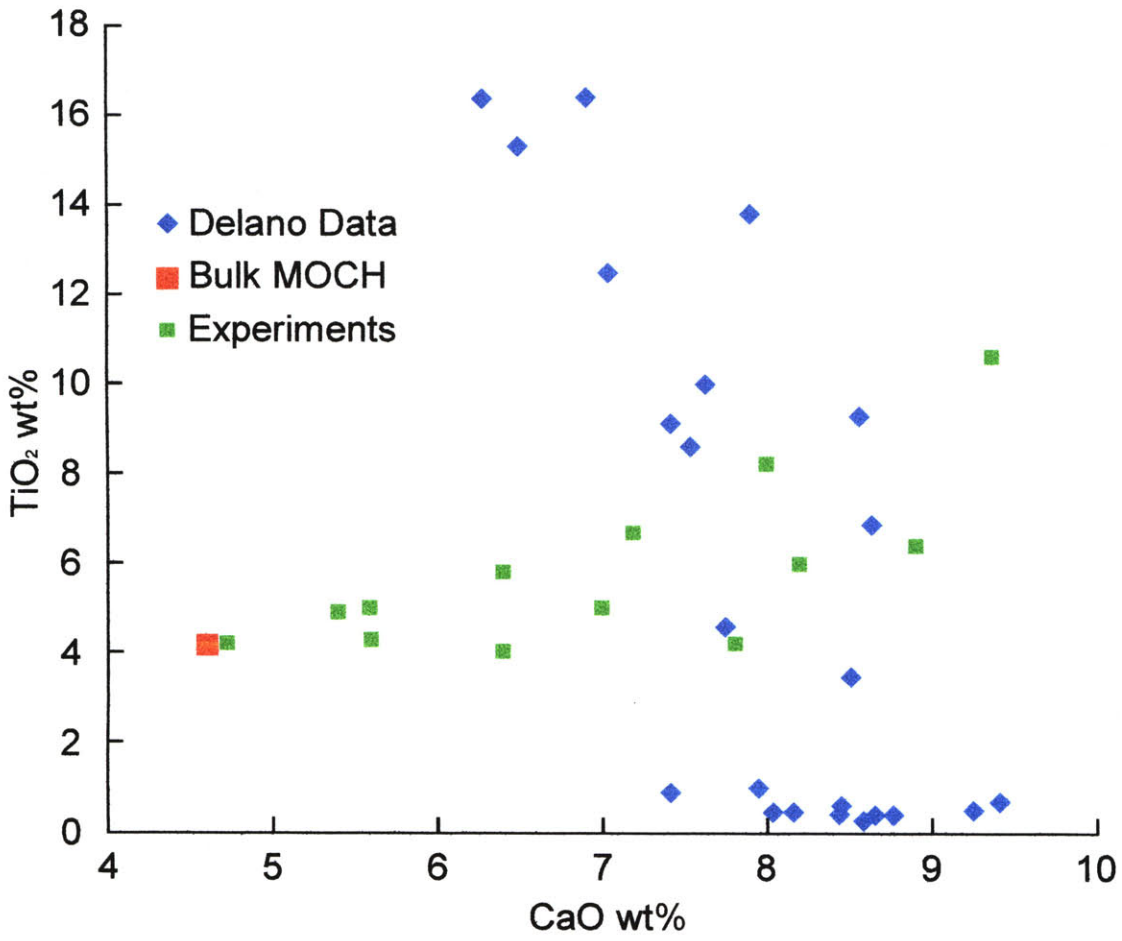
Delano Data
Bulk MOCH
Experiments
TiO₂ wt%
CaO wt%
0
2
4
6
8
10
12
14
16
18
4
5
6
7
8
9
10

Figure 5.

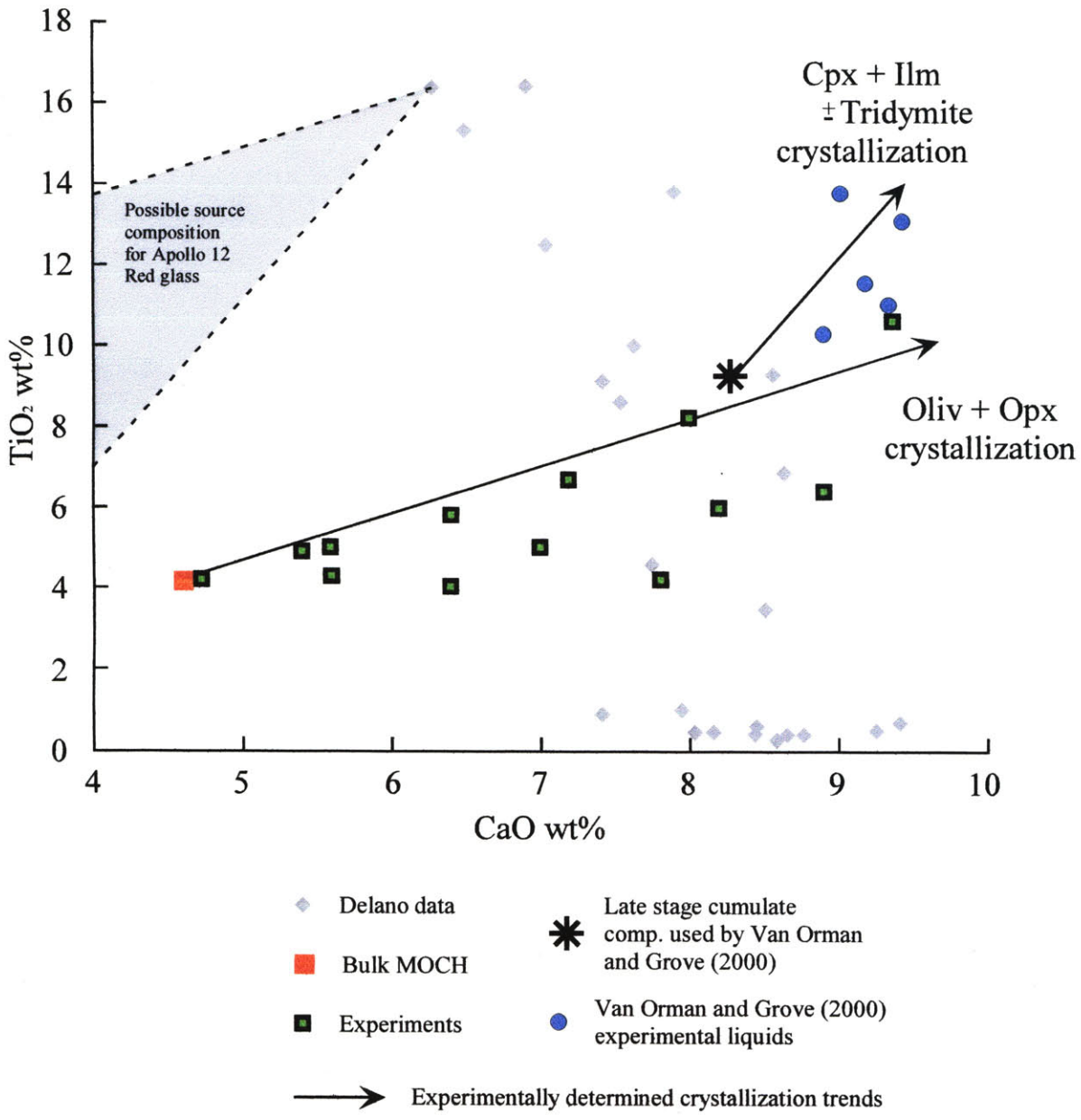
18
16
14
12
10
8
6
4
2
0
TiO2 wt%
4
5
6
7
8
9
10
CaO wt%
Possible source composition for Apollo 12 Red glass
Cpx + Ilm ± Tridymite crystallization
Oliv + Opx crystallization
Delano data
Bulk MOCH
Experiments
Late stage cumulate comp. used by Van Orman and Grove (2000)
Van Orman and Grove (2000) experimental liquids
Experimentally determined crystallization trends

Figure 6.

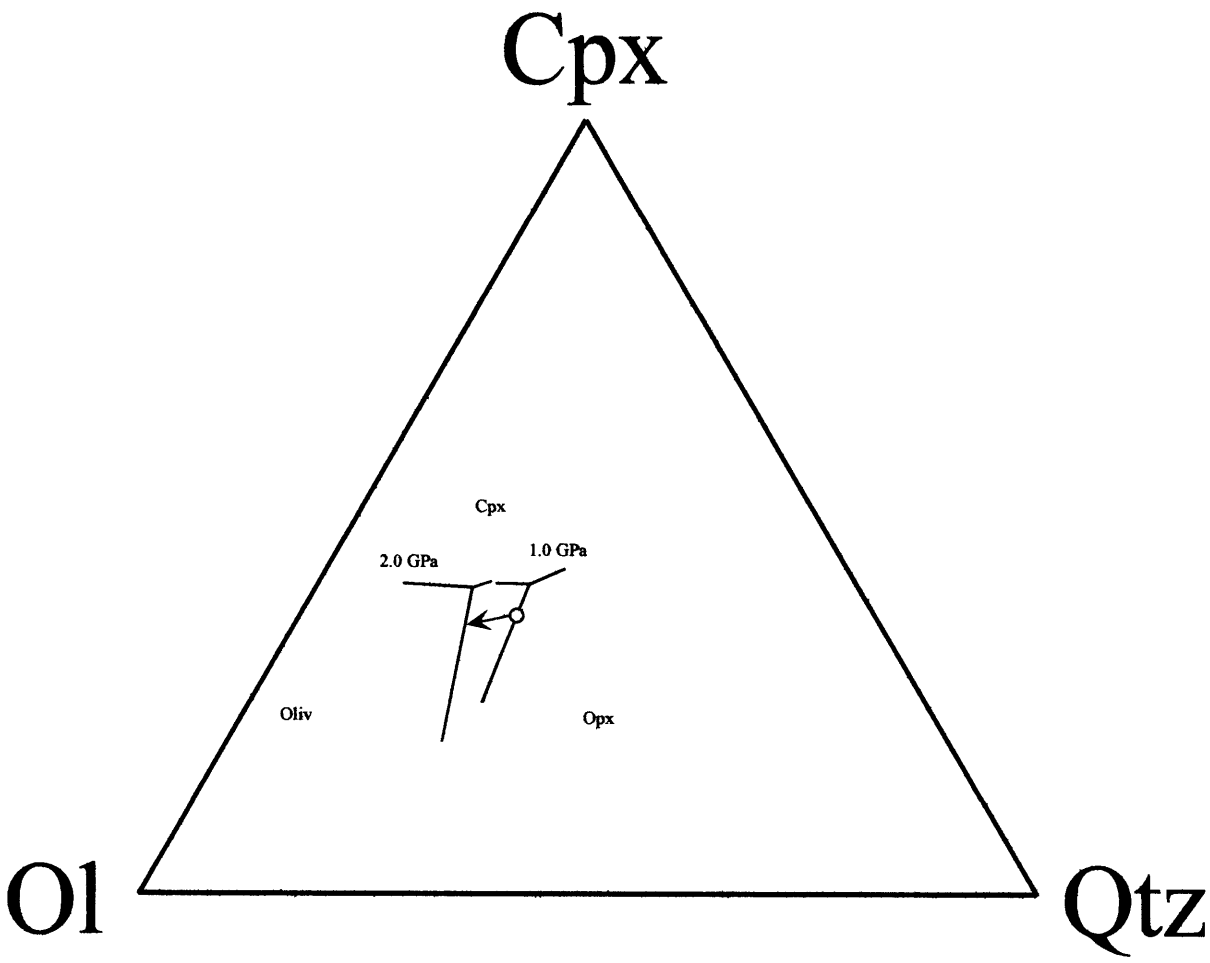

Figure 7.

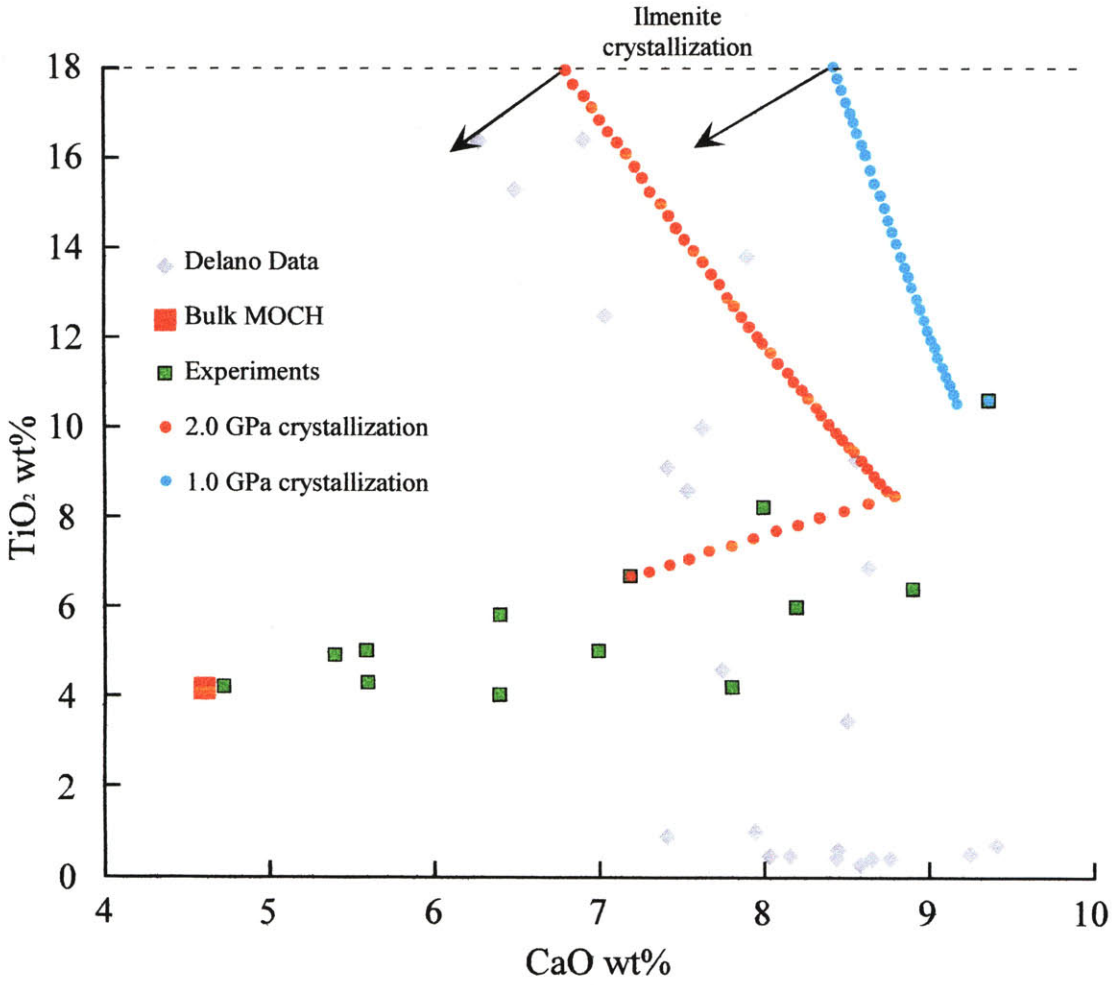
Ilmenite
crystallization
Delano Data
Bulk MOCH
Experiments
2.0 GPa crystallization
1.0 GPa crystallization
TiO₂ wt%
CaO wt%
0
2
4
6
8
10
12
14
16
18
4
5
6
7
8
9
10

Table 1. Magma Ocean Cumulate Hybrid component compositions

	Deep cumulate	Late Stage cumulate	MOCH
SiO2	40.35	41.61	45.44
TiO2	0	9.1	4.22
Al2O3	0	2.8	2.64
Cr2O3	0	0	0.19
FeO	12.54	29.6	18.97
MgO	47.11	7.5	23.84
CaO	0	8.2	4.6
Total	100	98.81	99.9
mg#	87	31	69

Exp #	duration (hours)	P (GPa)	T (C)	Phases (# analysis)	F	SiO_2	TiO_2	Al_2O_3	Cr_2O_3	FeO	MgO	CaO	Total	mg#	$K_d^{phase/liq}$	SSR
MOCH2-1	6.5	1.5	1300	Opx(30)[a]	0.27	53.0(5)[b]	1.3(2)	2.4(4)	0.21(4)	15.6(4)	25.6(4)	2.7(2)	100.81	74.6		0.860
				Cpx(5)	0.46	52.2(1)	1.41(7)	2.4(2)	0.19(1)	14.5(2)	21.5(5)	8.3(2)	100.50	72.5		
				Olivine(8)	0.19	37.4(2)	0.18(2)	0.07(2)	0.04(1)	25.3(4)	36.8(2)	0.36(1)	100.15	72.2		
				Ilmenite*	0.06	-[c]	-	-	-	-	-	-				
MOCH2-2	2.75	1.5	1450	Opx (18)	0.79	55.9(5)	0.52(8)	0.6(1)	0.16(2)	12.0(2)	30.3(4)	1.3(2)	100.78	81.8		35.850
				Olivine(16)	0.03	38.6(2)	0.15(3)	0.04(1)	0.11(1)	19.2(6)	42.3(7)	0.26(2)	100.66	79.7		
				Ilmenite*	0.12	-	-	-	-	-	-	-				
MOCH2-5	3	2.0	1550	Opx(12)	0.24	56.4(2)	0.36(5)	0.49(6)	0.15(2)	10.5(2)	31.0(1)	1.08(5)	99.98	84.0	0.26	0.105
				Ol(11)	0.13	39.1(2)	0.07(1)	0.03(1)	0.05(1)	17.3(5)	43.4(2)	0.20(2)	100.15	81.7	0.31	
				Liquid(2)	0.63	43.1(1)	6.7(2)	3.7(2)	0.17(6)	23(1)	18(1)	7.2(5)	101.87	58.1		
MOCH2-7	1.5	1.5	1580	Ol(10)	0.01	40.2(3)	0.07(2)	-	0.08(2)	12.2(2)	48.1(3)	0.15(2)	100.80	87.5	0.46	0.065
				Opx(3)	0.09	57.5(5)	0.4(2)	0.33(8)	0.15(3)	8(1)	33.6(7)	0.8(2)	100.78	87.8	0.44	
				Liquid(4)	0.84	47.8(2)	5.0(3)	2.73(6)	0.14(5)	13.6(5)	24.5(2)	5.6(3)	99.37	76.2		
				Metal	0.06	-	-	-	-	-	-	-				
MOCH2-8	1.75	2.0	1580	Opx(8)	0.21	57.0(6)	0.3(1)	0.4(1)	0.13(3)	8.6(6)	33.2(5)	0.8(1)	100.43	87.3	0.38	0.120
				Liquid(5)	0.73	45.2(4)	5.8(3)	3.2(2)	0.06(2)	16.5(7)	22.8(7)	6.4(5)	99.96	72.4		
				Metal	0.06	-	-	-	-	-	-	-				
MOCH2-9	2	1.0	1580	Liquid(20)	0.91	49.5(5)	4.2(1)	2.45(4)	0.05(4)	12.4(5)	27.0(2)	4.72(5)	100.32	68.5		1.114
				Metal	0.08	-	-	-	-	-	-	-				
MOCH2-14	2.8	1.0	1550	Ol (19)	0.17	40.0(3)	0.08(3)	-	0.11(2)	11.7(4)	48.1(3)	0.16(2)	100.15	88.2	0.38	59.242
				Liquid (12)	0.80	46.3(5)	4.0(2)	9(1)	0.13(5)	13.7(2)	21.1(6)	6.4(1)	100.63	73.3		
MOCH2-17	2	1.0	1500	Ol (4)	0.15	39.7(2)	0.08(2)	0.02(1)	0.09(1)	12.8(1)	46.7(1)	0.18(1)	99.57	86.7	0.34	1.539
				Liquid (11)	0.82	48.1(5)	5.0(4)	2.8(1)	0.25(5)	17.1(9)	20.9(9)	7.0(6)	101.15	68.6		
				Metal	0.03	-	-	-	-	-	-	-				
MOCH2-18	2.5	1.5	1600	Liquid (30)		47.4(3)	4.3(2)	3.3(1)	0.12(5)	13.3(3)	25.8(3)	5.6(1)	99.82	77.5		
MOCH2-19	2.5	1.0	1450	Opx (11)	0.49	57.0(4)	0.54(8)	0.30(5)	0.13(2)	10.1(3)	32.3(2)	1.12(8)	101.49	85.1	0.22	0.243
				Ol (8)	0.12	39.5(2)	0.11(2)	0.03(1)	0.10(2)	15.1(3)	45.0(3)	0.21(2)	100.05	84.2	0.24	
				Liquid (2)	0.33	40.0(8)	10.6(1)	5.77(6)	0.10(5)	21(2)	15(1)	9.37(7)	101.84	55.9		
				Metal	0.05	-	-	-	-	-	-	-				

[a] Number in parenthesis indicates the number of analyses used for average

[b] Number in parenthesis is one sigma standard deviation in terms of least units cited. Therefore, 38.7(3) should be read as 38.7 ± 0.3wt%

[c] Indicates element not analyzed of below detectability limit

Exp #	duration (hours)	P (GPa)	T (C)	Phases (# analysis)	F	SiO_2	TiO_2	Al_2O_3	Cr_2O_3	FeO	MgO	CaO	Total	mg#	$K_d^{phase/liq}$	SSR
MOCH2-21	2.5	1.7	1550	Liquid (7)	0.45	49.7(6)	6.4(5)	8.5(3)	0.21(5)	15.3(4)	10.8(7)	8.9(3)	99.81	55.6		3.224
				Olivine (5)	0.23	40.4(2)	0.09(0)	0.04(1)	0.10(2)	12.8(2)	47.6(5)	0.17(2)	101.20	86.9	0.19	
				Opx (7)	0.24	57.9(2)	0.48(5)	0.38(4)	0.10(3)	8.4(2)	33.9(2)	0.87(2)	102.03	87.8	0.18	
				Metal	0.07	-	-	-	-	-	-	-				
MOCH2-22	3	1.5	1550	Liquid (24)	0.65	50.0(6)	4.2(6)	4.4(6)	0.19(6)	10.5(7)	22(2)	7.8(8)	99.09	79.0		2.419
				Olivine (4)	0.06	41.0(2)	0.13(2)	-	0.10(1)	8.4(2)	51.6(3)	0.18(2)	101.41	91.7	0.36	
				Opx (5)	0.18	58.6(1)	0.46(5)	0.31(5)	0.13(1)	6.0(2)	36.3(7)	0.77(7)	102.57	91.5	0.35	
				Metal	0.11	-	-	-	-	-	-	-				
MOCH2-25	3	1.7	1530	Liquid (2)	0.51	41.6(5)	8.2(1)	4.5(1)	0.19(2)	20.0(4)	16.7(1)	8.0(2)	99.19	59.8		0.087
				Opx (20)	0.37	56.9(4)	0.58(8)	0.5(1)	0.13(2)	9.1(6)	32.3(7)	0.9(2)	100.41	86.3	0.24	
				Olivine (7)	0.07	40.0(3)	0.15(3)	0.05(1)	0.13(1)	15.0(2)	45.4(3)	0.23(1)	100.96	84.3	0.28	
				Metal	0.04	-	-	-	-	-	-	-				
MOCH2-27	3	1.5	1500	Liquid (183)	0.85	49(1)	4.9(9)	3.1(3)	0.14(6)	16(1)	24(1)	5.4(5)	102.54	73.4		0.005
				Opx (6)	0.03	57.8(4)	0.4(1)	0.25(7)	0.09(2)	7.2(4)	34.6(5)	0.6(2)	100.94	89.6	0.32	
				Olivine (11)	0.05	40.3(4)	0.11(2)	-	0.11(1)	10.8(2)	48.9(4)	0.12(1)	100.34	89.0	0.34	
				Metal	0.05	-	-	-	-	-	-	-				

Table 3. Apollo 17 Orange comparison

	Apollo 17 Orange glass	MOCH2-25 1.7 GPa; 1530C	% Diff
SiO_2	39.4	41.6	5.3%
TiO_2	8.63	8.2	5.2%
Al_2O_3	6.21	4.5	38.0%
Cr_2O_3	0.67	0.2	252.6%
FeO	22.2	20.0	11.0%
MgO	14.7	16.7	12.0%
CaO	7.53	8.0	5.9%

Table 4. Apollo high-Ti ultramafic glass and model liquid compositions

	Apollo 12 red	Apollo 14 black	1.0 GPa model	2.0 GPa model
SiO_2	33.4	34.0	32.1	31.8
TiO_2	16.4	16.4	16.1	15.9
Al_2O_3	4.6	4.6	7.2	5.9
Cr_2O_3	0.84	0.92	0.27	0.44
FeO	23.9	24.5	26.9	34.3
MgO	13.0	13.3	8.8	4.4
CaO	6.27	6.9	8.6	7.2

Crystallization/partial melting model for 1.0 GPa used MOCH 2-19 liquid as a starting liquid and crystallized olivine, orthopyroxene and clinopyroxene at the reaction point with the following coefficents: 0.4 Opx + 1 Liq = 0.1 Oliv + 1.3 Cpx. 2.0 Gpa model used MOCH 2-5 liquid as a starting liquid and coefficients of: 1 Liq = 0.33 Oliv + 0.67 Opx.